University of Modena and Reggio Emilia
Department of Engineering "Enzo Ferrari"

PhD "Enzo Ferrari" in Industrial and Environmental Engineering

XXXV Cycle

Multi-temporal SAR interferometry for ground deformation and structural investigations

Doctoral Dissertation

Supervisor
Prof. Francesco Mancini

Co-Supervisor
Prof. Alessandro Capra

Coordinator of the PhD Program
Prof. Alberto Muscio

Candidate
Francesca Grassi

Modena, May 2023

Abstract

Satellite radar interferometry is an effective technique in different applications focused on Earth surface deformation phenomena mainly for its ability to depict the displacement of ground targets at a very high accuracy level (1–2 mm/yr). Since the 1990s, several synthetic aperture radar missions with various frequency, spatial and temporal resolution have been launched enabling the investigation of different phenomena occurring at different spatial and temporal scale: from the first low resolution and the new generation of medium resolution satellite radar missions (e.g. ERS, Envisat and Sentinel-1) for large scale phenomena investigations (such as natural hazard assessment, ground deformation phenomena and polar cap dynamics investigations, slope failures, and instability processes) to the more recent high-resolution systems (e.g. COSMO-SkyMed and TerraSAR-X) that opened new perspectives in the infrastructures and structures monitoring field.
This dissertation focuses on the ability and potentiality of satellite radar data to generate valuable information for the interpretation of phenomena occurring on the Earth surface. To this aim, the multi-temporal interferometric processing of dual-orbit set of synthetic aperture radar data was complemented by the accuracies assessment by uncertainty analysis.
Given the availability of both medium and high resolution data, this thesis deals with topics from ground deformation phenomena up to structural investigations. The first objective is the development, testing and validation of an open-source processing workflow of synthetic aperture radar data including a calibration and decomposition procedure and complemented by the accuracy assessment of the results with error propagation analysis. Then, ground deformation phenomena, and, in particular, ground subsidence, are characterized in relation to their different contributions exploiting an approach based on a spatial analysis of the processed interferometric products performed in a geographic information system environment. Finally, the potentialities of interferometric satellite techniques for structural applications have been assessed presenting a procedure for the reconstruction of structural motion of single buildings from dual-orbit interferometric products complemented by the estimation of the motion parameters uncertainties.

Acknowledgements

First and foremost, I would like to express my gratitude to my supervisor, Prof. Francesco Mancini, for granting me the opportunity to pursue my PhD and for his continuous support and kind patience during these years. I would like to extend my thanks to my co-supervisor, Prof. Alessandro Capra, who constantly supported me during this PhD journey with valuable advices and his kindness.
A special thanks to the other members of the Geomatics Laboratory, Cristina Castagnetti, Paolo Rossi and Benedetta Brunelli for being supportive at every stage of my PhD and the enjoyable time spent together.
My gratitude also goes to the board of the PhD in Industrial and Environmental Engineering and, in particular, to the Coordinator Prof. Alberto Muscio, for providing me with the opportunity to participate in this PhD program.

I am also grateful to Eng. Angelo Galeandro and Dr. Nicola Cenni for their key contributions to the development of the first version of the decomposition algorithm and the processing and analysis of the GNSS observations, respectively.
I extend my gratitude to Prof. Loris Vincenzi and Eng. Elisa Bassoli for the collaboration on structural investigations topics, looking forward to continue our work together in the future.

Special thanks to the reviewers of my PhD thesis for their willingness and their valuable suggestions and comments.
I would like to acknowledge the Geomatics Research Unit of the Centre Tecnològic de Telecomunicacions de Catalunya and, in particular Dr. Michele Crosetto, for kindly hosting me during my abroad research period and for his valuable suggestions.

Finally, I would like to express my heartfelt thanks to my parents for their unwavering trust and support throughout all these years and to my sister Giulia for always being there for me with love and care.
Lastly, my deepest gratitude goes to my Pasquale for his endless and loving patience and for his steadfast belief in my abilities.

Contents

List of Figures

List of Tables

List of Acronyms

CGNSS	Continuous GNSS
CSG	COSMO-SkyMed Second Generation
CSK	COSMO-SkyMed
DEM	Digital Elevation Model
DInSAR	Differential InSAR
EO	Earth Observation
ESA	European Space Agency
ETRF	European Terrestrial Reference Frame
GACOS	Generic Atmospheric Correction Online Service
GIS	Geographic Information System
GNSS	Global Navigation Satellite System
InSAR	Interferometric SAR
IW	Interferometric Wide
LOS	Line Of Sight
PS	Persistent Scatterer
PSI	PS Interferometry
S1	Sentinel-1
SAR	Synthetic Aperture Radar
SBAS	Small Baseline Subset
SLC	Single Look Complex
SNAP	Sentinel Application Platform
SNAPHU	Statistical Cost Network Flow Algorithm for Phase Unwrapping
SRTM	Shuttle Radar Topography Mission

StaMPS Stanford Method for Persistent Scatterers

TOPS Terrain Observation with Progressive Scan

TRAIN Toolbox for Reducing Atmospheric InSAR Noise

Introduction

Since the launch of the first generation of Synthetic Aperture Radar (SAR) satellites in the 1990s, i.e., the European Remote Sensing satellite (ERS-1 and ERS-2), the Japanese Earth Resources Satellite (JERS-1) and the Radarsat-1, a number of application fields took advantage of the day-and-night and weather-independent data, such as natural hazard assessment, ground deformation studies, investigations on polar cap dynamics, slope failures and instability processes in general (Massonnet and Feigl 1998; Bürgmann et al. 2000; Moreira et al. 2013).
The first proposed technique for the measurement of deformations occurring at the ground was the Differential Interferometric SAR (DInSAR) interferometry relying on the interpretation of interferograms from a couple of SAR images combined with digital elevation models (DEM) to remove the topographic contributions affecting the interferograms (Gabriel et al. 1989; Rosen et al. 2000). In the last two decades, techniques based on the stacking of interferograms were proposed (Ferretti et al. 2000, 2001; Hooper et al. 2004, 2007; Berardino et al. 2002; Lanari et al. 2004a; Schmidt and Bürgmann 2003; Werner et al. 2003; Bert 2006; Crosetto et al. 2008; Ferretti et al. 2011; Perissin and Wang 2011), paving the way to the so-called multi-temporal interferometry. These techniques can provide the displacement of a multitude of specific targets at a very high level of accuracy with significant improvement in spatial density and better delineation of the phenomena at the required spatial scale with respect to geodetic terrestrial surveys. It is important to highlight the relative nature of multi-temporal DInSAR techniques; in fact, they allow to compute the displacements with respect to a reference position and a reference epoch. Therefore, the absolute velocity of one or more points within the studied area is required to transpose the relative displacement field into absolute values in a defined reference frame.
A number of SAR data provided by new SAR constellations, both working at C and X-band, have been made available to support the ever increasing need of long series of data with a suitable spatial resolution required by the scientific community. In particular, for the scope of this dissertation, it is important to mention the Sentinel-1 (S1) and COSMO-SkyMed (CSK) satellites operating at C and X-band, respectively. As far as the former is concerned, the data of the Sentinel-1A and -1B (S1A and S1B) satellites were made available within the framework of the Copernicus program on a free and open access basis providing SAR images at average spatial resolution and with very short revisiting time, thus opening new perspectives for continuous ground-surface monitoring (Geudtner et al. 2014). The long series of data now available and the spatial resolution make S1 data particularly suited for accurate large and medium scale displacement monitoring applications such as subsidence monitoring. Regarding the latter, the high resolution of

CSK data (1 m $\times$ 1 m at best) allows for applications at infrastructure or even building scale, thus paving the way to successive analyses oriented to the structural monitoring based on multi-temporal DInSAR. Moreover, it must be noted that the application of non traditional monitoring techniques is a central issue in the frame of Horizon Europe $2021 - 2027$ programme; indeed, the quantification of possible damages in structures and the successive planning of repair interventions (as a much more sustainable solution rather than demolishing) are grouped under the Pillar 2 "Civil Security for Society" of the mentioned European program. Moreover, these activities fall under the CLUSTER 3 "Civil Security for Society" (Strategic Emerging Topics: Human Wellbeing) for the reduction of losses from natural, accidental and man-made disasters through better societal resilience and improved disaster risk management.

Thesis scope The high number of available data from a number of SAR constellations with always increasing spatial resolution and reduced revisiting time have fostered the development of a multitude of tools and techniques for the processing and analyses of these data. In this framework, there is the need to address how the interferometric satellite data and the SAR-based results can generate valuable information regarding the phenomena occurring at the ground. Moreover, the evaluation of the accuracy of the performed analyses and the achieved results is essential when a trustworthy interpretation of the phenomena is the object of interest.
To this aim, during my PhD, the focus has always been set on the assessment of the uncertainties affecting the achieved results based on error propagation analyses. In particular, both the sources of uncertainties related to the observations and those introduced by the performed procedures have been considered as contributing to the overall final accuracy.
The millimetre-level accuracy, assessed with the above mentioned procedure, complemented with the validation of SAR-based results and the availability of high resolution SAR data[1], paved the way to the investigations performed at building scale. For this reason, the last part of my PhD has been devoted to the assessment of the potentialities of high resolution SAR data in the structural investigations field with a special focus on the performances of the proposed procedure, i.e., on the actual capability to identify the deformation phenomena and to assess the accuracies by which these deformations can be identified.

Thesis outline This dissertation is organised as follows. In Chapter 1, the basics of SAR interferometry required for the comprehension of this thesis are presented along with the developed and most used multi-temporal interferometric techniques. Then, the developed processing strategy is discussed in its two parts (namely, the interferometric and the Persistent Scatterer Interferometry (PSI) processing) and the dual orbit processing is presented, consisting of the calibration, the correction of the PS coordinated after residual topographic error estimation and the decomposition of Line of Sight (LOS) displacement into their vertical and East-West components. Finally, the medium (S1) and high (CSK) resolution data that have been processed and analysed throughout my PhD research activity along with the processing strategies tailored to the above mentioned data are discussed and some conclusions are given.
In Chapter 2, a procedure for the estimation of the uncertainties affecting the calibrated PSI products based on the uncertainties propagation law is presented. Moreover, the

[1]In particular, the Italian Space Agency (ASI) recently provided to Italian Institutional Users the opportunity to have a simplified access to the data from the first and second generation of COSMO-SkyMed mission.

validation of the SAR-based results performed with velocities from Global Navigation Satellite System (GNSS) observations performed at relevant points is reported. Then, the application of the proposed methods are presented; in particular, a dual-orbit S1 dataset over the eastern sector of the Po Plain (Italy) and subsequent analyses are presented. Finally, some discussions of the achieved results (with particular attention to the accuracies related to the PSI-based products and to the performed validation) are proposed and the conclusions are given.
The developed approach for the investigation and separation of ground deformation contributions based on the combination of PS velocities from multi-temporal SAR interferometry and Geographical Information Systems (GIS) analysis is presented in Chapter 3. The selected case study is the municipality of Ravenna (Emilia Romagna, Italy), an area in which subsidence phenomena both from natural and anthropogenic causes occur. In particular, the relationship between displacements occurring over built environment and consolidation processes will be investigated exploiting a dual-orbit Sentinel-1 SAR dataset and descriptive attributes related to the age of construction and intended use over the study area.
In Chapter 4, a method for the evaluation of the potentialities and performances of the multi-temporal satellite interferometric technique for structural investigations of single buildings is proposed. It relies on an analytical procedure for the reconstruction of the 3D rigid motion of isolated buildings based on a dual-orbit SAR dataset along with the evaluation of the uncertainties related to the estimated parameters. To validate the method, numerical simulations are also proposed. Finally, the processing and the analysis of a high-resolution COSMO-SkyMed dataset over the metropolitan area of city of Rome (Italy) are performed and the achievable accuracies are assessed and discussed.

Chapter 1

Synthetic Aperture Radar Interferometry basics and processing strategy

In this Chapter, the main theoretical concepts behind the multi-temporal SAR Interferometry and the developed workflow are presented along with implementation details. First, the theory of satellite interferometric techniques is briefly presented. Then, the focus is set to the SAR products processing workflow developed during my PhD activity outlining the interferometric and the PSI processing. Moreover, the combined processing of a dual-orbit set of SAR products is discussed and the employed open-source software are briefly presented. Finally, the medium resolution Sentinel-1 and high resolution COSMO-SkyMed data and the processing strategy tailored to these data are introduced and some conclusions are given.

1.1 Introduction

In the last three decades, Synthetic Aperture Radar Interferometry has become an effective technique in different application focused on ground deformation phenomena. Differential SAR interferometry was initially used to measure deformation of the land surface through interpretation of interferograms, combined with digital elevation models to remove the topographic contributions. DEM were obtained with the SAR interferometry by using one or two additional SAR images and it was called three, or four, pass interferometry, respectively. Today, approaches based on the stacking of interferograms are adopted more frequently, and the methodologies can be differentiated into persistent scatterer interferometry, small baseline subsets (SBAS), and methods based on the search of distributed scatterers rather than the persistent ones (Homogeneous Distributed Scatterer Interferometry, HDSI). These PSI (Ferretti et al. 2000, 2001; Hooper et al. 2004, 2007), SBAS (Berardino et al. 2002; Lanari et al. 2004b), and HDSI (Ferretti et al. 2011) methods require different strategies for the generation of the interferogram stacks and the statistical approach to find the velocity of stable and highly coherent scatterers from the time series of displacement between satellite passes. Regardless of the methodology used, one of the main advantages with respect to geodetic terrestrial surveys is that it is possible to find the displacement of a multitude of points with significant improvement in spatial density, and better delineation of the displacement phenomena at the required spatial scale. These methodologies are

based on differential approaches, and the derived displacements are referred to a reference position. Thus, the absolute velocity of the scatterers is required whenever the relative displacement field must be transposed into an absolute reference frame.
Others major limitations can be associated with spatial and temporal decorrelation phenomena, image gaps, the impossibility to detect fast motions due to the used wavelengths (typically the C and X bands are employed), and the ability to detect a minor part of the actual displacements due to the sampling along the slant direction. In particular, also depending on the acquisition geometry, the methodologies are more sensitive towards displacements occurring along the vertical and East-West directions. To obtain the final velocity field in a geodetic reference frame, displacements along the vertical and horizontal directions are required and a vector decomposition analysis must be applied.
In the last years, within the framework of the Copernicus Earth Observation programme, Sentinel-1A and Sentinel-1B satellites equipped with C-band radar sensors were launched in 2014 and 2016, respectively, as part of the Sentinel constellation of satellites. Under the umbrella of Copernicus, the European Space Agency (ESA) started to provide worldwide free-access SAR images at average spatial resolution and with very short revisiting times, which opened new perspectives for continuous ground-surface monitoring (Geudtner et al. 2014). In addition, users now have the opportunity to process SAR images using trusted and freely accessible toolboxes. Over the last years, the ESA has distributed the Sentinel Application Platform (SNAP) software with incorporated utilities for interferogram generation and stacking, complemented by the Statistical Cost Network Flow Algorithm for Phase Unwrapping (SNAPHU) package for phase unwrapping (Chen and Zebker 2000, 2001, 2002). The displacement histories of specific targets can be derived from the stacks of interferograms using the free Stanford Method for Persistent Scatterers (StaMPS) tool, which only requires interferograms from the SNAP since it uses an unwrapping algorithm derived from SNAPHU (Hooper and Zebker 2007). To date, studies have explored the combined use of SNAP and StaMPS for displacement analysis (e.g., Cian et al. (2019); Delgado Blasco et al. (2019); Foumelis et al. (2018)); however, only few of them rely on the processing of dual orbit set of data and are complemented by a decomposition analysis, a procedure to align PSI products to a global reference frame and the computation of the residual errors due to the DEM employed in the interferometric processing with successive correction of the PS coordinates.
To cover this gap, in this Chapter, the strategies adopted in the PSI processing of dual-orbit data using the SNAP and StaMPS open-source routines are introduced, in which the atmospheric contribution is evaluated and subtracted from the interferometric phase using the Toolbox for Reducing Atmospheric InSAR Noise (TRAIN) (Bekaert et al. 2015a,b). Moreover, a procedure to refer single orbit slant products to a global reference frame (i.e., calibration) has been developed exploiting GNSS observations along with a decomposition analysis to reconstruct the vertical and East-West oriented displacement. The residual topographic error is also estimated and the PS coordinates are corrected accordingly; this can be particularly useful in certain applications for which an accurate positioning of the targets is required.

1.2 Synthetic Aperture Radar Interferometry basics

In this Section, a brief overview on SAR sensors and SAR interferometry strictly necessary for this dissertation is given. For an extensive description of the covered topics, please refer to Hanssen (2001); Moreira et al. (2013); Curlander and McDonough (1991).

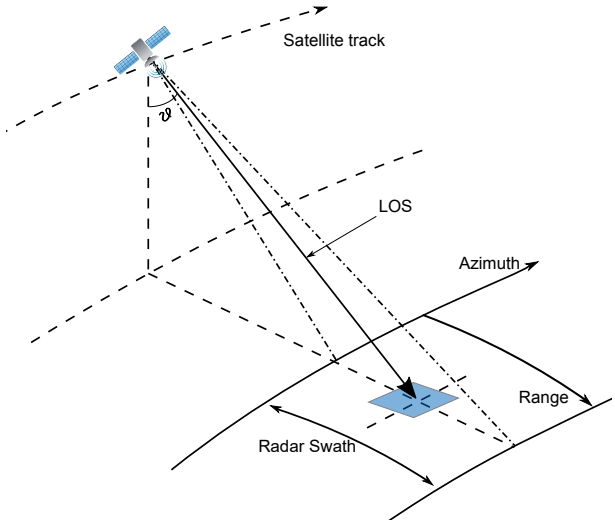

Figure 1.1: Satellite Synthetic Aperture Radar acquisition geometry.

Synthetic Aperture Radars are side-looking imaging radars which transmit electromagnetic pulses and collect the backscattered part of the signal through the antenna mounted on the same platform. SAR sensors transmit frequency modulated pulsed waveforms, the chirp signals, whose amplitude remains constant during the pulse time. The transmission time is then followed by a period in which the system receives and collects the backscattered echoes. The repeat cycle of the described procedure (the alternation between the transmission and receiving) is given by the Pulse Repetition Interval (PRI).
A simple acquisition geometry is presented in Figure 1.1 and described in the following. The SAR sensor and the antenna are mounted on a satellite that moves along its orbit (satellite track or along-track direction). While moving, the pulses are sent towards the ground along the LOS, perpendicular to the orbit and forming a look angle θ with the vertical from the satellite to the ground. The slanted geometry (typically right-looking) avoids ambiguous range reflections. At the ground, the projection of the satellite track is defined as the azimuth direction, while the range is the direction perpendicular to the azimuth.
The resolution of the images (i.e., the dimension of the cell at the ground that is mapped to a single pixel) can be expressed in ground range (range in Figure 1.1) and in azimuth. In particular, the ground range resolution can be expressed as

$$\delta_{gr} = \frac{c}{2B \sin\theta} \tag{1.1}$$

in which B is the system bandwidth and c is the light speed and θ is the look angle; while the azimuth resolution is given by

$$\delta_a = r_0 \frac{\lambda}{2L_{sa}} \tag{1.2}$$

where r_0 is the distance between the satellite and the target at the ground, λ is the radar wavelength and L_{sa} is the synthetic aperture length of the antenna that is simulated exploiting the movement of the platform along its path. The longer virtual aperture allows to increase the azimuth resolution to an appropriate value for imaging purposes.

Synthetic Aperture Radar data The SAR image is expressed by a regular grid of complex numbers whose amplitude and phase are related to the intensity and the time

delay of the backscattered signal, respectively (Hanssen 2001). Let us consider two SAR acquisitions y_1 and y_2 taken at epochs 1 and 2

$$y_1 = |y_1| \exp(j\psi_1)$$
$$y_2 = |y_2| \exp(j\psi_2)$$

After the alignment of the images and the computation of the complex interferogram (i.e. the pointwise complex multiplication between y_1 and y_2^*), the interferometric phase for a resolution cell x is given by

$$\psi_x = \psi_{x,1} - \psi_{x,2} = -\frac{4\pi\Delta R}{\lambda} \tag{1.3}$$

The interferometric phase in repeat-pass observations is sensitive to both surface topography (topo) and to the ground displacement (defo) of the scatterer occurred between the two passes along the LOS direction and it can be expressed by (Rosen et al. 1996, 2000)

$$\psi_x = -\frac{4\pi B_{\perp,0}}{\lambda}\frac{z}{r\sin\theta_0} + \frac{4\pi\Delta r}{\lambda} = \phi_{\text{topo}} + \phi_{\text{defo}} \tag{1.4}$$

in which $B_{\perp,0}$ is the perpendicular component of the baseline (B) referenced to the flat Earth, z is the topographic height, r is the range between the satellite and the target at the ground, θ_0 is the look angle for the considered resolution cell and Δr is the range variation caused by the target displacement. From Equation (1.4), the two main applications of SAR interferometry can be evidenced: the DEM computation (when the deformation component can be neglected) and the computation of the occurred LOS displacement. The latter can be performed estimating and subtracting the topographic component, when a DEM of the imaged scene is available (Crosetto et al. 2016). In this dissertation, the LOS displacement estimation of targets at the ground is the application of interest.
Before going in detail into the techniques for the displacement estimation from SAR data, a premise regarding the geometry of acquisition and how the displacement components can be detected by a SAR system is necessary. As shown in Figure 1.2, SAR satellite system are able to detect only the projection along the LOS of the displacement occurring at the ground (or real displacement); therefore, the magnitude of the detected displacement will be always a fraction of the actual displacement.

Interferometric techniques The DInSAR was the first developed satellite interferometric technique. The DInSAR is a two-pass interferometric technique; therefore, it exploits two SAR images taken from the same platform at two different epochs and an external DEM to compute displacements in the order of centimetres (Gabriel et al. 1989). The first applications to take advantage of the DInSAR were linked to the assessment of the displacement occurred after geophysical phenomena such as seismic or volcanic events. The main products of the technique are the generated interferograms, which represent the spatial trend of the interferometric phase, and, after phase unwrapping and the conversion of phases into displacements, the deformation map over the imaged area. The limitations of the DInSAR technique are related to the possibility to depict only the displacement occurring between two satellite passes, the possible occurrence of decorrelation phenomena and atmospheric disturbances and the unsuitability to depict small-magnitude phenomena (i.e., in the order of few millimetres) due to the poor achievable accuracy.

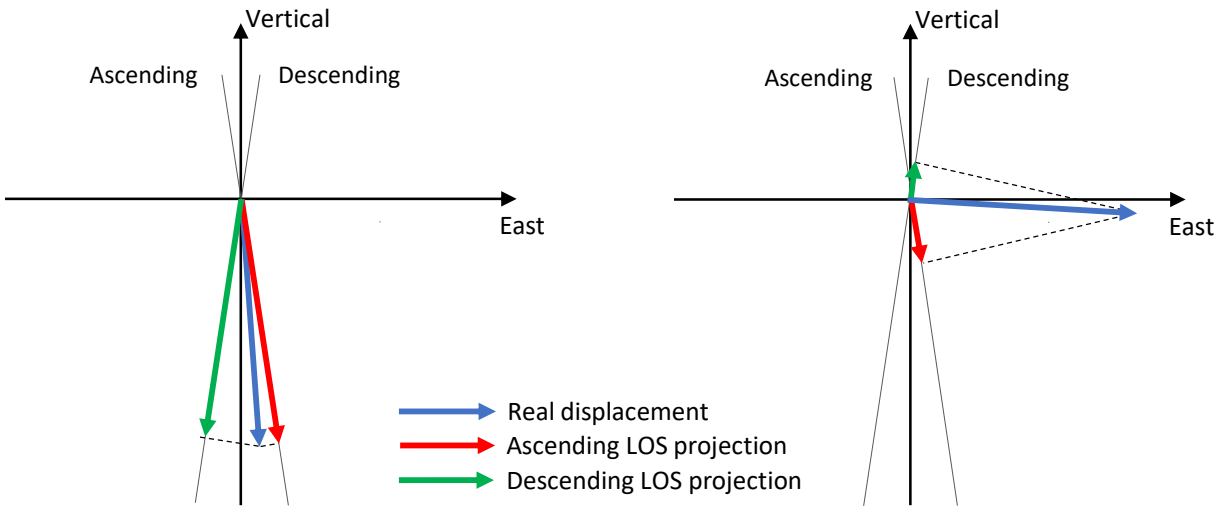

Figure 1.2: The displacements as detected by the line of sight directions.

In the last two decades, more advanced techniques have been proposed to overcome the limitations of two-pass interferometry relying on the analysis of a set of images. In particular, different multi-temporal interferometric techniques were proposed enabling the reconstruction of the displacement history of selected targets at the ground with a millimetre accuracy; this is performed extracting the phase component related to the displacement from the observed phase value. Considering a more complete version of Equation (1.4) after the removal of the topographic phase contribution and the phase unwrapping, the following expression holds

$$\phi_x = \phi_{\text{defo}} + \phi_{\text{res,topo}} + \phi_{\text{atm}} + \phi_{\text{noise}} + 2k\pi \tag{1.5}$$

in which $\phi_{\text{res,topo}}$ is the residual topographic phase, ϕ_{atm} is the atmospheric phase contribution, ϕ_{noise} represents the phase noise and k is the integer phase ambiguity of the phase unwrapping procedure.

The first advanced DInSAR technique proposed in literature was the Permanent Scatterer Interferometry (PSInSAR™) by Ferretti et al. (2001) relying on the identification of highly coherent targets, the so called Permanent Scatterers (PS) from a set of $(N-1)$ interferograms (where N is the total number of the processed SAR images) computed with respect to the same master image. The main step of the PSInSAR™ can be summarized as follows: a) interferograms and differential interferograms generation, b) PS selection, c) preliminary estimate of PS LOS motion (adopting a constant velocity model), residual topography and atmospheric phase contributions, d) refinement of the previous step.

The main drawback are related to 1) the inability to identify as PS targets whose motion does not follow a linear model or, in other cases, the fact that the non-linear part of the target motion is considered as atmospheric disturbance and 2) low number of targets found in non-urban areas due to the high coherence required during the PS selection step. To face the first, an advanced version of the PSInSAR™ has been presented in Ferretti et al. (2000) relying on a stochastic model. In the proposed approach, the target motion estimation is performed with a sub-optimal spatio-temporal filter applied to unwrapped PS phase.

In the years immediately after, another fundamental multi-temporal interferometric technique has been proposed (Berardino et al. 2002; Lanari et al. 2004b): the so-called small-baseline subset (SBAS) technique. The main idea of the SBAS technique is the

computation of interferograms between pair of images characterized by a short baseline to reduce the spatial decorrelation phenomena. The results achieved by the application of the SBAS technique include a shorter temporal baseline and a higher targets density with respect to the standard PS approach.
Other valuable techniques have been developed and proposed (Schmidt and Bürgmann 2003; Werner et al. 2003; Bert 2006; Crosetto et al. 2008; Costantini et al. 2008; Ferretti et al. 2011; Perissin and Wang 2011) differencing for the combination method for the interferograms generation (mainly the single master and the small baseline configurations) and the criterion for the selection of stable targets. For the scope of this dissertation, it is important to mention the method developed by Hooper et al. (2004, 2007) and implemented in the StaMPS software. In this approach, a method for the extraction of PS pixel as the dominant scatterer in a resolution cell and the computation of the displacement history of them is proposed without the need of an a-priori deformation model. The PS method developed by Hooper et al., makes it possible to find PS pixels also in area where few man-made structures are present and to compute the displacement time series of these targets also in case of deformations occurring at variable time rate. More information regarding the StaMPS method will be given in Section 1.3.

1.3 The developed processing strategy

The developed processing workflow is composed of two parts: the interferometric processing carried out in SNAP and the PSI processing performed in the StaMPS environment (Figure 1.3). In the following, each part constituting the processing is described along with theoretical principals. Further details regarding the software will be given in Section 1.3.4.

1.3.1 Interferometric processing

As far as the first part of the processing is concerned, the main steps are the selection of the optimum master image, the coregistration, the formation of the interferograms and the topographic phase component removal from the interferograms.

Selection of the master The selection of the master image might have a significant role in the effectiveness of the whole procedure and is based on the minimization of the geometrical and temporal decorrelation effects (Rucci et al. 2012; Ferretti et al. 2000; Crosetto et al. 2016). The joint effects of the sources of decorrelation are considered, with estimation of the total correlation coefficient between the (i, j) pair of images (Zebker and Villasenor 1992),

$$\begin{aligned}\rho_{i,j} &= \rho^{\mathrm{T}}_{i,j} \cdot \rho^{\mathrm{S}}_{i,j} \cdot \rho^{\mathrm{D}}_{i,j} \cdot \rho^{\mathrm{Th}}_{i,j} \\ &\approx \left(1 - f\left(\frac{T}{T_C}\right)\right)_{i,j} \cdot \left(1 - f\left(\frac{B_\perp}{B_{\perp,C}}\right)\right)_{i,j} \cdot \left(1 - f\left(\frac{F_{DC}}{F_{DC,C}}\right)\right)_{i,j} \cdot \rho^{\mathrm{Th}}_{i,j}\end{aligned} \tag{1.6}$$

where

$$f(y) = \begin{cases} y & \text{for } y \leq 1 \\ 1 & \text{for } y > 1 \end{cases} \tag{1.7}$$

and $\rho^{\mathrm{T}}_{i,j}$, $\rho^{\mathrm{S}}_{i,j}$, $\rho^{\mathrm{D}}_{i,j}$, $\rho^{\mathrm{Th}}_{i,j}$ are the temporal, spatial, Doppler and thermal correlation coefficients respectively, $B_\perp$ is the perpendicular baseline, T is the temporal baseline and

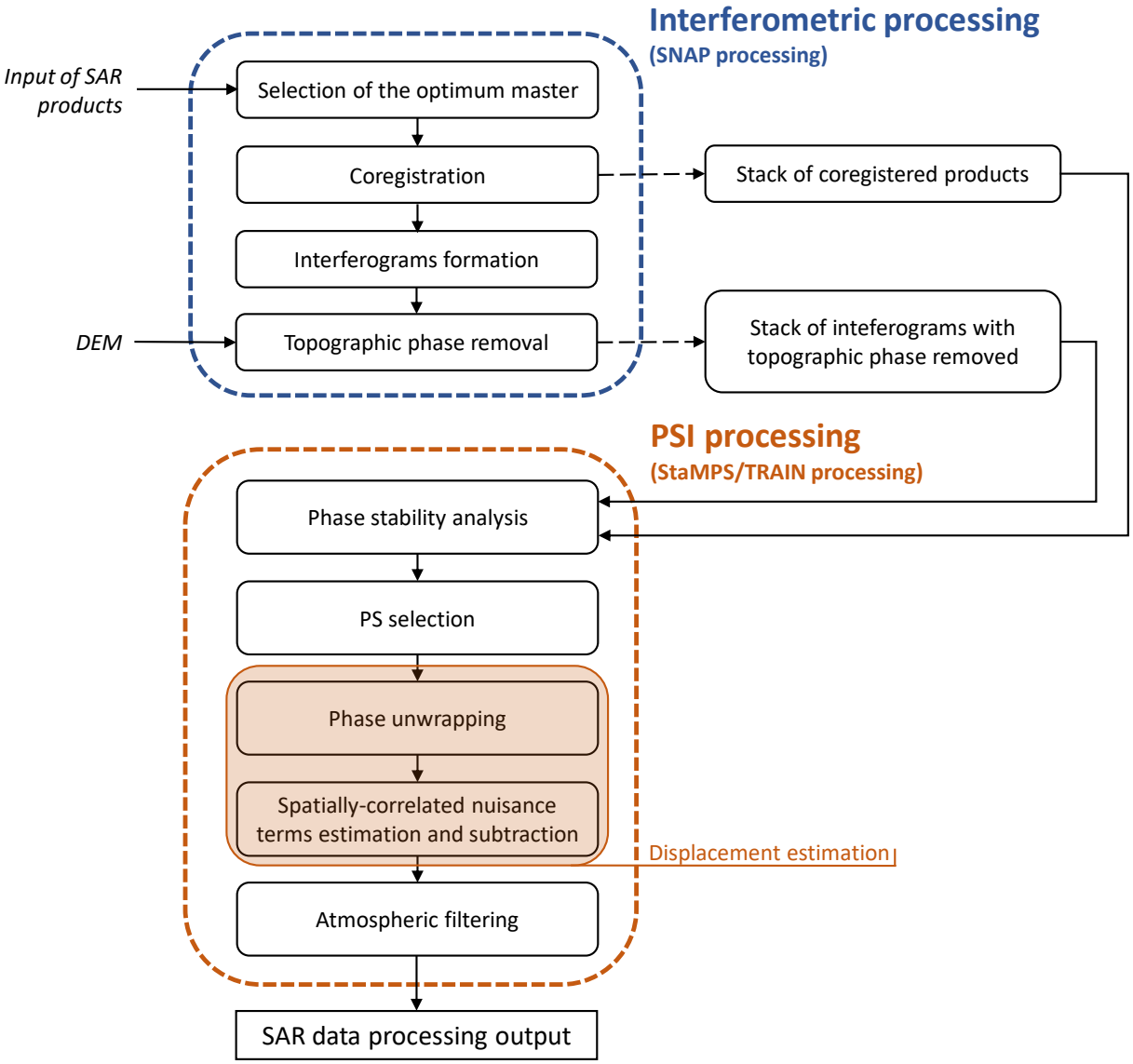

Figure 1.3: The SNAP-StaMPS workflow developed for the processing of Synthetic Aperture Radar data.

F_{DC} is the Doppler centre frequency difference between two images. The terms with the pedex C denote the critical values. The master is selected between the set of images as the image whose index satisfies

$$\hat{m} = \max_{i \in \{1,\dots,N\}} \sum_{\substack{j=1 \\ j \neq i}}^{N} \rho_{i,j} \tag{1.8}$$

where i and j are the images indices and N is the total number of images.

Coregistration The precise (i.e. sub-pixel) registration of the SAR images with respect to the master is a critical step in the interferometric processing since it improves the interferometric coherence and the accuracy of the unwrapping and interferograms computation procedures (Hanssen 2001; Scheiber and Moreira 2000). The aligment is performed through a cross-correlation technique that could be slow for large search windows; for this reason, the procedure is divided in two steps: the coarse and fine registration in which the

offsets are approximated and the sub-pixel alignment accuracy is obtained, respectively. Then, the coregistration polynomial is computed and the resampling of the slaves to the master geometry is performed.

Interferograms formation A complex interferogram is computed as the pointwise complex multiplication between the phasors of the master (m) and the complex conjugate of the slave (s) images. Extracting the phase of the complex interferogram, the interferometric phase for a resolution cell x can be expressed as

$$\psi_x = \angle(y_m y_s^*) = \psi_{x,m} - \psi_{x,s} \tag{1.9}$$

where $\psi_{x,m}$ and $\psi_{x,s}$ are the observed phase values for master and slave, respectively. After the computation of the interferograms, the phase component due to the curvature of the reference body is computed and subtracted. For this purpose, the WGS84 ellipsoid is usually considered.

Topographic phase removal In order to obtain the deformation content of the interferometric phase, the topographic phase has to be computed and removed from the complex interferogram exploiting a DEM. First, the DEM is resampled to the radar master image geometry (i.e., radarcoded). Then, the DEM phase is computed and interpolated to the grid of the master image. Finally, the topographic phase can be subtracted from the interferometric phase.

1.3.2 Persistent Scatterer Interferometry processing

The stack of coregistered products and the stack of interferograms without the topographic phase contribution are the products needed for the PSI processing.
The developed workflow for the selection of persistent scatterers and the computation of their displacement history follows the theory of the persistent scatterer InSAR technique. The basic method identify and select persistent scatterers relying on the smilarity between the phase history of the target and the one assumed as the functional deformation model (Ferretti et al. 2001). Since the estimation of the targets deformation in time is the aim of the interferometric techniques application, the basic approach can be limiting. The method proposed in Hooper et al. (2004, 2007) and implemented in StaMPS selects the PS pixels exploiting the spatially correlated nature of the deformation without the need of a-priori assumptions on the deformation model. In the following the adopted procedure is described.

Phase stability analysis and selection of the Persistent Scatterers The preliminary selection of the PS pixels is based on an amplitude analysis, as presented in Ferretti et al. (2001), Sec. III.C. First, exploiting the statistical relationship between the amplitude and phase stability, the amplitude dispersion (D_A) is used as a threshold value: in fact, a high value is set to speed up the processing and include almost all the PS pixels. The amplitude dispersion for each pixel is defined as

$$D_A = \frac{\sigma_A}{\mu_A} \tag{1.10}$$

where σ_A is the standard deviation, and μ_A is the mean of the amplitude of the pixel. Then, the phase stability of each pixel is analyzed by estimating the phase noise contribution through an iterative process and checking that it does not obscure the displacement term.

The wrapped phase of the x-th pixel and the i-th interferogram is expressed by (Hooper et al. 2007, Eq. (10))

$$\psi_{x,i} = W\{\phi_{D,x,i} + \phi_{A,x,i} + \Delta\phi_{S,x,i} + \Delta\phi_{\theta,x,i} + \Delta\phi_{N,x,i}\} \tag{1.11}$$

where $W\{\cdot\}$ is the modulo 2π wrapping operator, $\phi_{D,x,i}$ is the phase change due to displacement along the LOS, $\phi_{A,x,i}$ is the phase contribution due to atmospheric refraction, $\Delta\phi_{S,x,i}$ is the residual phase depending on the satellite orbit inaccuracies, $\Delta\phi_{\theta,x,i}$ is the residual phase due to look angle error and $\Delta\phi_{N,x,i}$ is the phase noise term. The first three terms and part of the fourth of Equation (1.11) are assumed to be spatially correlated, hence, the estimation of the spatially correlated part of $\psi_{x,i}$ ($\tilde{\psi}_{x,i}$) gives an estimate for these terms. The described operation is implemented in Hooper et al. (2007) with a band pass filter as an adaptive phase filter combined with a low pass filter in the frequency domain. Then, subtracting the spatially correlated estimate of the wrapped phase and the estimation of the uncorrelated part of the residual phase due to look angle error performed with a least square procedure, a measure of the variation of the residual phase of each pixel from the N interferograms can be defined as

$$\gamma_x = \frac{1}{N}\Big|\sum_{i=1}^{N} \exp(\sqrt{-1}(\psi_{x,i} - \tilde{\psi}_{x,i} - \Delta\hat{\phi}^{u}_{\theta,x,i}))\Big| \tag{1.12}$$

where the apex u denotes the uncorrelated part of the term.

Under the hypothesis of spatial uncorrelation of the phase noise term, γ_x is a measure of the phase noise and can be used to determine whether a pixel is a persistent scatterer with the procedure described in Hooper et al. (2007).

Displacement estimation After the selection of the PS, the contribution to the phase of the displacement ($\phi_{D,x,i}$) can be estimated from Equation (1.11) after phase unwrapping and the estimation and cancellation of nuisance terms. The unwrapping procedure aims at computing non-ambiguous phase from modulo 2π phase values. The results of the procedure can be written as

$$\hat{\phi}_{x,i} = \phi_{D,x,i} + \phi_{A,x,i} + \Delta\phi_{S,x,i} + \Delta\phi_{\theta,x,i} + \Delta\phi_{N,x,i} + 2k_{x,i}\pi \tag{1.13}$$

in which $\hat{\phi}_{x,i}$ is the unwrapped phase estimate and $k_{x,i}$ is the integer ambiguity associated to pixel x of the interferogram i.
Then the nuisance terms that could mask the displacement contribution have to be estimated. The spatially uncorrelated part of these nuisance terms can be modelled as noise, while the spatially correlated contributions are estimated using a combination of spatial and temporal filters dividing them into two parts: one correlated and the other non-correlated in time. The details of the procedure is extensively described in Hooper et al. (2007), Sec. 5.2. The estimates of the nuisance terms are then subtracted to the unwrapped phase to give an estimate of the phase displacement.

Atmospheric filtering The atmosphere can affect the radar signal and the main contributions can be accounted as ionospheric effects and tropospheric effects. The former is due to the variation of free electrons number along the travel path of the signal; this effect is significant as the frequency of the radar signal decreases. Regarding the latter, the variations in temperature, pressure and relative humidity of the troposphere can affect the signal with a significant magnitude causing a spatially varying delay of the signal itself (Bekaert

et al. 2015a,b). In this dissertation, only the corrections of the tropospheric effects on the signal will be taken into account. Different approaches have been proposed in literature: corrections based on weather models information, GNSS observations, spectrometers data or phase-based models. The main limitations of the first three corrections are related to their low spatial and temporal resolution; however in case of cloud-free and daylight data, the spectrometers ensure the best performances while weather models can outperform when turbulences are present. To overcome the drawbacks of the first three methods, a linear or quadratic relation can be taken into account between the tropospheric delay and the topography in areas not subjected to deformations. More detailed information regarding the available correction methods and their description can be found in Bekaert et al. (2015b).

1.3.3 Dual orbit processing

The interferometric processing described in Sections 1.3.1 and 1.3.2 is performed for an ascending and a descending dataset. Then, these two sets of LOS-projected velocities are calibrated to obtain velocities in an absolute reference frame and combined to retrieve the vertical and East-West velocity components. Moreover, a procedure for the computation of the residual topographic error and the correction of the PS coordinated according to it has been devised. The developed procedure is presented in detail in the following and in Figure 1.4.

Calibration The calibration procedure of the SAR velocities exploiting GNSS observations aims at constraining and aligning the slant-oriented velocities to a global reference frame. More specifically, the GNSS vertical and horizontal (namely, East-West and North-South) velocities are projected along the ascending and descending LOS directions as

$$\begin{cases} v_{\mathrm{LOS,asc}}^{\mathrm{GNSS}} = v_{\mathrm{up}} \cos(\theta_{\mathrm{asc}}) - \sin(\theta_{\mathrm{asc}})[-v_{\mathrm{n}} \sin(\alpha_{\mathrm{asc}}) + v_{\mathrm{e}} \cos(\alpha_{\mathrm{asc}})] \\ v_{\mathrm{LOS,desc}}^{\mathrm{GNSS}} = v_{\mathrm{up}} \cos(\theta_{\mathrm{desc}}) - \sin(\theta_{\mathrm{desc}})[-v_{\mathrm{n}} \sin(\alpha_{\mathrm{desc}}) + v_{\mathrm{e}} \cos(\alpha_{\mathrm{desc}})] \end{cases} \tag{1.14}$$

where v_{up}, v_{n} and v_{e} are the vertical, North-South and East-West GNSS velocity components.
Then, for each orbit processing, the mean velocity value of the PSs in proximity to the GNSS station is aligned with the value computed from Equation (1.14) and the velocities of all the other processed PSs are scaled accordingly. The outcome of the described procedure are the ascending and descending sets of calibrated LOS velocities.

Correction of the PS coordinates after residual topographic error estimation The interferometric phase as expressed in Equation (1.5) contains the phase contribution due to residual topography after the topographic phase removal procedure ($\phi_{\mathrm{res,topo}}$); this contribution can be due to inaccuracies in the employed DEM or objects at the ground that are not accounted for in the elevation model (Perissin and Rocca 2006; Jung et al. 2019). In particular, the PS is placed on the surface of the DEM at the satellite-target distance that is detected by the sensor itself (point 1 in Figure 1.5). However, as previously recalled, if structures not detected by the DEM or inaccuracies of the model occur, the target is incorrectly positioned and it must be placed at the same distance from the satellite but at a different elevation (point 2 in Figure 1.5). The difference between the elevations of the two planimetric positions of the PS, is called topographic error (ΔH). Given that

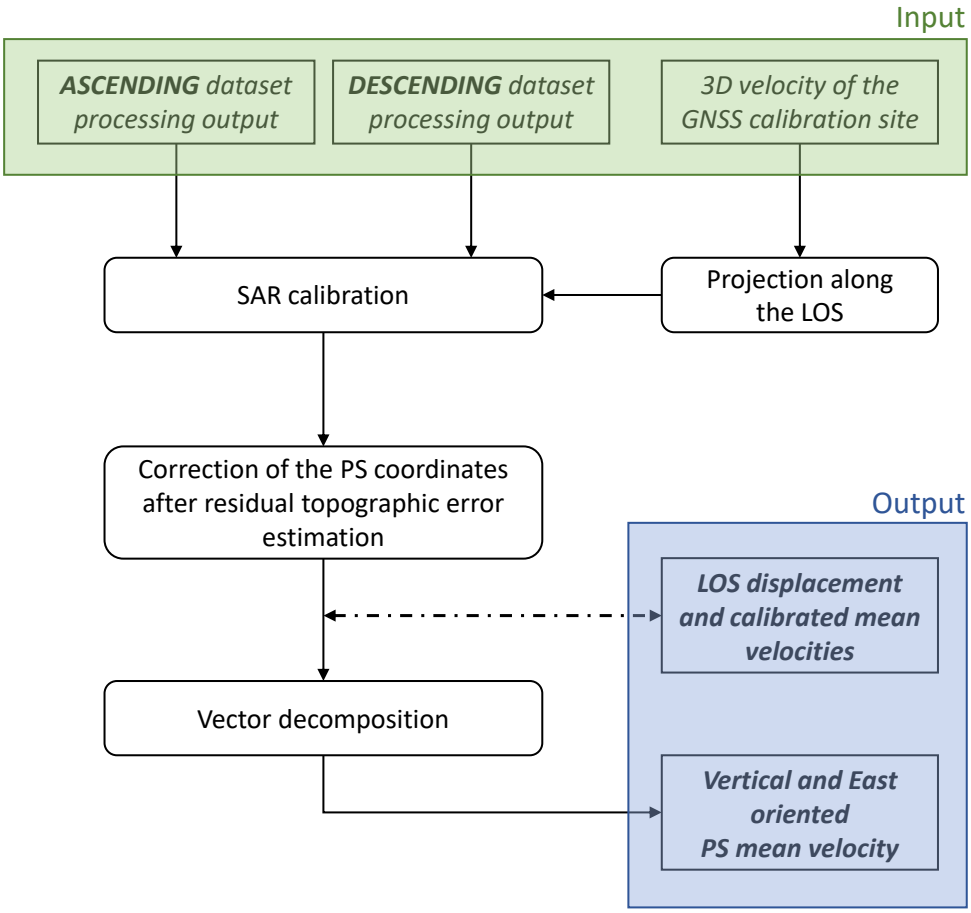

Figure 1.4: The developed workflow for the calibration and decomposition of the mean Line of Sight velocities and the correction of the Persistent Scatterers coordinates after the computation of the residual topographic error.

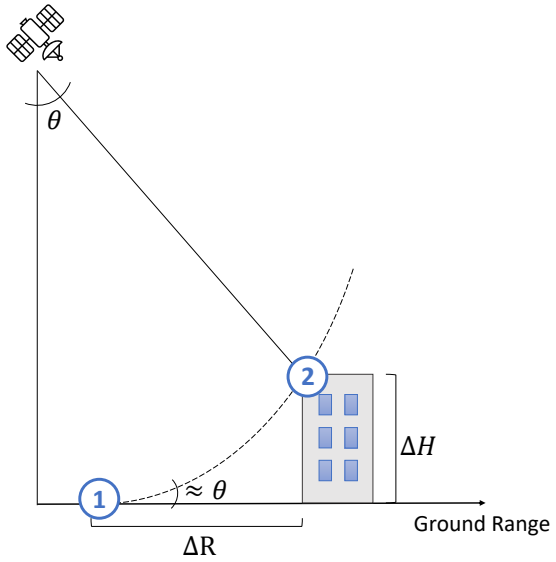

Figure 1.5: The topographic error in case of a structure not detected by the digital elevation model.

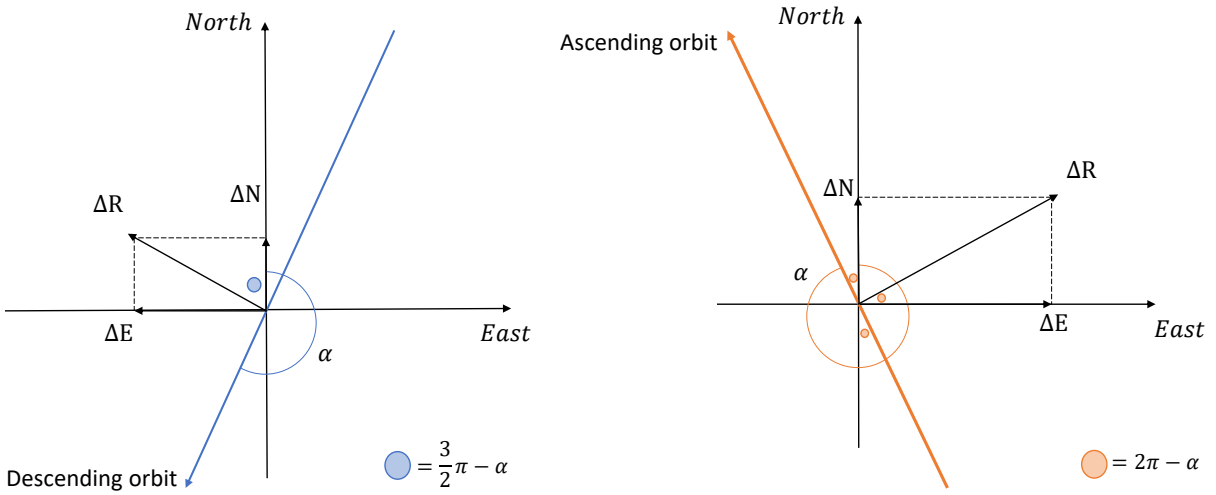

Figure 1.6: The North and East components of Persistent Scatterers position correction.

the acquisition geometry is known (i.e. the angle of incidence (θ) and the heading angle (α)) and under the validity of the far field approximation, it is possible to compute the correction in positioning along the ground range (ΔR in Figure 1.5)

$$\Delta R = \Delta H \cot \theta \tag{1.15}$$

and its components along the North (ΔN) and East (ΔE) directions for both orbits (Figure 1.6)

$$\begin{cases} \Delta N = -\Delta R \sin \alpha \\ \Delta E = \Delta R \cos \alpha \end{cases} \tag{1.16}$$

Once the corrections to be made to the North and East components are known, the coordinates of each PS can be updated.
More information on the implemented procedure will be given in Section 1.3.4.

Decomposition The decomposition procedure aim is to combine the ascending and descending calibrated LOS velocities to compute the vertical and horizontal velocity components.
As stated in Hanssen (2001) and Samieie-Esfahany et al. (2009), the LOS-oriented ascending and descending displacements can be decomposed into the actual displacements along the vertical and horizontal directions. For a satellite orbit with heading α, the mean velocity along the LOS can be expressed by

$$v_{\text{LOS}} = v_{\text{up}} \cos(\theta) - \sin(\theta)(v_{\text{n}} \cos(\alpha - 3\pi/2) + v_{\text{e}} \sin(\alpha - 3\pi/2)) \tag{1.17}$$

where the mean velocity is considered, instead of the displacement as in Hanssen (2001), without losing the validity of the discussion. In Equation (1.17), θ is the local incidence angle, v_{up}, v_{n}, v_{e} are the components of the mean velocity along the vertical, North-South and East-West directions, respectively. Typically, the sensitivity of SAR satellite systems to the North-South displacement component is very low (Hanssen 2001); for instance, the Sentinel-1 constellation was designed to have a heading angle of 190° and a mean incidence angle of 37°, giving a sensitivity of -0.10 to the North-South direction. For this reason, the decomposition procedure was developed to compute the displacement components

along the vertical and East-West directions only from the ascending and descending passes of the satellites as

$$\begin{cases} v_{\mathrm{LOS,asc}} = v_{\mathrm{up}} \cos(\theta_{\mathrm{asc}}) - v_{\mathrm{e}} \sin(\theta_{\mathrm{asc}}) \cos(\alpha_{\mathrm{asc}}) \\ v_{\mathrm{LOS,desc}} = v_{\mathrm{up}} \cos(\theta_{\mathrm{desc}}) - v_{\mathrm{e}} \sin(\theta_{\mathrm{desc}}) \cos(\alpha_{\mathrm{desc}}) \end{cases} \tag{1.18}$$

Inverting the equations and re-writing the system with the matrix notation, the decomposition procedure is expressed by

$$\begin{bmatrix} v_{\mathrm{up}} \\ v_{\mathrm{e}} \end{bmatrix} = A^{-1} \begin{bmatrix} v_{\mathrm{LOS}}^{\mathrm{asc}} \\ v_{\mathrm{LOS}}^{\mathrm{desc}} \end{bmatrix} \tag{1.19}$$

where

$$A = \begin{bmatrix} \cos(\theta_{\mathrm{asc}}) & -\sin(\theta_{\mathrm{asc}}) \cos(\alpha_{\mathrm{asc}}) \\ \cos(\theta_{\mathrm{desc}}) & -\sin(\theta_{\mathrm{desc}}) \cos(\alpha_{\mathrm{desc}}) \end{bmatrix}$$

1.3.4 Software

The proposed workflow was developed with free and open-source software complemented by MATLAB routines specifically introduced to complete the processing with the calibration, decomposition and the correction of the PSs coordinates.

SNAP SNAP[1] is an architecture that is provided by the ESA and incorporates all the Sentinel Toolboxes for the analysis and processing of Earth Observation (EO) data. In particular, the Sentinel-1 Toolbox includes the functionalities for the interferometric processing of both ESA (e.g., Sentinel-1, ERS-1, ERS-2, Envisat) and third party (e.g., COSMO-SkyMed, Radarsat-2, TerraSAR-X, ALOS PALSAR) SAR missions.

StaMPS StaMPS[2] is a software package for PSI processing developed by Stanford University, University of Iceland, Delft University of Technology and the University of Leeds. StaMPS is able to compute the time series of targets deformations without the need of a-priori deformation model taking into account the spatially correlated nature of the deformation (Hooper et al. 2004).

SNAPHU The unwrapping operation was accomplished with the software SNAPHU[3]. The package SNAPHU is the implementation of the Statistical-cost, Network-flow Algorithm for Phase Unwrapping proposed by Chen and Zebker (2000, 2001, 2002) and it is compatible both with SNAP and StaMPS software. The unwrapping algorithm is based on a maximum a posteriori probability estimation approach to compute the most likely unwrapped solution given the wrapped phase, the image intensity and the interferometric coherence as observables. Three different statistical models for topography, deformation and smooth generic data are proposed to derive models for the joint statistic of the estimated solutions and the observed signal. Moreover non-linear cost functions are employed to describe the relationship between the derived models and network-flow techniques are used to approximate the maximum a posteriori probability solution.

[1]Link to the webpage: `https://earth.esa.int/eogateway/tools/snap`
[2]Link to the webpage: `https://homepages.see.leeds.ac.uk/~earahoo/stamps/`
[3]Link to the webpage: `https://web.stanford.edu/group/radar/softwareandlinks/sw/snaphu/`

TRAIN The TRAIN[4], developed by the University of Leeds, includes the current state of the art tropospheric correction methods. The toolbox is compatible with StaMPS and can be used independently from the InSAR processor as long as the interferometric data follow a specific convention. The following correction methods are included in the TRAIN toolbox: the phase-based linear and power-law corrections, spectrometer correction (Moderate/Medium Resolution Imaging Spectrometer (MODIS/MERIS)), weather model correction (European Reanalysis-Interim (ERA-I)), Modern-Era Retrospective Analysis for Research and Applications (MERRA/MERRA-2), Generic Atmospheric Correction Online Service (GACOS), Weather Research and Forecasting model. For further information, refer to Bekaert et al. (2015a,b).

Calibration, decomposition and correction of PS coordinates The calibration and decomposition procedures were implemented in MATLAB following the methods described in Section 1.3.3.

Calibration The calibration algorithm consists of: a) the extraction of the incidence angle of the nearest PS with respect to the calibration GNSS station for the computation of the GNSS velocity projected along the LOS direction according to Equation (1.14), b) the computation of the mean of the mean PS velocities belonging to a selected circular area centred on the GNSS station with the radius defined by the user, c) the computation of the difference between the LOS-projected GNSS velocity and the mean PS velocity

$$\Delta v_{\text{asc}} = v^{\text{GNSS}}_{\text{LOS,asc}} - \frac{\sum_{i=1}^{N} v^{\text{PS}}_{\text{LOS,asc},i}}{N}$$
$$\Delta v_{\text{desc}} = v^{\text{GNSS}}_{\text{LOS,desc}} - \frac{\sum_{j=1}^{M} v^{\text{PS}}_{\text{LOS,desc},i}}{M}$$

where N and M are the total number of ascending and descending PS contained in the selected circular area with a radius R and centred on the GNSS station.
The computed values Δv_{asc} and Δv_{desc} are added to the set of the ascending and descending PS, respectively.

Correction of the PS coordinates after residual topographic error estimation The procedure implemented in StaMPS for the computation of the topographic error relies on the computation of the phase error from uncertainty in the DEM as proportional to the perpendicular component of the baseline ($B_\perp$) (Hooper 2006). Referring to the i-th interferogram and the x-th resolution cell

$$\phi_{res,topo} = B_{\perp,x,i} K_{\epsilon,x} \tag{1.20}$$

where $K_{\epsilon,x}$ is a proportionality constant and it can be estimated for each pixel in a least square sense from the set of the available interferograms. The topographic error in meters (ΔH of Figure 1.5) is then computed exploiting orbital and image geometric parameters. Then, the correction along the ground range and its components along the North and East directions can be computed according to Equations (1.15) and (1.16). Finally, the corrected geographical coordinates ($\text{Lat}_{\text{corrected}}$ and $\text{Lon}_{\text{corrected}}$) of the PS can be computed as

[4]Link to the manual: `http://davidbekaert.com/download/TRAIN_manual.pdf`

$$\text{Lat}_{\text{corrected}} = \text{Lat} + \Delta\text{Lat} = \text{Lat} + \frac{\Delta N}{\rho} \tag{1.21}$$

and

$$\text{Lon}_{\text{corrected}} = \text{Lon} + \Delta\text{Lon} = \text{Lon} + \frac{\Delta E}{r} \tag{1.22}$$

for the Latitude and Longitude, respectively.
In Equations (1.21) and (1.22), ρ is the first radius of curvature and holds

$$\rho = \frac{a(1-e^2)}{(1-e^2\sin^2\phi)^{3/2}} \tag{1.23}$$

and r is the radius of curvature of the parallel and is equal to

$$\rho = N\cos\phi \tag{1.24}$$

in which N is the grand normal and is expressed as

$$N = \frac{a}{(1-e^2\sin^2\phi)^{1/2}} \tag{1.25}$$

In Equations (1.23) and (1.25), a and e are the semi major axis and the eccentricity of the WGS84 ellipsoid respectively and ϕ is the mean Latitude of the scene.

Decomposition As far as the the decomposition algorithm is concerned, the first step is the creation of a single grid that contains both the ascending and descending sets of PS data defined in a geographic ellipsoidal coordinate system. For this purpose, a four-element vector containing the grid limits ($\mathbf{lim} = [a, b, c, d]$) is created, where a (b) is the minimum between the minimum longitude (latitude) of the ascending set of PSs and the minimum longitude (latitude) of the descending set of PSs, c (d) is the maximum between the maximum longitude (latitude) of the ascending set of PSs and the maximum longitude (latitude) of the descending set of PSs. The number of grid cells along both the directions can be computed as

$$N_{cells} = \frac{l_{max} - l_{min}}{\delta}$$

in which l_{max} and l_{min} indicate the maximum and minimum longitude (latitude), respectively and δ is the step size of the cells in degrees. The extension of the cells can be derived dividing the extension of the grid (both along longitude and latitude) by the number of cells. A simplified graphical description of the decomposition grid creation is presented in Figure 1.7.

The second step of the decomposition consists of checking for each cell if PSs from ascending and descending set are present. For each non-empty cell, the mean of the mean PS velocity for each orbit is assigned to the cell centroid allowing the decomposition of velocities exploiting Equation (1.19). In the described procedure, the local incidence angle for each PS is considered.

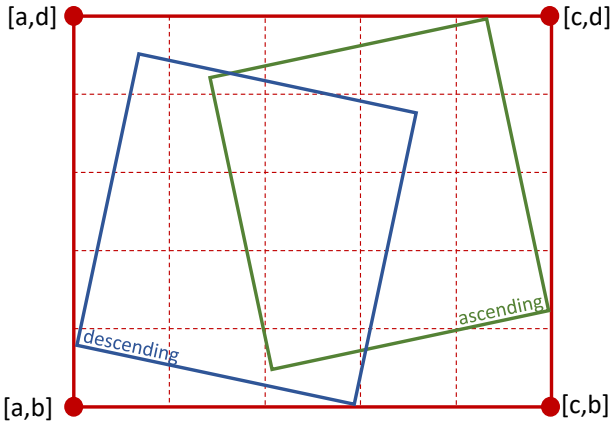

Figure 1.7: A simplified graphical description of the decomposition grid creation.

1.3.5 Medium and high resolution SAR data

The workflow presented in Section 1.3 and shown in Figure 1.3 has a general validity and minor changes have to be performed to tailor it to the processed data. In particular, during my PhD activities medium resolution data from the Sentinel-1 constellation and high resolution data from COSMO-SkyMed satellites were processed.

Sentinel-1 data Sentinel-1 satellites are part of the ESA EO Copernicus program, whose aim is to provide services and near-real-time and easily accessible data with a global coverage for a number of applications such as the management of natural disasters, the monitoring of oceans, vegetation and atmosphere, the climate change studies, the sustainable development and the civil protection (Geudtner et al. 2014). The free, full and open access to Sentinel data is guaranteed for all the users through the *Copernicus Open Access Hub*[5]. The Sentinel-1 constellation is currently composed of Sentinel-1A and 1B satellites, launched respectively in April 2014 and April 2016, both equipped with a C-band SAR instrument. Unfortunately, due to an anomaly occurred in December 2021, the end of the S1B was announced; however, the Sentinel satellites 1C and 1D are under development and the launch of Sentinel-1C is expected to occur in the second quarter of 2023. Regarding the orbital parameters, Sentinel-1 satellites have a circular near-polar Sun-synchronous orbit at an altitude of 693 km with a revisiting time of 12 days for each satellites and a 6 days revisiting time for the constellation. With the described space segment and an extensive ground segment, S1 constellation is able to provide routine data within one hour to ground station, 24 hours to the archive and emergency request data in near-real time.
The acquisition modes implemented on-board the S1 satellites are listed and described in the following:

- Interferometric wide swath (IW). The IW mode implements the Terrain Observation with Progressive Scan (TOPS) SAR mode, an improvement of the ScanSAR mode in terms of image performance, that is the most suitable in case of large scale monitoring applications (Torres et al. 2012; Yagüe-Martínez et al. 2016; De Zan and Monti Guarnieri 2006). The basic idea of the TOPS acquisition mode is that the sensor scans the illuminated area at the ground rotating the antenna both from backward to forward in the azimuth direction and along bursts in the range direction.

[5]Link to the data hub: `https://scihub.copernicus.eu/dhus/#/home$`

However, the fast azimuth beam steering reduces the target dwell time, and as such, the spatial resolution in azimuth. The main advantage of the TOPS mode is related to the capability of providing wide swaths; in particular, the IW TOPS mode implemented on Sentinel-1 satellite provides 250 km-wide swaths in range direction. The achieved spatial resolution of the IW Single Look Complex (SLC) TOPS data is 5 m$\times$ 20 m in range and azimuth respectively, with an incidence angle values that range from 32.9° for the first subswath (IW1) to 43.1° for the last subswath (IW3).

- Stripmap (SM). In SM mode, uninterrupted coverage is provided, with a spatial resolution of 5 m $\times$ 5 m at a swath width of 80 km. For each swath the antenna is configured to generate a beam with fixed azimuth and elevation pointing. Elevation beam forming is applied to suppress range ambiguity. Stripmap mode will only be operated on request for extraordinary situations.

- Wave (WV). In the WV mode, a single Stripmap image is acquired with an alternating elevation beam at a fixed on/off duty cycle, resulting in the generation of 20 km $\times$ 20 km vignettes at regular intervals of 100 km with a spatial resolution of 5 m $\times$ 20 m. The incidence angle could vary in the range $[23 - 37]^\circ$.

- Extra Wide Swath (EW). As the IW mode, EW mode implements the TOPS technique to cover a very wide area of 400 km at a spatial resolution of 20 m $\times$ 40 m (range $\times$ azimuth). The incidence angle can assume values in the range $[18.9 - 47]^\circ$

The IW, SM and EW mode support single and dual polarisation, while WV mode data are available in single polarisation only.

The IW SLC S1 data are those of interest in this thesis. An extensive description of the IW SLC TOPS data can be found in Yagüe-Martínez et al. (2016). In particular, SLC consists of focused, georeferenced, zero-Doppler and slant oriented data. These are Level-1 processing data, obtained from raw data after a pre-processing step, the Doppler centroid estimation and the focusing.

With reference to Figure 1.8, the processing of the S1 data is performed at bursts level in the first processing steps, therefore the selection of the same swaths and bursts for the master and slave images is required. The orbital corrections need to be applied exploiting the precise orbit information and the coregistration of the SAR images is performed taking advantage of an external DEM of suitable accuracy and spatial resolution. Adjacent bursts in azimuth direction are merged (i.e. deburst step of Figure 1.8) and the interferograms are computed from the stack of coregistered and debursted pairs of images. Finally, the topographic phase contribution is computed from the DEM and removed from the interferograms. The stack of coregistered products and the stack of interferograms without the topographic contribution are exported for successive PS processing.

COSMO-SkyMed data The COnstellation of small Satellites for Mediterranean basin Observation (COSMO-SkyMed) mission is the main EO mission of the Italian Space Agency (ASI) and it aims at providing data and services for a variety of both Civilian and Defence use such as emergency, risk management, scientific and commercial applications offering a global coverage and all weather and day and night acquisition capability of high spatial resolution and short revisiting time SAR data. The system is composed of: a) a first (CSK) and a second (CSG) generation of satellites equipped with a multi-mode

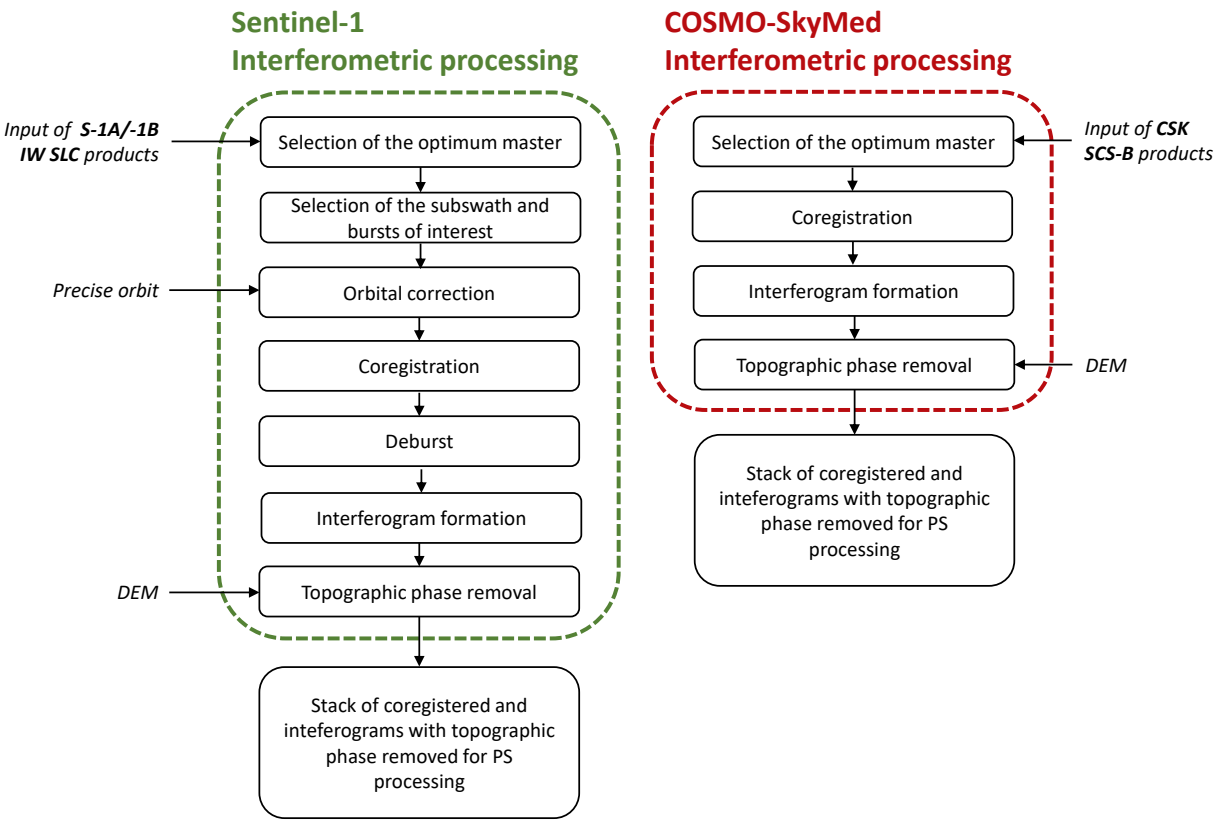

Figure 1.8: The Sentinel-1 (left) and COSMO-SkyMed (right) interferometric processing workflow.

X-band SAR instrument and antenna, b) ground infrastructures for the management of the system, the collection, archiving and distribution of the acquired SAR data. Focusing on the space segment, the first generation mission consists of four satellites whose launches took place in 2007, 2009 and 2010 with the completion of the deployment, and thus the provision of the data, in January 2011. The second generation mission is based on two enhanced satellites placed on the same orbit of the CSK satellites whose aim is to provide continuity to the first generation mission improving the performances of both space and ground segment.
The available acquisition modes are:

- SPOTLIGHT. In the Spotlight mode, the antenna is steered during the acquisition both in azimuth and elevation illuminating for a long time period the scene, thus increasing the synthetic aperture antenna length and the azimuth resolution at the expense of the azimuth coverage. In fact, the Spotlight images have a spatial resolution of 1 m in both range and azimuth for the first generation of satellites and sub-metric spatial resolution for CSG satellites and a scene size of 10 km $\times$ 10 km. Single polarization acquisitions are available for CSK data, while, for CSG satellites, also dual polarization is available.

- STRIPMAP. The Stripmap acquisition mode is implemented by pointing the antenna along a fixed direction with respect to the flight path, thus the antenna footprint is a strip on the ground surface and the acquisition could be virtually non-limited along the azimuth. However, the length of the strip is limited due to the limitations related to the SAR duty cycle. For the first generation, HIMAGE and PINGPONG modes are available with a scene size of 40 km $\times$ 40 km and 30 km $\times$ 30 km, respectively,

with single polarisation, whereas dual and quad polarisation data are available with CSG acquisitions.

- SCANSAR. In the Scansar mode, the antenna beam is periodically stepped to neighbouring sub-swath allowing wider swath in range (from 100 m to 200 m) at the expenses of the spatial resolutions (from 30 m and 100 m resolution of CSK to slightly increased values of CSG). With the second generation, also the polarimetric capabilities are improved with the availability of dual polarization.

For the second generation mission, non-standard Spotlight operation modes are available: the Discrete Stepped Strip Multi-Swath and the Theatre. The former mode makes available the simultaneous acquisitions of two separate targets based on the interleaved transmission with a halved Pulse Repetition Interval with respect to a standard acquisition and thus a reduced swath width in range. The images from the Discrete Stepped Strip Multi-Swath mode have a scene size of 10 km $\times$ 4 km and a spatial resolution of 0.6 m in both the directions. In the case of Spotlight Theatre mode, a pitch manoeuvre is performed to acquire a series of adjacent (along both range and azimuth) or scattered images on an area of interest at the expenses of the image quality. The acquisition and distribution of images from the non-standard modes are subjected to a specific authorization.
Regading the orbital position of the satellites, the CSK and CSG satellites share the same orbital plane. CSK satellites are positioned to guarantee at least two acquisitions per day over the same area under different geometry with a distance of 90° between the first three satellites and 67.5° between the second and fourth satellites allowing a one-day revisit time in the Tandem-like configuration. The two CSG satellites are positioned 180° apart to guarantee interferometric acquisitions every 8 days. Moreover, with the Stripmap mode, interferometric acquisitions between first and second generation satellites are provided.

The Single Look Complex Slant (SCS) CSK data are obtained after the level 1A (L1A) processing and consist of focused complex data in slant range and zero Doppler projection. SCS L1A data are available as unbalanced (SCS_U) and balanced (SCS_B); the latter, that will be of interest for this thesis, contain in-phase and quadrature components and are obtained after weighted processing with cosine-like windowing and radiometric equalization in addition to compensation, internal calibration and data focussing. Regarding the acquisition mode, the Stripmap HIMAGE is the one selected for this activity and it provides L1A SCS products with a 3 m ground resolutions and the incidence angle varying in the range $[18 - 59.8]°$.
The information reported in this Section and additional material regarding the COSMO-SkyMed missions and products can be found in ASI (2019, 2021).

The developed workflow for the processing of CSK Stripmap HIMAGE L1A SCS_B data (right part of Figure 1.8) consists of the selection of the optimum master following the criteria presented in Section 1.3.1, the coregistration of the products with respect to the selected master, the computation of the stack of interferograms and the subtraction of the topographic contribution exploiting an external DEM. Finally, the stack of coregistered and the stack of interferograms without the topographic contribution are exported for the PS processing.

1.4 Final remarks

In the first Section of this Chapter, the Synthetic Aperture Radar Interferometry basics needed for the comprehension of this thesis have been briefly reported. Then, the developed processing strategy for dual orbit set of satellite SAR data has been presented. It relies on the interferometric processing performed in SNAP and the PSI processing along with the atmospheric phase correction carried out in StaMPS and TRAIN, respectively. The procedure has been completed with the calibration, decomposition and correction of the PS coordinates accounting for the residual topographic error; the implementation details regarding the added procedures have been given in Section 1.3.4. Finally, the changes made to the general workflow for the processing of medium resolution Sentinel-1 and high resolution COSMO-SkyMed data have been presented along with the essential information regarding the SAR constellation, the geometries of acquisitions and the data provided by these constellations.
The combined use of the open source and free SNAP, StaMPS and TRAIN processing tools offers great opportunities for users interested in a trusted interferometric processing of SAR data from the more recent constellations. Moreover, the open code of the StaMPS package provide to the users the opportunity to make changes and adjust the available processing strategy, to develop the specific processing needed for the application of interest and to complete it, as done during my PhD research activity, with the calibration and decomposition steps and the corrections of the PS coordinates due to the DEM error.
In this dissertation, SAR data from the Sentinel-1 and COSMO-SkyMed satellites have been mentioned and the processing of set of data from these constellations will be presented and discussed in the following Chapter. On one hand, the great availability of Sentinel-1 data along with the provided spatial and temporal resolutions make these data particularly suited for the large and medium scale monitoring of the phenomena occurring at the ground with different spatial and temporal evolutions. On the other hand, COSMO-SkyMed data, thanks to the available high resolutions and the high frequency of the mounted radars, offer new opportunities for structural and infrastructural investigations, for which a high number of scatterers and the capability to detect very small displacements are required.

Chapter 2

PSI-based ground deformation with uncertainty estimation and validation

In this Chapter, a procedure to estimate the uncertainty level associated to the PSI-based East-West and vertical velocities is proposed along with the validation performed with velocities computed from GNSS observations. Finally, an application of the processing strategy proposed in Chapter 1 and the procedures presented in this Chapter is proposed. In particular, the processing of a dual-orbit S1 dataset over the eastern sector of the Po Plain and subsequent analyses are presented.

2.1 Introduction

Satellite radar interferometry is recognized as an effective technique in different applications focused on deformation phenomena that occur on the Earth surface. The successful application of this methodology is strictly related to the ability to depict the displacement of ground targets at a very high level of accuracy ($1 - 2$ mm/yr) using SAR images and time series analysis of displacements oriented along the LOS directions. Since the first applications in the early 1990s, with the first generation of SAR satellites (ERS-1 and Radarsat-1), the temporal and spatial resolution increased and a number of research fields have taken advantage of satellite radar interferometry, such as applications to natural hazard assessment, ground deformation, investigations into polar cap dynamics, slope failures, and instability processes in general (Gabriel et al. 1989; Massonnet et al. 1993, 1995; Massonnet and Feigl 1998; Bürgmann et al. 2000; Moreira et al. 2013; Rucci et al. 2012). A number of SAR images provided by ended (e.g., ERS-1 and -2, Envisat, Radarsat 1, ALOS PALSAR) and active (e.g., Radarsat 2, TerraSAR-X, ALOS-2, COSMO SkyMed) satellite radar missions have been used for the above mentioned applications with some remarkable results obtained. In the last years, under the Copernicus Earth Observation programme, the Sentinel-1A and Sentinel-1B satellites equipped with radar sensors were launched starting to provide worldwide free-access SAR images at average spatial resolution and with very short revisiting times, which opened new perspectives for continuous ground-surface monitoring (Geudtner et al. 2014). The time series of the S1 SAR images is now long enough to process reliable displacement maps with more reliable detection of seasonal and/or long-term trends and to make the validation procedure, based on comparisons with

external data, more reliable.
To obtain the final velocity field in a geodetic reference frame, displacements along the vertical and horizontal directions are required and a vector decomposition analysis must be applied. However, during the decomposition from ascending and descending slant velocities to different directions the uncertainties propagate. See Ogundare (2015) for details about the application of the error propagation law to geodesic and surveying science. However, the studies focused on ground deformations phenomena from the processing of single or dual orbit S1 SAR image depicting ground deformation maps of large areas (Devanthéry et al. 2018; Cian et al. 2019; Delgado Blasco et al. 2019; Manunta et al. 2019; Roccheggiani et al. 2019) often lack of further decomposition analysis and a validation procedure complemented by uncertainty analysis. Manunta et al. (2019) used accurate continuous global navigation satellite system (CGNSS) positions to refer the displacements for the whole Italian territory to a global reference frame, as obtained from descending S1 data and the SBAS method. Delgado Blasco et al. (2019) developed a workflow based on the SNAP and StaMPS tools to process dual-orbit S1 data with successive vector decomposition, to obtain the actual vertical motion component. They used the velocities available from CGNSS sites as reference, with no further validation steps. To date, the scientific literature does not provide evidence on the accuracy assessment of ground deformation maps based on dual-orbit S1 data and the SNAP–StaMPS workflow with respect to a defined global reference frame. However, a similar approach was described by Del Soldato et al. (2018) and Farolfi et al. (2019b).
In this Chapter, a procedure for the accuracy assessment of the PSI velocities and the validation at specific sites based on an error propagation analysis is proposed. The strategies adopted in the processing of S1 dual-orbit data using the SNAP and PSI–StaMPS open-source routines with constraint of single orbit products to a global reference frame and decomposition analysis have been described in Chapter 1. To align PSI slant velocities to a reference frame and validate results on selected sites, we processed GNSS observation from continuous stations distributed over the study area. In particular, we discuss the performances of the SNAP–StaMPS workflow for the investigation of ground deformation over metropolitan areas located in the southeastern border of the Po Plain (Italy). This represents a unique case study where significant ground deformation phenomena have been reported over a large area due to the combination of natural (e.g., quaternary sediment compaction of the Plio-Quaternary deposits and deep tectonics) and anthropogenic (e.g., mainly pumping of groundwater for industrial and drinking purposes or deep gas field exploitation) factors (Teatini et al. 2006; Modoni et al. 2013). Subsidence phenomena have been previously investigated through analyses based on PSI from data provided by both single and dual ERS and Envisat satellite orbits (Farolfi et al. 2019b; Stramondo et al. 2007; Bitelli et al. 2015). However, no updates have been provided using data from dual orbits modern satellite radar sensors and CGNSS data. To cover this gap, we processed the full range of the available ascending and descending S1 data, along with the observations provided by the CGNSS permanent stations installed in the area. We retrieved the vertical and East-West oriented velocity fields after vector decomposition and validate results following the above discussed approach. We obtained a ground deformation map which updates the present knowledge about phenomena occurring in the investigated area and discussed a few case studies where vertical and horizontal displacements can be linked to different factors.

2.2 Uncertainty estimation and SAR validation

In this Section, a method for the accuracy assessment of calibrated PSI products from dual-orbit dataset is proposed along with the validation of the ground deformation maps performed with respect to a defined global reference frame. To this aim, velocities from CGNSS observations will be employed.

Uncertainty analysis From Equation (1.14), given the uncertainties affecting the North, East and vertical GNSS velocity components ($\sigma^2_{v_\mathrm{n}}$, $\sigma^2_{v_\mathrm{e}}$ and $\sigma^2_{v_\mathrm{up}}$, respectively), the uncertainties of the LOS-oriented GNSS velocities for both orbits can be computed following the uncertainty propagation law as

$$\sigma^2_{v^{\mathrm{GNSS}}_{\mathrm{LOS}}} = \left[\frac{\partial f}{\partial v_\mathrm{up}}\right]^2 \cdot \sigma^2_{v_\mathrm{up}} + \left[\frac{\partial f}{\partial v_\mathrm{n}}\right]^2 \cdot \sigma^2_{v_\mathrm{n}} + \left[\frac{\partial f}{\partial v_\mathrm{e}}\right]^2 \cdot \sigma^2_{v_\mathrm{e}} + C \tag{2.1}$$

Where f is the function expressed by Equation (1.14) and C denotes the covariances related to the pair of the variables. Under the hypothesis that the variables are not correlated and the angles are error-free, the uncertainties of the LOS-oriented GNSS velocities can be expressed as

$$\sigma^2_{v^{\mathrm{GNSS}}_{\mathrm{LOS}}} = \cos^2(\theta_\mathrm{inc})\sigma^2_{v_\mathrm{up}} + \sin^2(\theta_\mathrm{inc})[\sin^2(\alpha)\sigma^2_{v_\mathrm{n}} + \cos^2(\alpha)\sigma^2_{v_\mathrm{e}}] \tag{2.2}$$

in which θ_inc is the local incidence angle and α is the orbit heading angle.
The computation of Equation (2.2) can be performed for both the ascending and descending orbit, thus obtaining the uncertainties related to the LOS components of the GNSS velocities, namely $\sigma^2_{v^{\mathrm{GNSS}}_{\mathrm{LOS,asc}}}$ and $\sigma^2_{v^{\mathrm{GNSS}}_{\mathrm{LOS,desc}}}$.
As far as the PS velocities are concerned, the variance–covariance matrix of decomposed velocities can be then computed from Equation (1.19) following the error propagation law

$$C_{V_\mathrm{decomp}} = \begin{bmatrix} \sigma^2_{v_\mathrm{up,PS}} & \mathrm{Cov}(v_\mathrm{up,PS}, v_\mathrm{e,PS}) \\ \mathrm{Cov}(v_\mathrm{up,PS}, v_\mathrm{e,PS}) & \sigma^2_{v_\mathrm{e,PS}} \end{bmatrix} = A^{-1} C_{V_\mathrm{LOS}} (A^{-1})^T \tag{2.3}$$

where, C_{V_LOS} is the variance-covariance matrix associated to the vector of the ascending and descending PS LOS velocities and, under the assumption that the ascending and descending LOS velocities are uncorrelated, it is expressed as

$$C_{V_{LOS}} = \begin{bmatrix} \sigma^2_{v_\mathrm{LOS,asc}} & 0 \\ 0 & \sigma^2_{v_\mathrm{LOS,desc}} \end{bmatrix}$$

In the definition of $C_{V_{LOS}}$, $\sigma^2_{v_\mathrm{LOS,asc}}$ and $\sigma^2_{v_\mathrm{LOS,desc}}$ are computed as the variance of the PS mean LOS velocities for the ascending and descending orbit, respectively. In particular, for a given validation point (e.g. a GNSS station for which the mean velocities are known), an area of interest (or validation area) is set and the variance of the mean PS velocities values is computed as

$$\sigma^2_{v_\mathrm{LOS}} = \sum_{i=1}^{N} \frac{(v_{\mathrm{PS},n} - \overline{v}_\mathrm{PS})^2}{n(n-1)} \tag{2.4}$$

where N is the total number of PS included in the validation area and $\overline{v}_\mathrm{PS}$ is the mean velocities of the PSs belonging to the same area.
The computation expressed by Equation (2.4) is performed for both the orbits obtaining

the quantities $\sigma^2_{v_{\mathrm{LOS,asc}}}$ and $\sigma^2_{v_{\mathrm{LOS,desc}}}$ referred to the set of PSs belonging to the defined validation area.
It is important to recall that Equation (2.3) allows the computation of the uncertainty level to be assigned at velocities components along the East-West and vertical directions (i.e., $\sigma^2_{v_{\mathrm{up,PS}}}$ and $\sigma^2_{v_{\mathrm{e,PS}}}$) as computed from Equation 1.19.

Validation For each validation point, the difference between the vertical and East-oriented velocities from SAR products and GNSS observations with the associated uncertainties are computed as

$$\begin{aligned}(v_{\mathrm{up,GNSS}} - v_{\mathrm{up,PS}}) \pm \sqrt{\sigma^2_{v_{\mathrm{up,GNSS}}} + \sigma^2_{v_{\mathrm{up,PS}}}} \\ (v_{\mathrm{e,GNSS}} - v_{\mathrm{e,PS}}) \pm \sqrt{\sigma^2_{v_{\mathrm{e,GNSS}}} + \sigma^2_{v_{\mathrm{e,PS}}}}\end{aligned} \tag{2.5}$$

in which v_{GNSS} and $\sigma^2_{v_{\mathrm{GNSS}}}$ are computed from the analysis of the GNSS observations (more information regarding the GNSS observations processing strategy will be given in Section 2.3.2), v_{PS} is given by Equation (1.19) and $\sigma^2_{v_{\mathrm{PS}}}$ are the elements of the main diagonal of $C_{V_{\mathrm{decomp}}}$ (Equation (2.3)).

2.3 PSI-based ground deformation investigation over the eastern sector of the Po Plain (Italy)

The general method described in Chapter 1.3 and the method described in Section 2.2 were tested through the processing of the ascending and descending S1A and S1B IW SLC products over the eastern sector of the Po Plain (Italy) to investigate the ground deformation phenomena affecting the area. In this Section, first the study area will be briefly described enlightening the geological and hydrological context and presenting the anthropogenic and natural processes that can contribute to the ground deformation phenomena. Then, the processed data and the processing strategy will be discussed with particular emphasis on the GNSS observations processing. Finally, the achieved results will be shown and discussed.

2.3.1 Study area

The selected study area is included in the eastern sector of the alluvial Po plain (Figure 2.1) and it is characterised by the historical and present ground subsidence due to a combination of long-term geological and anthropogenic related processes. The former is related to the compaction of the Holocene sediments of the alluvial plain and, in minor part, to deep active tectonics. The latter (i.e., the human-induced contribution) is connected to the extraction of groundwater from a well-developed multi-aquifer system that started during the second half of the 20th century, in parallel with the increasing industrial activities (Martinelli et al. 1998; Carminati and Martinelli 2002). Another anthropogenic minor contribution has come from the extensive agricultural and zootechnical techniques and from gas exploitation (Tosi et al. 2013), although the deformation extents due to the latter are strongly limited to productive sites.
As reported by Carminati et al. (2003b), the modern rate of subsidence is at least an order of magnitude greater than the historical rate. The major cities included within the study area are Bologna and Ferrara, settled on areas that are characterised by very different geological settings and superficial deformation processes (Carminati et al. 2003b).

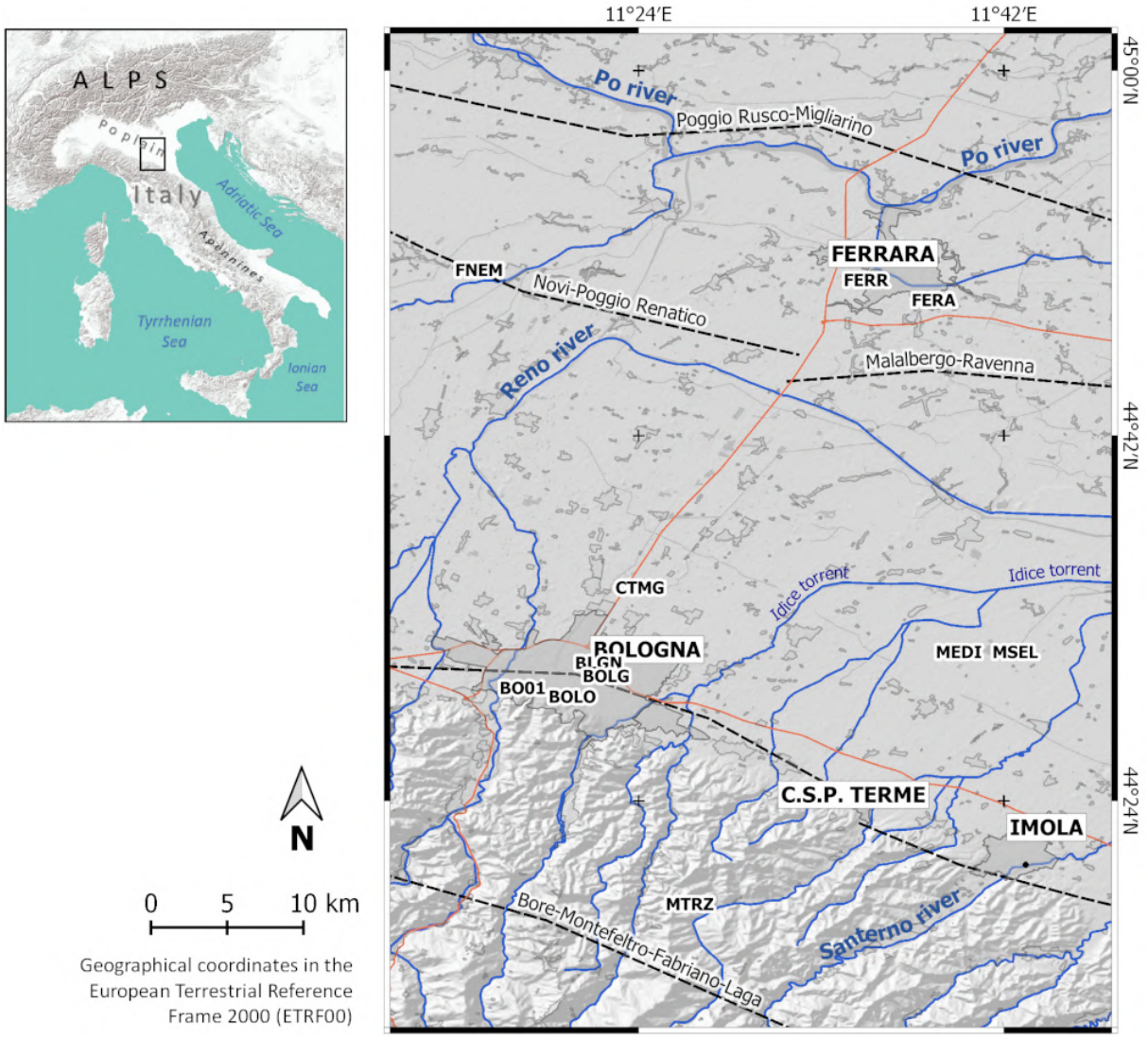

Figure 2.1: Map of the study area, including the main urbanized areas, the seismogenic faults (dashed lines, SHARE project (Basilic et al. 2013)) and the CGNSS sites used for calibration and validation purposes. The four-letter alphanumeric codes identifying the CGNSS stations are printed above the actual locations of the stations.

2.3.2 Dataset and processing strategy

For the investigation of the ground deformation phenomena, a dual-orbit set of S1 IW SLC data with a ground resolution of 20 m × 5 m (azimuth × range) were processed following the strategy described in Section 1.3; in particular the DEM from the Shuttle Radar Topography Mission (SRTM) with a resolution of 90 m has been employed to remove the topographic contribution. The selection of the candidate PS pixels was performed assuming an amplitude dispersion threshold (according to Equation 1.10) of 0.4. The linear phase-based model implemented in TRAIN was adopted to estimate and subtract the atmospheric phase contribution. Moreover, 11 CGNSS stations observations, acquired between March 2015 and the end of 2019, were processed for calibration and validation purposes.
More information regarding the SAR processed dataset are reported in Table 2.1 and the temporal and perpendicular baselines between the master and the slave images are shown in Figure 2.2. Regarding the GNSS dataset, the locations of CGNSS station are reported

Table 2.1: The Sentinel-1 dataset over the eastern sector of the Po Plain.

Orbit	Track	Number of images	Master date	Start date	End date	Subswath	θ
Ascending	117	171	3/10/2017	30/03/2015	17/09/2019	IW2	38.3°
Descending	95	132	16/05/2017	15/04/2015	12/05/2019	IW1	32.9°

Note: θ is the mean incidence angle of the scene.

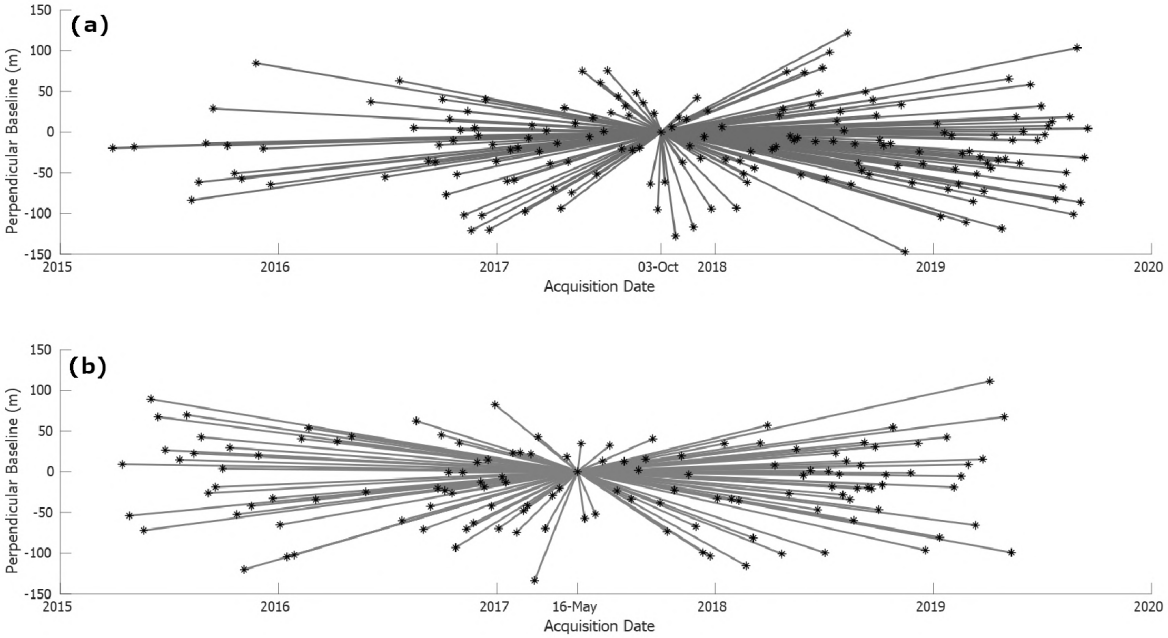

Figure 2.2: The temporal and perpendicular baselines for the ascending and descending Sentinel-1 datasets.

in Figure 2.1 while the processing strategy is described in the next paragraph.

GNSS processing strategy The absolute reference frame for the relative PSI displacement and the data for validation have been defined by a network of CGNSS sites that are unevenly distributed within the study area as shown in Figure 2.1. Moreover, CGNSS time series can improve the understanding of the superficial kinematic phenomena providing fundamental information about the tectonic and geodynamic behaviors of the region. Unfortunately, CGNSS sites belonging to international networks are usually a limited number and stations from other positioning services (e.g., managed by different public and private agencies for scientific investigations or for real-time positioning) could be of interest in the validation process. However, CGNSS sites designed and realized for technical operations do not introduce noise into the data recorded with respect to sites used for scientific applications (Baldi et al. 2009, 2011) and, for this reason, they can be taken into account.
The processing of CGNSS observations, performed using the GAMIT-GLOBK software package (Herring et al. 2018), was carried out only for the sites that meet the following criteria: a) time series of observation longer than 2.5 years, b) an efficiency (i.e., number of days with regular observations with respect to the whole period of observation) greater than the 50%. Moreover, a loose constraint approach (i.e., 100 m) applied to the a-priori coordinate of each site and tight constraints were used for the precise ephemerides and

the Earth Orientation Parameters. The FES2004 ocean-loading model (Lyard et al. 2006) and an atmospheric propagation delay based on the global mapping function (Boehm et al. 2006) were used in addition to the absolute antenna phase center model provided by the International GNSS Service for satellites and ground stations. The provided daily solutions were constrained to the European Terrestrial Reference Frame (ETRF) 2014, with an Helmert transformation and a minimization procedure of the differences between the positions of the 14 International GNSS Service stations surrounding the study area (Cenni et al. 2012). The daily time series for the North, East and vertical components were modelled as

$$y_j(t_i) = D_k + v_k t_i + \sum_{k=1}^{N} d_{jk} H(t_i - T_k) + \sum_{k=1}^{M} \left(A_{1k} \cos\left(\frac{2\pi t_i}{P_k}\right) + A_{2k} \sin\left(\frac{2\pi t_i}{P_k}\right)\right) + \epsilon_k(t_i) \quad (2.6)$$

in which j is the index that represent the direction (i.e., North, East or vertical). Assuming a linear trend of displacement in the time series within the analysed time span, the initial position (D_k) and velocity (v_k) obtained from an ordinary least squares linear regression analysis were used to model the long-term trend. The N discontinuities due to instrumental changes and seismic events that occur near the sites are modelled with the d_{jk} terms, while $\epsilon_k(t_i)$ is time-dependent noise, and A_{1k} and A_{2k} are the amplitudes of the M (with $M \leq 5$) seasonal signals with period P_k. During the first phase of the analysis, only the initial position, velocity, discontinuities and noise were estimated by a weighted least-squares method. To obtain a residual time series, a model of the motion was computed using the parameters estimated and, successively, this motion was removed from the time series. Residuals were used to compute the standard errors of the linear regression analysis and, successively, analysed using a non-linear least-squares technique to estimate the spectra, following the Lomb–Scargle approach (Lomb 1976; Scargle 1982). The spectrum of each component was analysed to estimate the period of the five statistically meaningful signals in the interval between 1 month and half of the observation time span. Periodicities were therefore used in Equation (2.6) to estimate discontinuities, the intercept and velocities, with amplitude

$$A_k = \sqrt{A_{1k}^2 + A_{2k}^2} \quad (2.7)$$

and phase

$$\phi = \arctan \frac{A_{2k}}{A_{1k}} \quad (2.8)$$

for each component.

For the calibration procedure, the BOLG CGNSS station was chosen as the reference for three main criteria: the length of the time series of observations, the number of days with regular observations with respect to the whole period and the quality of the monument used in the antenna installation. In particular, BOLG is part of the Regional Reference Frame Sub-Commission for Europe (EUREF) Permanent GNSS Network and it guarantees a reliable constraint to the global reference frame.
The processing performed at the BOLG site (using Equation (2.6)) for the same observation period as the interferometric dataset gave the following results

$$v_{\text{up}}^{\text{BOLG}} = (-1 \pm 1.2)\,\text{mm/yr}$$
$$v_{\text{east}}^{\text{BOLG}} = (0.3 \pm 0.5)\,\text{mm/yr}$$
$$v_{\text{north}}^{\text{BOLG}} = (4.6 \pm 0.5)\,\text{mm/yr}$$

The residual horizontal components were estimated by removing the Eurasian plate movements modelled with the parameters provided by Altamimi et al. (2016).
The CGNSS velocities projected along the ascending and descending LOS directions with uncertainties (according to Equations (1.14) and (2.1)) are

$$v_{\text{LOS,asc}}^{\text{BOLG}} = (-1.4 \pm 0.9)\,\text{mm/yr}$$
$$v_{\text{LOS,desc}}^{\text{BOLG}} = (-1.1 \pm 1.0)\,\text{mm/yr}$$

2.3.3 Results and discussions

In this section, the results of the processing and analysis of the dataset described in Section 2.3.2 are presented along with the discussion of the obtained results.
The first result that has to be shown are the LOS-oriented and calibrated velocity maps within the study area for the ascending and descending orbits (Figure 2.3). In the legend of the maps presented in Figure 2.3, the colour red corresponds to a range increase of the targets (i.e., a movement away from the satellite) and the colour blue represent a decreasing of the distance in time between the targets and the sensor (i.e., a movement towards the satellite). The areas bordered by black rectangles and numbered represent areas in which significant ground deformation phenomena have occurred in the period of observation. The first marked area (area 1) is the metropolitan area of the city of Bologna in which a spatially broad phenomenon is highlighted by the data. The other two areas (area 2 and area 3) correspond to smaller cities (Minerbio and Budrio, respectively) in which very localised phenomena occurred, demonstrating that. in the study area, phenomena at different geographic extents have occurred in the time spanned by the analysis.

The uncertainty affecting the average velocity of radar targets located in the vicinity of BOLG station has been quantified by a statistical analysis applied to the group of selected PSI time series used. In particular, samples of more than 30 slant velocities in both orbits have been used and averaged to find the average values to be aligned with slant projected CGNSS velocities. A sample of ascending time series of the PSs located in the calibration area (i.e., in the vicinity of the BOLG GNSS reference site) is presented in Figure 2.4, in which each sub-figure (from 1 to 6) represents the time series of a PS. As can be seen from Figure 2.4, the PS displacement scattering is in a range of few millimetres between the acquisition epochs.

Even though several studies (Stramondo et al. 2007; Baldi et al. 2009, 2011; Cenni et al. 2013) pointed out that the displacement occurring in the study area is mainly related to the lowering of the ground due to anthropogenic causes, the occurrence of horizontally-oriented displacement components cannot be excluded a priori. In fact, phenomena characterized by the horizontal displacement of the same order as the vertical one have been detected in the Po Plain area from GNSS observations (Baldi et al. 2009, 2011; Cenni et al. 2012, 2013). For this reason, to achieve full knowledge of the ground deformation field as detected by the SAR acquisition geometries, there is the need for vector decomposition analysis from ascending and descending velocity maps acquired in the slant geometry complemented by

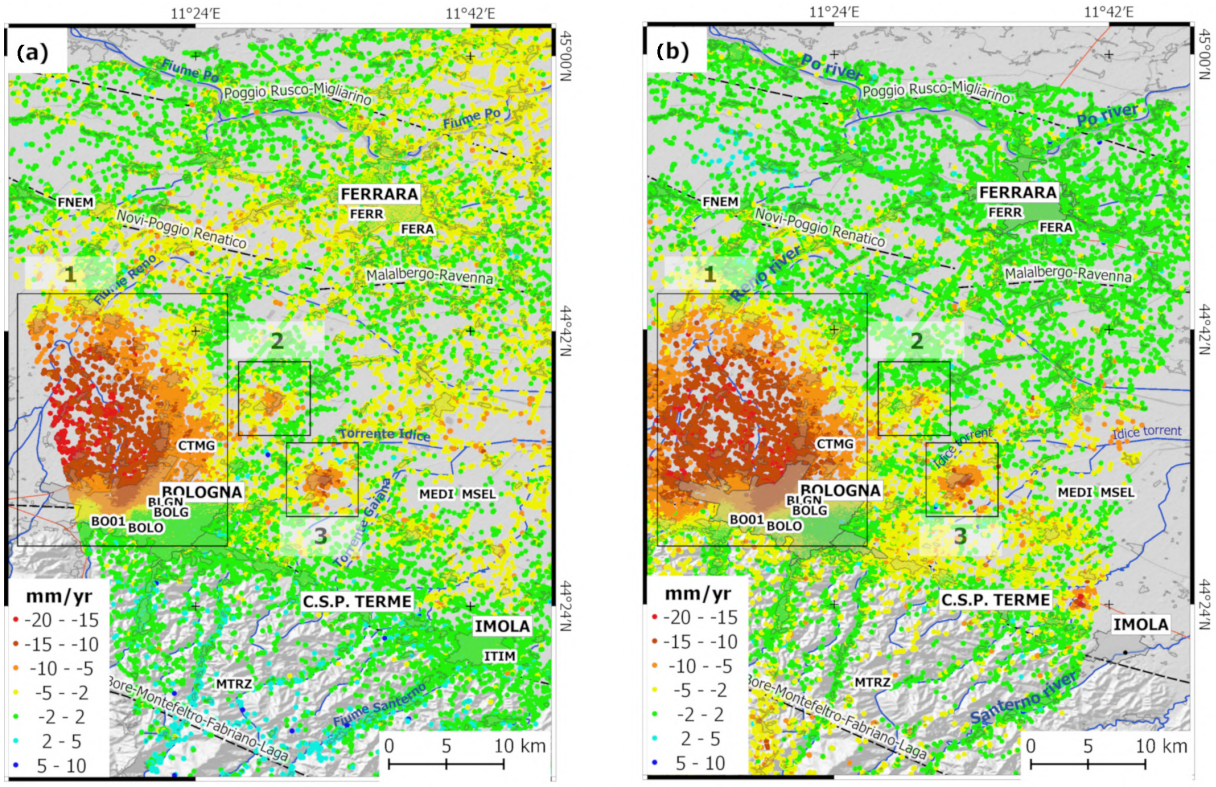

Figure 2.3: LOS-oriented and calibrated velocity maps (mm/yr) obtained from the ascending (a) and descending (b) orbits within the study area. Areas enclosed by rectangles identify zones characterized by significant deformation phenomena: (1) Bologna metropolitan area; (2) municipality of Minerbio; (3) municipality of Budrio.

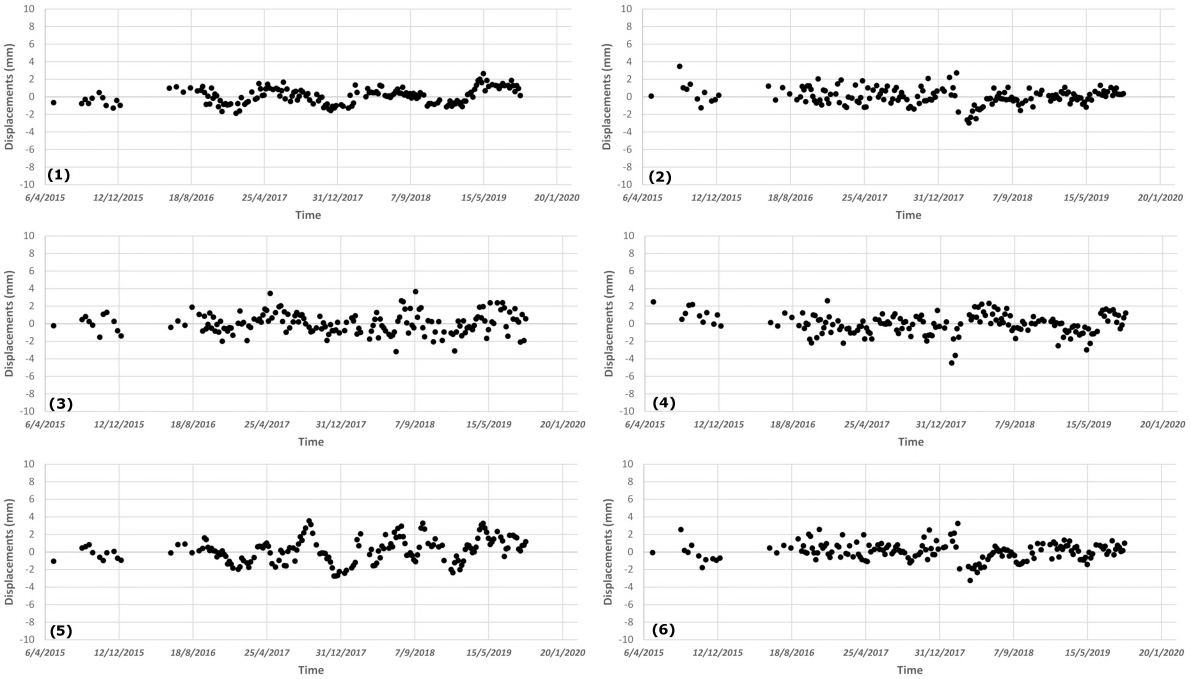

Figure 2.4: A sample of ascending slant oriented time series provided by the Persistent Scatterer Interferometry analysis in the vicinity of BOLG station. Each sub-figure (1–6) represents the time series of a single Persistent Scatterer.

the error propagation analysis performed as described in Sections 1.3.3 and 2.2. As far as the author knows, previous SAR-based studies in the study area did not perform the decomposition of displacement from ascending and descending set of SAR data.
As already seen in Section 1.3.4, the first step of the decomposition procedure aims at sampling the ascending and descending dataset over a common grid. The dimension of the grid was chosen to be comparable with the spatial resolution of S1 data; for this reason, a grid with a dimension of 20 m $\times$ 20 m at the ground is selected. Then, Equation (1.19) is used to compute the velocities along the vertical and East-West directions for cells with at least 1 Persistent Scatterer included in both orbits obtaining the vertical and horizontal velocities maps shown in Figure 2.5. For the dataset taken into account and the described processing, 111,306 non-empty cells were obtained from the decomposition procedure. The use of larger decomposition grid size would have produced a decrease of the cells number and a smoothing effect on the resulting decomposed velocities; for instance, considering a sampling grid size of 30 m $\times$ 30 m, a 10% reduction of the number of cells can be noted. From the vertical velocity map of Figure 2.5, a significant vertical deformation pattern over a wide area in the western sector of the metropolitan area of Bologna (area 1), whit vertical rates up to 20mm/yr, can be seen over an extent of approximately 200 km^2. The horizontal velocity pattern shows increasing eastern movement in the same area where the greatest subsidence velocities are seen, thus suggesting the presence of horizontal displacement components involved in the subsidence processes. Moreover, at the North-East of the study area, where the city of Ferrara is located, a widespread and eastward movement (i.e., positive values) in the range of a few mm/yr can be noted; this area was stricken by the seismic events in May–June 2012 and it is characterised by a Po plain sedimentary cover over a a buried arcuate thrust system and growth folds related to the Apennines chain (Carannante et al. 2015), the principal lineaments of which are also shown in Figure 2.5. The moderate uplift in this area (map (a) of Figure 2.5) might be connected to the tectonic movements of the buried Apennines chain, as suggested by several studies for the eastern movements (Mantovani et al. 2020). Finally, minor contributions to the eastward displacement might derive from actual displacements along the North direction, which would contribute to a lesser extent in the slant direction and in successive decomposition analysis.
The linear phase-based model adopted in the present study to estimate the atmospheric phase contribution is shown to be suitable for mapping deformation in the study area. In particular, the atmospheric corrections processed for the interferograms affected the hilly area that was part of the central Apennines. After the decomposition, this area shows null vertical deformation rates, with only delimited areas characterized by very small positive rates (southernmost sector of the map (a) of Figure 2.5). This behaviour is consistent with the theories related to the tectonics of the Apennine chain. Residual horizontal velocities in correspondence with the hilly area (map (b) of Figure 2.5) are mostly due to slope instabilities.

A close-up to the deformation phenomena occurring in the area 2 (municipality of Minerbio) and area 3 (municipality of Budrio) is presented in Figure 2.6 and 2.7 respectively, where the vertical and East-West velocity maps are presented. The vertical velocity map over the municipality of Minerbio (Figure 2.6, map (a)) exhibits subsidence rates up to 10 mm/yr; moreover, a prevalent East-West component is well depicted in map (b) over a delimited area. In this area, an industrial activity related to gas storage in depleted deposits takes place; however, there are no other evidences for this relationship and detailed study of the causes of such superficial deformation field is far from the aims of this dissertation.

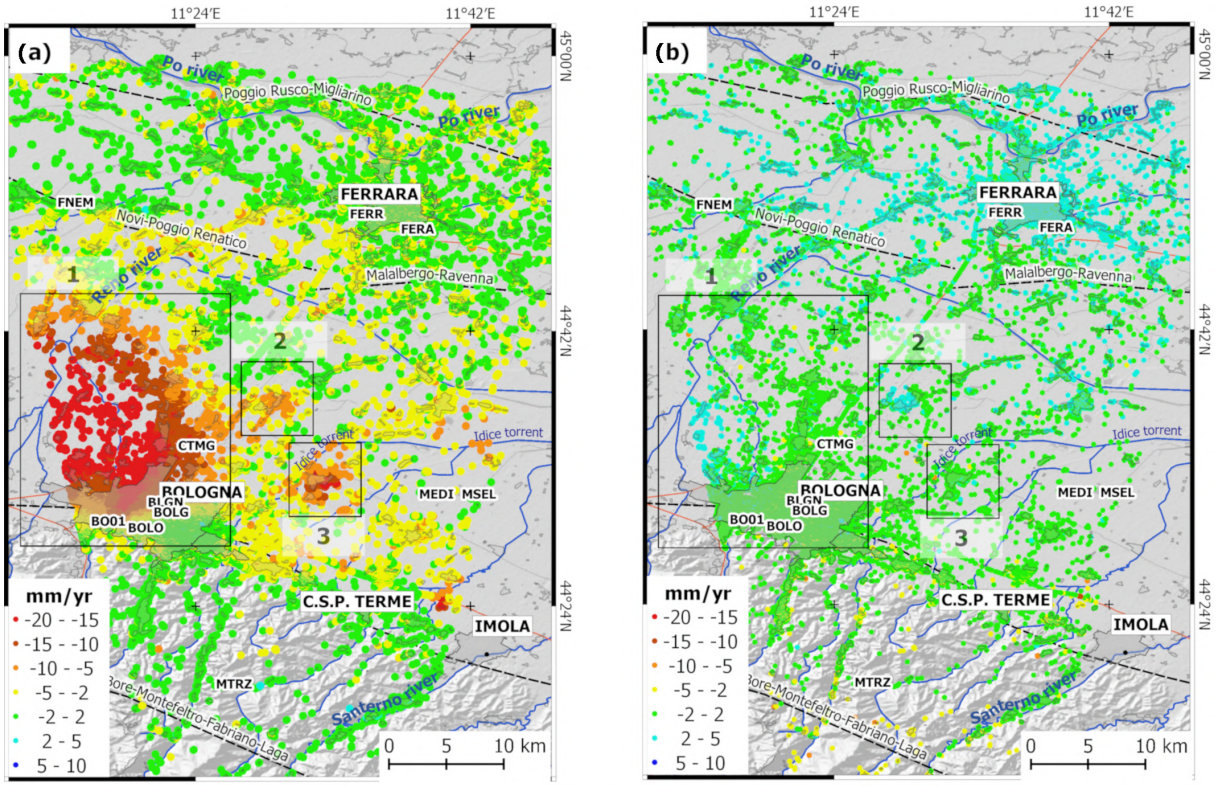

Figure 2.5: Velocity maps (mm/yr) oriented in the vertical (a) and East-West (b) directions; the decomposition grid has a size of 20 m $\times$ 20 m at the ground.

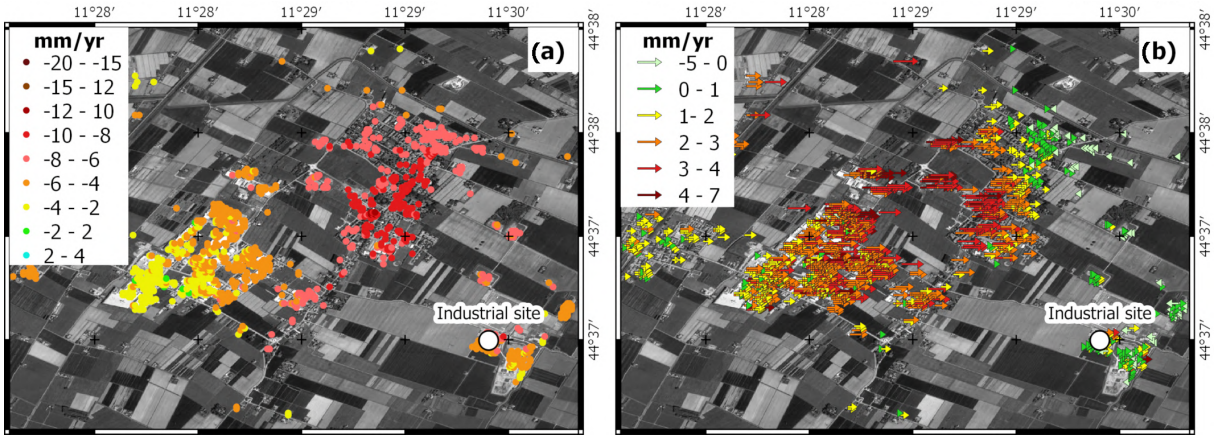

Figure 2.6: Vertical and horizontal velocity maps (mm/yr) over the municipality of Minerbio (area 2 of Figure 2.5). In the horizontal velocity map (b), negative rates indicate West-oriented horizontal displacement, positive rates indicate East-oriented horizontal displacement. Module of horizontal displacements are described using row instead of points. The white dot denotes the main site of industrial activity.

Similarly, maps (a) and (b) of Figure 2.7 show vertical and horizontal velocity maps processed in the municipalities of Budrio.

To provide quality assessment for the vertical and horizontal velocity maps after the decomposition procedure, the rates produced by the PSI-based analysis were compared with the specifically processed CGNSS measurements referred to the same period. All measurements are complemented by the uncertainty levels provided as standard deviation and, based on the procedure discussed in Section 2.2, the error propagation analysis is

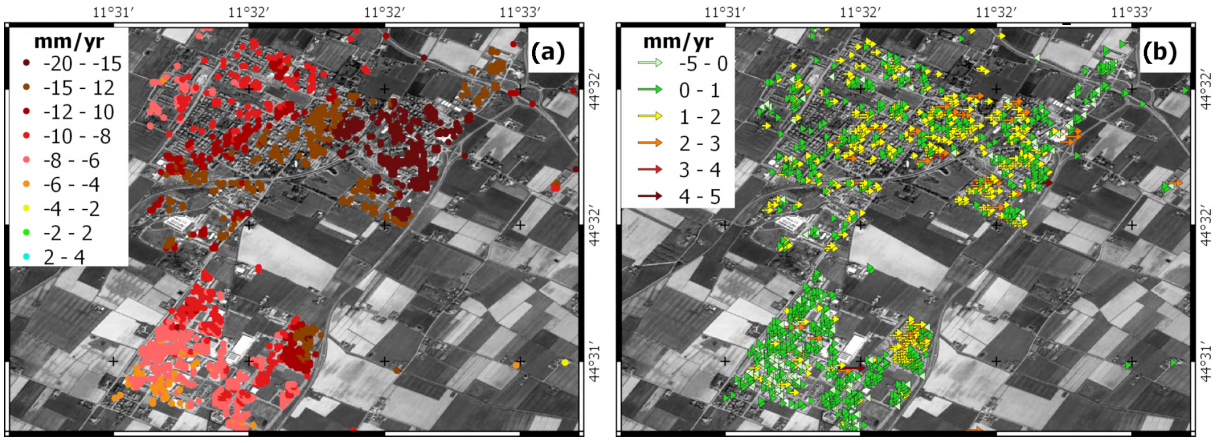

Figure 2.7: Vertical and horizontal velocity maps (mm/yr) over the municipality of Budrio (area 3 of Figure 2.5). Negative vertical rates in (a) indicate subsiding phenomena. In the horizontal velocity map (b), negative rates indicate West-oriented horizontal displacement, positive rates indicate East-oriented horizontal displacement. Module of horizontal displacements are described using row instead of points.

Table 2.2: Results of the comparisons between the velocities at the Continuous GNSS sites and the average PSI velocities for a minimum set of five PS located around the Continuous GNSS site at a given distance (SD) with: 50 m $\leqslant$ SD $\leqslant$ 500 m.

CGNSS site code	GNSS velocity (mm/yr) with standard deviation		PSI average velocity (mm/yr) with standard deviation				Comparison (mm/yr) with standard deviation	
	East	Up	East	Up	No. of PS	SD (m)	East	Up
BLGN	-1.5 ± 0.2	-7.6 ± 0.8	-1.2 ± 0.1	-8.1 ± 0.1	13	50	-0.3 ± 0.2	0.5 ± 0.8
BOLO	-0.4 ± 1	-1.9 ± 2	0.7 ± 0.1	-1.56 ± 0.1	7	50	-1.1 ± 1.0	-0.3 ± 2
BO01	0.7 ± 0.3	-4.0 ± 1.3	0.1 ± 0.1	-3.6 ± 0.1	10	100	0.6 ± 0.3	-0.4 ± 1.3
CTMG	-0.9 ± 0.8	-12.8 ± 1.6	-0.4 ± 0.1	-13.2 ± 0.1	14	100	-0.5 ± 0.8	0.4 ± 1.6
MTRZ	0.5 ± 1	-1.7 ± 1.8	-1.0 ± 0.2	-0.9 ± 0.1	2	500	1.5 ± 1.0	-0.8 ± 1.8
MEDI	1.0 ± 0.4	0.2 ± 1	0.4 ± 0.1	-1.5 ± 0.1	11	500	0.6 ± 0.4	1.7 ± 1.0
MSEL	0.6 ± 1	-1.3 ± 1.6	0.4 ± 0.1	-1.5 ± 0.1	12	500	0.2 ± 1.0	0.2 ± 1.6
FNEM	1.2 ± 0.8	-1.5 ± 2.4	1.4 ± 0.1	-1.3 ± 0.1	24	100	-0.2 ± 0.8	-0.2 ± 2.4
FERR	0.5 ± 0.7	0.1 ± 1.7	2.2 ± 0.1	-1.1 ± 0.1	9	50	-1.7 ± 0.7	1.2 ± 1.7
FERA	0.6 ± 1.1	-4.3 ± 2.1	1.9 ± 0.1	-2.2 ± 0.1	6	50	-1.3 ± 1.1	-2.1 ± 2.1

Note: Comparison is intended as (GNSS-PSI).

performed to provide errors in the final comparison between GNSS and PSI vertical and East-West velocities. The results are provided in Table 2.2. In the performed comparison, the PSI-based velocities were computed as the average values from a minimum of five persistent scatterers located in the vicinity of the GNSS site taking into account a variable radius for the validation area. To this purpose, a minimum radius of 50 m is considered; however, for each validation location, the search radius was increased by 50 m step (for a maximum of 500 m) until the required number of persistent scatterers was achieved. The final comparison is performed computing the difference between the GNSS and PSI-based velocities; results show differences smaller or equal to ± 2 mm/yr within the reference period, with larger values detected for the vertical component of the GNSS site FERA. This validation station is located in the urbanized area of Ferrara, at a distance of about 40 km from the reference site; this distance might have a role. Moreover, the levels of uncertainties are smaller than 2 mm/yr in the majority of comparisons.

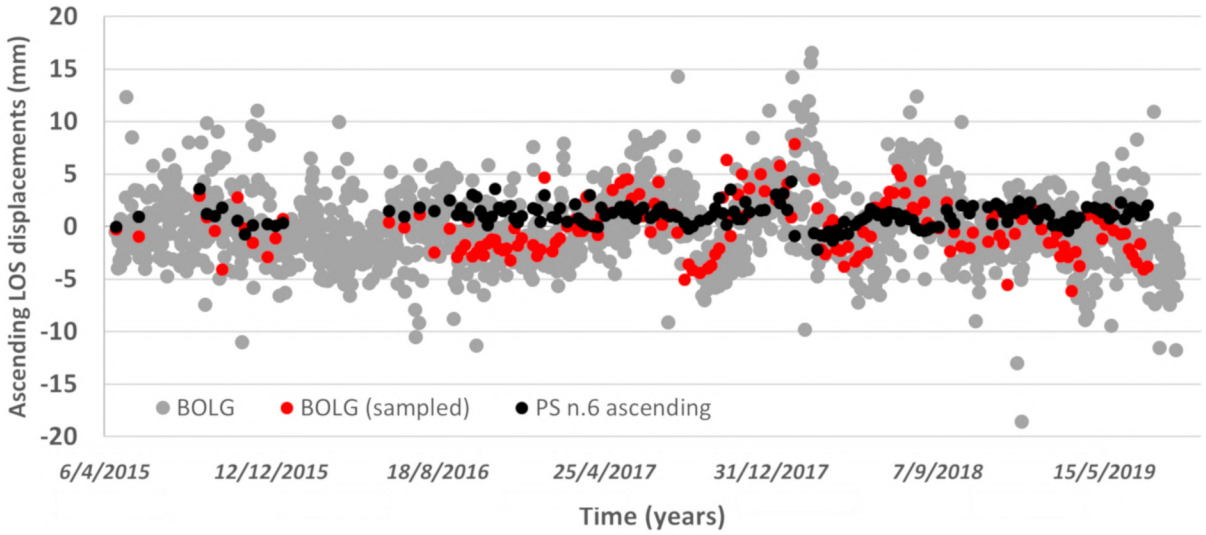

Figure 2.8: Comparison between BOLG and a single Persistent Scatterer time series. Both series are oriented along the ascending Line Of Sight and aligned with respect to a common first epoch. The time in the x axis is referred to the period under investigation and is provided in the form day/month/year.

Even thought GNSS and SAR observations velocities span the same period, a comparison of GNSS and PSI techniques based on average annual velocities could be poorly sensitive to noises and unmodelled effects. To remove part of these noises, a comparison at the level of time series of displacements should be used; to this aim, in Figure 2.8 the LOS-oriented ascending time series for a single target (the same as time series 6 of Figure 2.4) is compared with the CGNSS BOLG station positions projected along the LOS. CGNSS positions are reported for the full time series and for a subset of points sampled at the time of satellite passes. An epoch-by-epoch comparison has been assessed by the root mean square error (RMSE) and is equal to 2.9 mm for the time series presented in Figure 2.8. This is mainly due to periodic fluctuations in the CGNSS time series that are not clearly visible in the response from the radar target.

Discussions The combined SNAP–StaMPS open-source processing of full ascending and descending S1 radar data and the use of contemporary GNSS observations for the ground deformation monitoring over the eastern sector of the Po Plain have been presented. The comparison between the velocities provided by a limited number of GNSS sites and PSI analysis provided an assessment of the reliability to depict the displacement field over an area affected by subsidence phenomena. In particular, the contemporaneity of the ascending and descending SAR data and the GNSS observations used in the present study offered the opportunity to perform a careful calibration procedure with respect to a global reference frame and a decomposition analysis with successive assessment of the ground deformation phenomena. A similar approach can be found in Del Soldato et al. (2018) and Farolfi et al. (2019b), in which the PSI velocities from dual orbits were aligned and then corrected using the GNSS values. In Khorrami et al. (2019), a S1 descending orbit dataset was processed and the results were combined with in-situ measurements, such as groundwater and GNSS measurements for a more complete interpretation of the data. However, these previous studies based on S1 data lack contemporaneity between the datasets; moreover, none of them explored the vertical and horizontal displacements fields with calibrations in an absolute reference frame followed by an accuracy assessment

procedure.
The SNAP–StaMPS workflow provided a final persistent scatterer time series that can depict linear trends and periodical signatures along the slant direction with a points dispersion of few mm, with no further filtering procedures. The comparison between CGNSS and PSI-derived velocities allowed to define differences of 2 mm/yr in worst cases with uncertainties at mm/yr. In this computation, the incidence angle must be referred to the area where the reference site is placed. The PS time series appeared less reliable at the beginning of the reference period, when only the S1A data were available and a void of data was found in the first half of the year 2016, due to the lack of S1 radar images in the repository used.
The workflow has revealed to be useful in the detection of deformation phenomena at the millimeter level, like those affecting the Po Plain sedimentary basin. The spatial and temporal variability of the ground deformation driven by anthropogenic causes, such as gas and groundwater exploitation, might be significant and this dual approach based on GNSS and InSAR offers a possible solution. A study of the spatial distribution of the phenomena is also necessary, especially when the adopted techniques have an important difference in terms of the spatial distribution: the single point for the GNSS measurements and a relatively large number of targets at the ground for the multi-temporal SAR technique. For these reasons, we processed the same observation time span ($2015 - 2019$) for the GNSS and SAR observations and the comparison between the results obtained, performed in a selected validation area, shows a good agreement between the vertical and horizontal (East-West) velocity values (Table 2.2).
The ground deformation maps produced in the present study update previous investigations commissioned by the Regional Agency for Environmental Prevention, on behalf of the Emilia-Romagna Region; such studies were initially based on traditional topographic surveying (Bitelli et al. 2015). From 2005, single-orbit SAR interferometry based on radar images provided by ERS, Envisat and Radarsat satellites was used to depict the subsidence phenomena over the area, thus assuming a negligible horizontal motion. These previous studies provided updates up to the year 2016 (Bitelli et al. 2020) and a reliable benchmark for the present investigations, even though no studies based on dual-orbit and vector decomposition are available. The maps of Figures 2.5, 2.6 and 2.7 depict the current subsidence phenomena in the metropolitan area of Bologna, in addition to ground deformation phenomena that affect the nearby settled areas representing a recent update on the modern subsidence rates and a valuable tool for stakeholders involved in finding countermeasures to land subsidence after the continuous reduction in the amount of groundwater pumped by supply stations located within the study area (A.R.P.A.E. 2018).

2.4 Final remarks

In this Chapter, a procedure for the estimation of the uncertainties associated to the vertical and East-West components of the mean PS velocities has been proposed. In particular, the variance-covariance matrix associated to the decomposed velocities has been derived from the variance-covariance matrix associated to the vector of the ascending and descending slant oriented velocities and the acquisition geometries. In addition, a validation procedure of the SAR decomposed results with velocities from GNSS observations has also been proposed.
The open-source SNAP-StaMPS processing strategy, presented in Chapter 1, has been

applied to a dual orbit set of Sentinel-1 data over the eastern sector of the Po Plain (Italy) and the accuracy of the results have been investigated and validated according to the above mentioned procedure. Results show that the developed workflow, complemented by a procedure to process contemporary CGNSS site velocities to refer the LOS-projected velocities by the InSAR approach to the modern ETRF2014 and an algorithm for decomposition analysis at preferred spatial resolution, allows the investigation of ground deformation due to subsidence phenomena over large extent. Moreover, the validation performed at 10 CGNSS sites provided differences between decomposed SAR and GNSS annual rates at the millimeter level with larger values at 2mm/year, thus showing substantial agreement between the PSI-based and GNSS measurements. Moreover, the computed difference values are compatible with the uncertainty level provided by the error propagation analysis.
Even though the accuracy assessment provided a satisfactory outcome, more effort could be focused on the investigation of the algorithms other than the linear phase-based model for the atmospheric phase correction. However, the study area is characterized by a prevalently flat topography, and these data can be considered as an improvement in the understanding of ground deformation processes that affect the area as a response to underground resource exploitation.
The combined use of the SNAP-StaMPS and TRAIN processing tools offers an opportunity for users who are interested in processing freely available Sentinel-1 SAR images; moreover the open code of StaMPS represents a positive point for the possibility for the users to introduce personalized routines, as it was did for the calibration, vector decomposition and uncertainties assessment with validation steps during this research activity.

Chapter 3

PSI-based separation of the ground deformation contributions

In this Chapter, an approach for the investigation and separation of ground deformation contributions combining multi-temporal satellite interferometry and Geographical Information Systems analysis is presented. In particular, the relationship between displacements occurring over built environment and consolidation processes will be investigated exploiting a dual-orbit Sentinel-1 SAR dataset and descriptive attributes related to the age of construction and intended use over the municipality of Ravenna (Emilia Romagna, Italy). The aim of the presented approach is to assess and filter out the mentioned contribution to the subsidence phenomena to quantify the local overestimation of the subsidence due to consolidation processes.

3.1 Introduction

Thanks to the ability of the multi-temporal interferometric techniques to detect the LOS mean velocity of targets at the ground at a high accuracy level ($1 - 2$ mm/yr) and the spatial resolutions up to few meters of the more recent SAR missions (e.g. Sentinel-1, Radarsat, COSMO-SkyMed and TerraSAR-X) (Casu et al. 2006; Crosetto et al. 2016), investigations about natural and anthropogenic components of subsidence taking advantage of these techniques have been widely presented in the scientific literature (Gabriel et al. 1989; Ferretti et al. 2000; Teatini et al. 2006; Stramondo et al. 2007; Bitelli et al. 2015; Del Soldato et al. 2018; Cian et al. 2019; Delgado Blasco et al. 2019; Mancini et al. 2021; Li et al. 2022). Moreover, since the main sensitivity of the technique towards displacement occurring along the vertical and, at less extent, in the East-West directions (Hanssen 2001; Samieie-Esfahany et al. 2009), SAR interferometry, complemented by few GNSS observations, can be considered a powerful method to detect subsidence phenomena at the desired spatial scale (Farolfi et al. 2019a). As additional advantage of multi-temporal SAR interferometry, the temporal and spatial analysis of the detected displacements provides further insights into the deformation phenomena and their possible natural and anthropogenic drivers (Carminati and Martinelli 2002; Teatini et al. 2011; Tosi et al. 2013). More recently, few papers focussed on GIS-based post analyses of SAR products for advanced applications have been reported (Qiu et al. 2021; Radman et al. 2021; Barra et al. 2022).
Very often, subsidence phenomena are investigated over areas where major cities have been

developed and, furthermore, the built environment is particularly suited for analysis based on Persistent Scatterers. However, the different natural and/or anthropogenic sources of subsidence in settled areas cannot be distinguished, being the measured displacement of scatterers the overall displacement occurring at the ground. Different contributions compose the overall phenomenon, such as long-time trends of natural compaction processes of fine-grained sediments, groundwater table depth variation in response to pumping for industrial and drinking purposes (Stramondo et al. 2008; Abidin et al. 2011; Dang et al. 2014; Chen et al. 2015; Qin and Perissin 2015; Lyu et al. 2020; Bui et al. 2021), gas storage/exploitation or activities related to oil industries (Bertoni et al. 1995; Teatini et al. 2005; Simeoni et al. 2017; Mancini et al. 2021) and mining activities (Samsonov et al. 2013; Wang et al. 2022).

Moreover, the consolidation processes due to recently built structures load could further affect the subsidence mapping, in particular for studies devoted to the analysis of ground deformation phenomena at local scale (superficial effects of groundwater and gas reservoir exploitation, tunnelling, excavation), where the spatial deformation pattern could be strongly affected by the consolidation processes for more than two decades (Chen and Liew 2002). With reference to consolidation processes after construction, Ketelaar et al. (2020) and Van Leijen et al. (2021) proposed a method for the classification of scatterers to better distinguish between deep and shallow processes; in these works the targets are separated into two groups (i.e. the well-founded objects sensitive to deep processes only and those sensitive to the total ground motion) exploiting a criterion based on the relative scatterers height with respect to the terrain height. However, in some cases, due to the local stratigraphic setting, the building displacements could be sensitive both to superficial and shallow processes and the approach proposed in the mentioned papers cannot be adopted.

The relationship between subsidence and possible causal factors has been reported in particular for megacities around the world and the attempt to separate natural and anthropogenic components of subsidence has been limited to further investigation on imposed load and the construction age of the buildings (Tang et al. 2008; Xu et al. 2012; Solari et al. 2016). However, a quantitative separation between natural and anthropogenic components of subsidence into possible contributions is still an open problem requiring a more advanced integration between results provided by SAR interferometry and available geospatial datasets. In particular, the quantification and separation of target displacements detected by SAR interferometry, which are not due to common subsidence phenomena, provides a better understanding of the specific phenomenon of interest and avoid the overestimation and mis-interpretation of subsidence trends because of the influence of unexpected factors, such as the consolidation processes of recent settlements. For this purpose, an approach that integrates GIS-based spatial analysis and measurements from multi-temporal InSAR could be employed. However, the application of these approaches for consolidation processes assessment is still in a superficial stage. A deeper integration with the GIS environment was proposed by Tomás et al. (2019) and Macchiarulo et al. (2022) who adopted clustering analyses to define structural deformation processes and by Scivetti et al. (2021) who investigated the relation between LOS velocities and urban growth at the neighbourhood scale and geomorphologic features. In the attempt to better understand the anthropogenic processes affecting subsidence studies by integrating GIS data about the built environment, Fiaschi et al. (2017) introduced the contribution of the land use changes in the interpretation of land subsidence retrieved from the analysis of ERS-1/2 and TerraSAR-X images. A correlation between increasing values of subsidence

rates and a land use change to construction unit was also shown and interpreted as an effect of sediments compaction caused by the load of the newly constructed building.
In this Chapter, we introduce an approach based on the combination of SAR interferometry and spatial analysis by GIS to improve the separation among natural and anthropogenic components of subsidence over the municipality of Ravenna (Italy), a 650 km^2 wide study area in which subsidence phenomena can be observed. In particular we focused on the use of large dataset to quantify the displacement of targets due to external factors, such as consolidation processes under building loads and their dependency from the age of construction for selected intended uses. To this aim, displacements obtained from the processing workflow SNAP and StaMPS of ascending and descending Sentinel-1 data (already presented in Chapter 1) have been combined with GIS geometric and descriptive data and GNSS observations.

3.2 GIS-based separation of consolidation processes contributing to the subsidence

In this Chapter, the proposed methodology will be exemplified through the Ravenna case study. In fact, the variety in space, time and causes of the phenomena affecting the area make the selected case study particularly suited for the declared purposes. Moreover, an unusually rich GIS building dataset related to the Ravenna city has been made available by the municipality. The details regarding the phenomena affecting the study area and the available GIS dataset are presented in Sections 3.2.1 and 3.2.2, respectively.

3.2.1 Study area

In the presented application, the area of the municipality of Ravenna (Emilia-Romagna, Italy) is taken into account as the study area. This area is a lowland belonging to the eastern area of the alluvial Po plain and faced to the Adriatic Sea; it is characterized by coastal zones with elevation not exceeding 2 meters above sea level (a.s.l.) with large portions below mean sea level and the presence of land reclamation, wet areas and salt marshes (see Figure 3.1).
In the last decade, due to the combination of anthropogenic and natural geological processes, cumulative rates of subsidence up to 5 mm/yr in the city centre of Ravenna and inner sectors and 15 mm/yr over limited extent of coastal stretches occurred (A.R.P.A.E. 2018; Polcari et al. 2022). Natural and anthropogenic components of subsidence in the study area have been deeply investigated by several authors. Rates of natural land subsidence arise from the combination of deep downward tectonic movement (Carminati et al. 2003a) and the compaction of recent Holocene (Quaternary) sediments (Teatini et al. 2011). Gambolati and Teatini (1998) estimate a natural subsidence rate in the area of about $2-3$ mm/yr over the last $2,500$ years and Antonellini et al. (2019) assigned 0.9 mm/yr of the total estimate to primary consolidation processes of the fine-grained prodelta levels. In the area, the anthropogenic land subsidence was caused by the fast industrial development occurred in the years after the World War II and is mainly due to groundwater pumping from shallow and deep aquifers and to gas exploitation from Plio-Pleistocene inland and offshore reservoirs (Bertoni et al. 1995; Teatini et al. 2005). The extents of the shallow aquifers and of the Angela and Angelina off-shore reservoir are reported in Figure 3.1.
These factors caused an intense subsidence that reached the value of 110 mm/yr during the 1970*s*. The actions undertaken in the late 1970*s* and 1980*s* by the municipality reduced the groundwater pumping and, thus, the subsidence rate reduced to the values registered

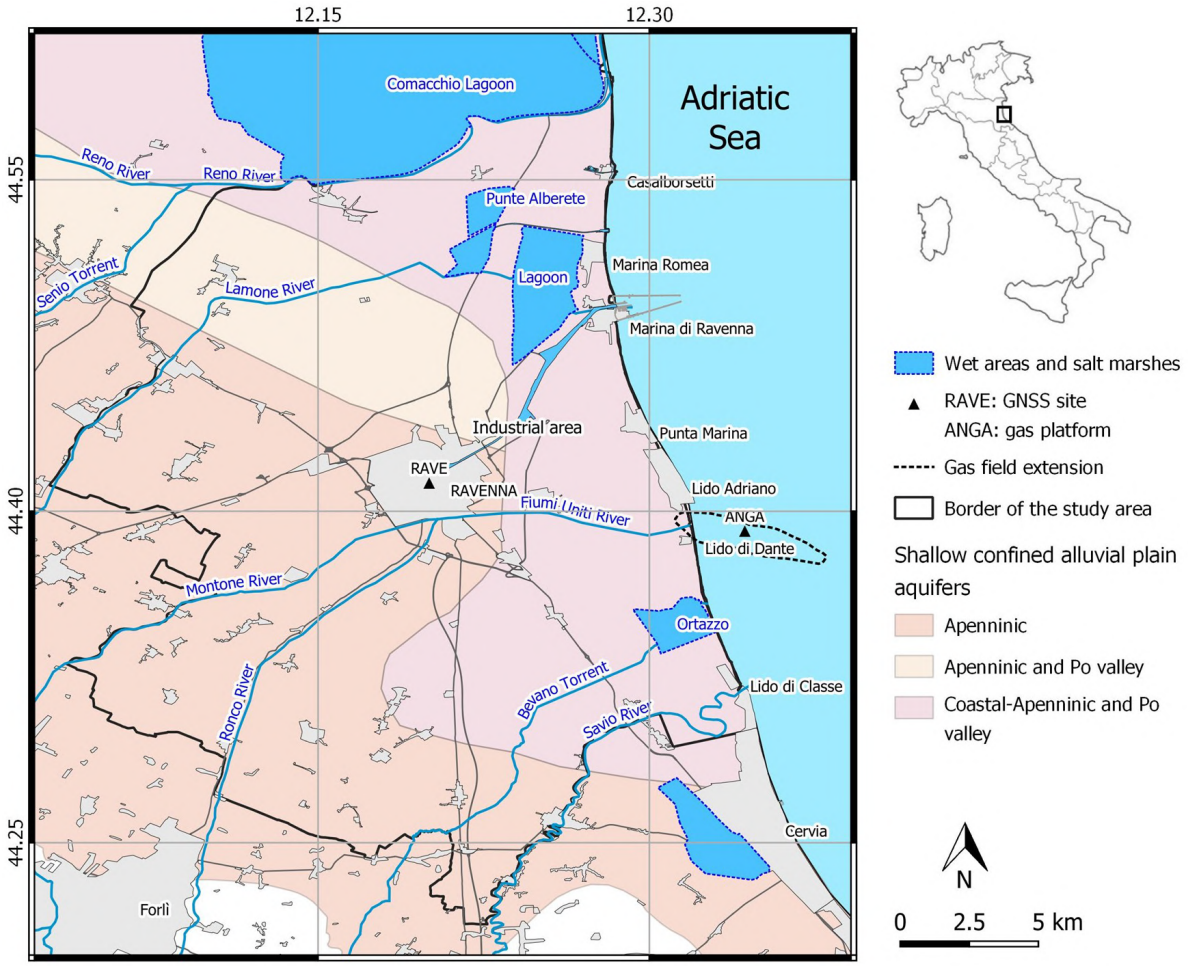

Figure 3.1: Map of the study area with borders of the municipality of Ravenna (Emilia Romagna, Italy), the extension of the gas field and the shallow confined aquifers. ANGA: Angela and Angelina off-shore platforms for natural gas exploitation; RAVE: Continuous GNSS station.

in the first half of the 20th century (Teatini et al. 2005, 2006). During the last two decades, the mainland appeared to be stable or slightly subsiding, while part of the coastal areas still present a subsidence of about 10 mm/yr. In particular, some criticalities still remain in the area of Lido Adriano, Lido di Dante and in the industrial area between Marina di Ravenna and the city centre (Teatini et al. 2005). These trends were confirmed by the DInSAR analyses carried out by Antoncecchi et al. (2021) in the periods $1995 - 2010$ and $2015 - 2018$. The total amount of land subsidence, in addition to recent trends in sea level rise up to 2.2 ± 1.3 mm/yr (Cerenzia et al. 2016), made the coastal areas strongly vulnerable to erosive processes and opened problems connected to engineering works for coastal protection of the settlements (Sytnik and Stecchi 2014).

3.2.2 Dataset and processing strategy

The presented application integrates displacement from the implemented PSI method and a GIS dataset of the built environment. In the following, the interferometric dataset and processing strategy and the GIS dataset are presented.

Interferometric dataset and processing S1 SLC data acquired with the IW mode were processed with the open-source procedure described in Section 1.3 and depicted in Figure

Table 3.1: The Sentinel-1 dataset over the municipality of Ravenna.

Orbit	Track	Number of images	Master date	Start date	End date	Subswath	θ
Ascending	117	216	03/10/2017	30/03/2015	18/08/2020	IW2	46°
Descending	95	170	05/05/2017	12/10/2014	17/08/2020	IW2	43.9°

Note: θ is the mean incidence angle at RAVE station.

1.4 which exploits a combination of the software SNAP, StaMPS, TRAIN and MATLAB routines for the calibration and decomposition of the SAR products. In particular, the DEM SRTM with a resolution of 30 m has been selected and employed to remove the topographic phase contribution. The linear phase-based model was employed to compute and subtract the atmospheric phase contribution. The details on the interferometric ascending and descending S1 dataset can be found in Table 3.1. Moreover, the local deformation trend as provided by Bonetti et al. (2022) was taken into account to refer the LOS velocities to a common reference frame (i.e., for the calibration step); to this aim, the CGNSS station RAVE was chosen as reference station. RAVE station is located in the centre of the study area (as can be seen from Figure 3.1) and the provided velocities refer to an observation period that overlaps with the interferometric dataset and amounts at

$$
\begin{aligned}
v_{\text{up}}^{\text{RAVE}} &= -4.6\,\text{mm/yr} \\
v_{\text{east}}^{\text{RAVE}} &= 1.0\,\text{mm/yr} \\
v_{\text{north}}^{\text{RAVE}} &= 3.1\,\text{mm/yr}
\end{aligned}
$$

in which the ETRF is adopted to remove the Eurasian plate motion. Similar rates of subsidence have been reported by the Regional Environmental Protection Agency of the Emilia Romagna Region (ARPAe) (A.R.P.A.E. 2018).
In this application, the validation step of the SAR results using GNSS observations (as presented in Chapter 2) is omitted; for this reason the uncertainty related to the GNSS velocities are not reported.

GIS dataset The employed GIS dataset is composed of information related to the urbanized and natural environment. These data are available in the geographic repositories of the Emilia Romagna Region and the Municipality of Ravenna through the open-source data management system Comprehensive Knowledge Archive Network (CKAN) developed by Open Knowledge Foundation to publish, share and use open data by handling geospatial ArcGIS portals and major metadata schemas. The layers representing the built environment are available as shapefiles (*.shp*) and Feature Collections in geoJSON (*.JSON*) formats. Besides the geometric entities included in the layers, detailed descriptive attributes fundamental in the successive spatial analysis have been also provided. In particular, the information layers relating to the classes of buildings and constructions were used in which 60700 buildings are represented with additional fields containing information useful for the present study such as the intended use, year of construction, subsequent maintenance, restructuring interventions and many others. Among the list of intended uses listed in the attributes of the dataset, civil and industrial have been considered.

3.2.3 Methodology

The proposed approach relies on the combination of the PSI processing of the dual-orbit S1 dataset and analyses performed in a GIS environment. The main objectives of the method can be summarised as:

1. the estimation of the building consolidation contribution to the overall subsidence,
2. the estimation of the long-period (i.e., natural) subsidence,
3. the computation of the residual rates due to local phenomena.

The residual rates are defined as the components of the velocity that still remain after the computation and subtraction of the natural component and the temporary effect due to the consolidation processes under building loads from the ascending and descending slant velocities.
To assess the possible relationship between the displacements of scatterers representing buildings and the age of construction, the GIS dataset including buildings with the related ages of construction was used. Then, the computed contribution and the long-period subsidence component are subtracted from the the budget of the overall subsidence phenomena enabling the analysis of residual displacements. The workflow of Figure 3.2 summarizes the proposed approach in which the LOS-oriented velocities for each orbit are used to preserve the full resolution of the SAR data.

Intersection between SAR products and building dataset The first step is the intersection of the slant ascending and descending set of mean PS velocities with the dataset of the buildings. However, establishing the spatial relations (e.g. membership or proximity) between the PS and building parts producing a response to the radar pulses is not trivial when data from a moderate resolution (i.e. tens of meters) satellite sensor are used, such as those from S1 constellation. Furthermore, the geocoding of scatterers over a grid oriented along the azimuth and range directions and errors at few meters level in the spatial positioning of the scatterer make the analysis at building-scale even more difficult. For this reason, in order to define the spatial relation between scatterer locations and building shape complemented by descriptive attributes, a preliminary spatial clustering was performed to delineate urban areas characterized by a common age of construction. The clustering was achieved with a sequence of operations based on vector geometry tools available in QGIS and data attributes. First, polygons representing the buildings were grouped on the basis of the construction year and intended uses. A buffer with a fixed distance of 2 m was therefore created for all the features in the input layers. Then, buffers characterized by the same construction year and a particular intended use were dissolved into single multipolygon layers. Finally, spatial criteria were used to assign attributes such as the year of construction and intended use of derived polygons to the descriptive features of single PS. PSs falling into more than one polygon or outside any polygon were excluded from the dataset. The described first step produces as output the dataset composed by the ascending and descending set of PSs related to the buildings.

Consolidation processes related to the building year of construction and natural subsidence estimation From the new set of data, the mean LOS velocity related to each year of construction is computed and the plot representing the relation between the mean LOS velocities and the year of construction of the buildings is constructed. From the

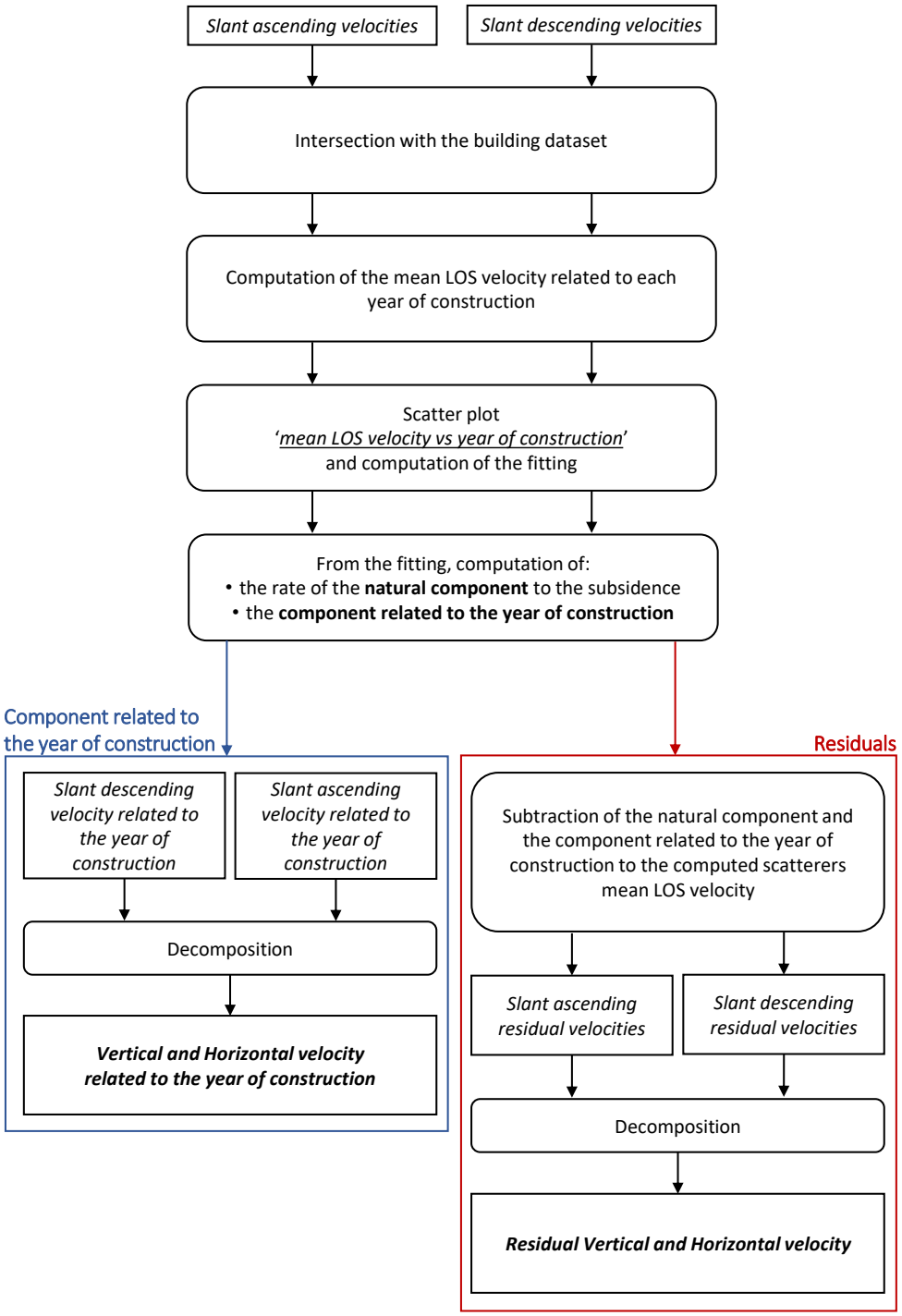

Figure 3.2: The workflow adopted in the processing of residual slant velocities after subtraction of natural subsidence and displacements due to built areas consolidation.

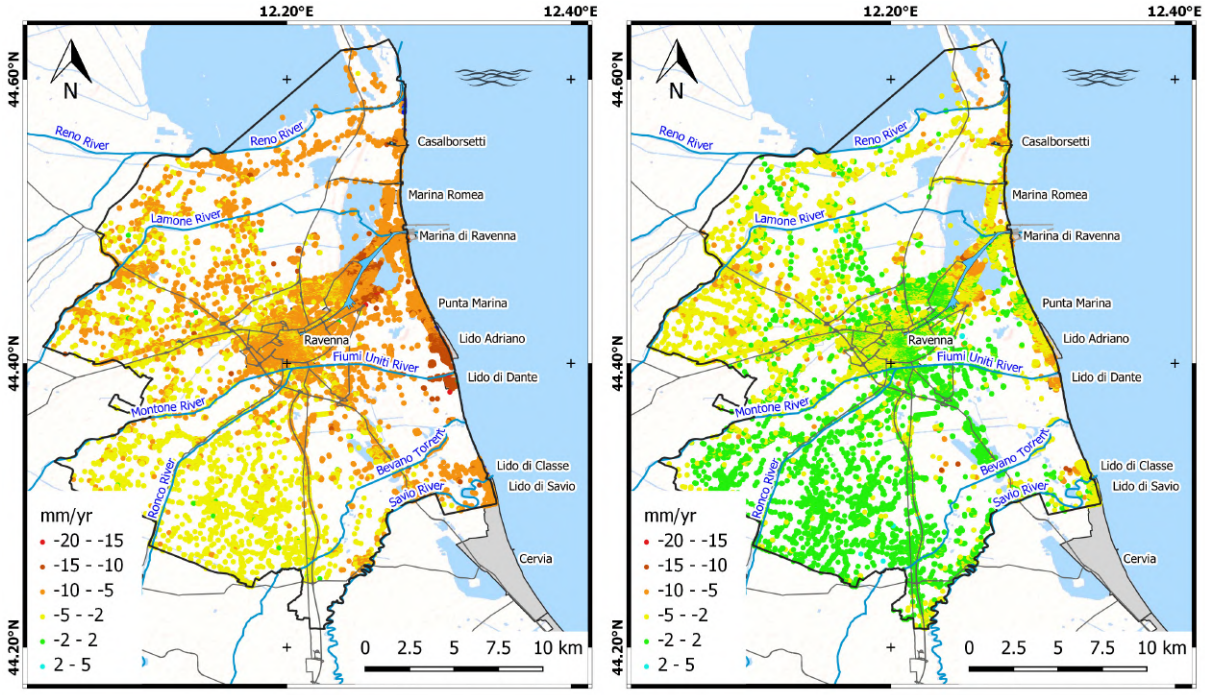

Figure 3.3: Ascending (left) and descending (right) slant oriented velocity maps (mm/yr) over the municipality of Ravenna.

fitting of the data in the plot, the natural component to the subsidence and the component related to the year of construction of the buildings can be retrieved.
As far as the latter is concerned, the decomposition of the slant ascending and descending set of velocities related to the year of construction is performed and the vertical and horizontal velocities induced by the compaction of the ground due to the construction of a building is computed; therefore, the relation between the occurred displacement and the year of construction of the building itself can be assessed.

Residual rates analysis Once the cited two contributions (i.e., the natural component and the contribution related to the buildings year of construction) are known, they can be removed from the mean LOS velocities of the scatterers. Then, the decomposition of these residual velocities is performed to retrieve the horizontal and vertical velocities due to local phenomena that have not been modelled as natural subsidence or effect of the buildings construction.

3.2.4 Results and discussions

The interferometric processing as reported in Figure 1.4 produced the ascending and descending LOS-oriented calibrated velocities shown in Figure 3.3. However, given the application and the resolution of the S1 data, the step concerning the correction of the PS coordinates after the residual topographic error estimation was not performed.

The first step of the workflow proposed in Figure 3.2 is the intersection between the PS LOS-oriented velocities presented in Figure 3.3 and the building dataset in a GIS environment. Then, to investigate the relationship between averaged ascending and descending slant velocities for civil and industrial buildings and the year of construction of the buildings themselves, the plot shown in Figure 3.4 is proposed.

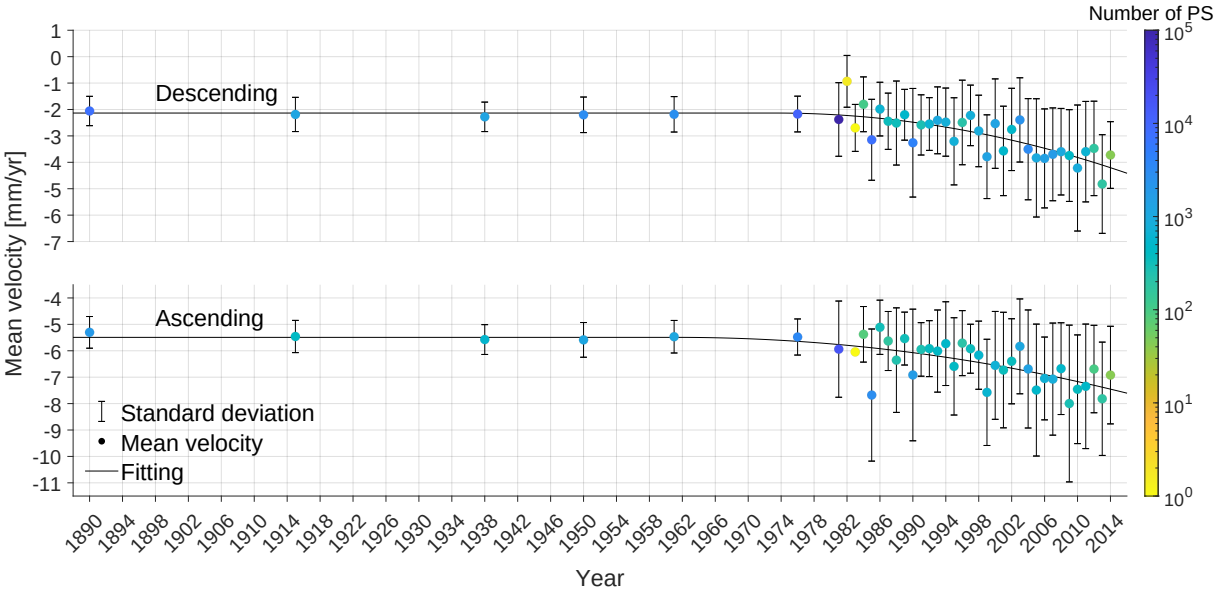

Figure 3.4: Descending (top) and ascending (bottom) mean Line Of Sight velocities of the Persistent Scatterer versus the buildings year of construction and their fitting.

The steps followed to produce the plot are described in the following. First, the attributes (e.g. the mean LOS velocity and the year of construction) of a building were inherited from each PS belonging to that building. Then, for all the PSs of all the buildings with the same year of construction, the mean of the mean velocity is computed, thus, having a single value of velocity representing each year of construction. For the computation of the mean velocity, forty-four thousands and thirty-eight thousands of PSs were considered for ascending and descending orbit, respectively. Finally, the mean LOS velocity values versus the years of construction and the fitting of these scatterers were plotted. The color of the scatterers in Figure 3.4 represents the number of PSs belonging to buildings constructed in the same year (i.e. the number of PSs used to compute the mean velocity related to a given year). The vertical bars in correspondence with the scatterers represent the standard deviation of the computed mean velocity. The fitting function is a piecewise continuous function of the construction year composed by a constant and a parabola branch. The value of the constant, the year in which the two functions join and the parabola concavity (i.e. the variables of the fitting function) were obtained solving a constrained non-linear multivariable minimization problem in which the mean squared error between the fitting function itself and the mean velocity value is minimized. The described procedure was carried out for both the orbits to compute the LOS mean velocity of buildings PSs versus the year of construction of the buildings themselves and infer the relation between them. As can be inferred from Figure 3.4 for both orbits, the mean LOS velocities of PSs belonging to buildings constructed before 1980 have a constant rate. Up to this year, the mean LOS velocity has a constant value of approximately -2 mm/year and -5.5 mm/year for the descending and ascending orbits, respectively. This rate is detected differently by the observing geometry (i.e. from different incidence angles as can be seen from Table 3.1) and can be accounted for as the long-period natural component of the subsidence, affecting all the scatterers in the study area. The buildings constructed in the last three decades exhibit increasing values of the mean LOS velocity. For instance, for the descending orbit, as can be seen from the fitting, the mean LOS velocity has a value of -2.2 mm/yr for 1980 and -4.2 mm/yr for 2014. Similarly, for the ascending orbit, the values read by the fitting

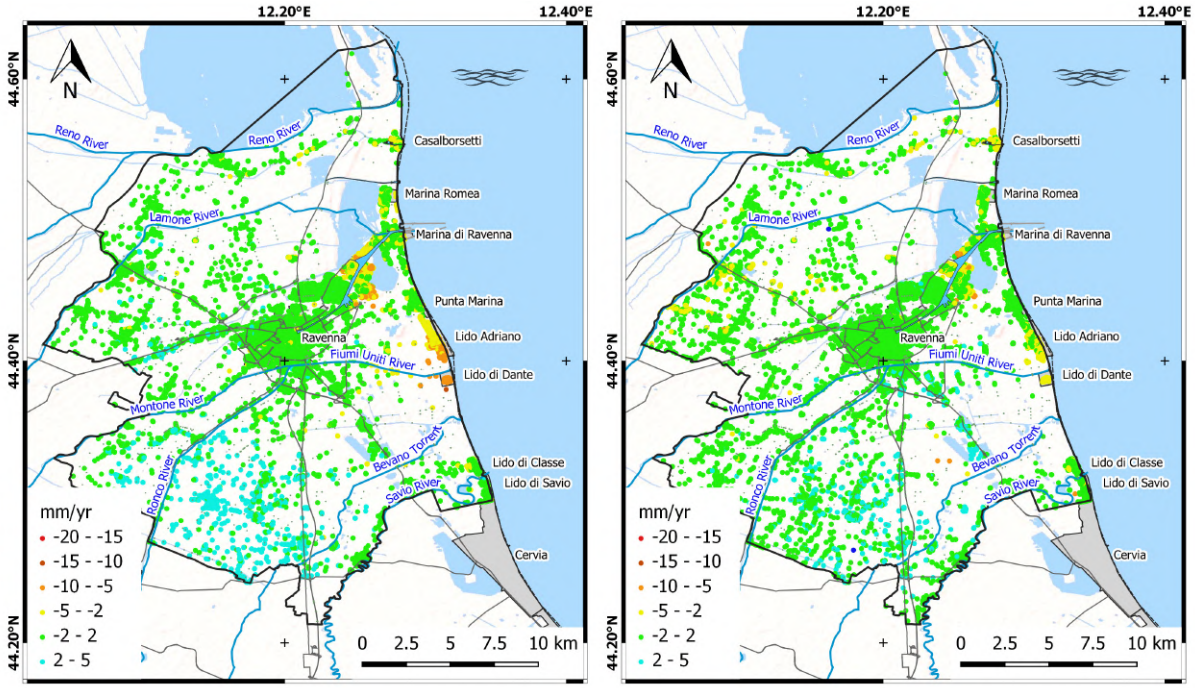

Figure 3.5: Ascending (left) and descending (right) slant oriented residual velocity maps (mm/yr).

are −5.8 mm/yr and −7.5 mm/yr for 1980 and 2014, respectively. Figure 3.4 could be therefore considered as representative of the cumulative subsidence produced by long-term subsidence and time-dependent consolidation processes. Besides the relationship between the slant velocities and the year of construction, an increase of the standard deviations could be observed from the last decades involved; this is likely due to the influence of consolidation processes that, based also on the local stratigraphic setting and construction mode, start to show their effects on more stable long-term displacements. Increasing values of displacements along the slant direction with respect to the year of construction of buildings could be referred to an anthropogenic source due to consolidation processes under the building loads. It contributes to an overestimation of the natural subsidence phenomena or any other deformation processes investigated by the SAR interferometry. To bring phenomena that deviate from the behaviour represented by the fitting curve into evidence, the mean velocity values as read by the fitting curve for each year of construction were subtracted from the corresponding mean LOS velocities of PS. The computed residues are therefore related to local deformation phenomena where long-term displacements and the effect of consolidation processes have been filtered out. The results of the described procedure for both orbits and the corresponding decomposition along the vertical and East-West directions are shown in Figures 3.5 and 3.6, respectively.

Residual vertical and horizontal velocities (Figure 3.6) show well-defined ground deformation patterns. In the vertical direction, the residual subsidence phenomena other than the natural long-term trend and consolidation processes are located in the coastal villages and industrial areas. Regarding the horizontal direction, displacements in the East–West direction show very well delimited spatial pattern mostly located in the coastal village of Lido di Dante and nearby industrial area where velocity field pointing at the East is visible. The possible connection with an offshore gas exploitation activity will be further addressed in the discussions paragraph. Conversely, a wide area located in the central-western portion of the municipality of Ravenna exhibits horizontal velocities oriented in the West direction.

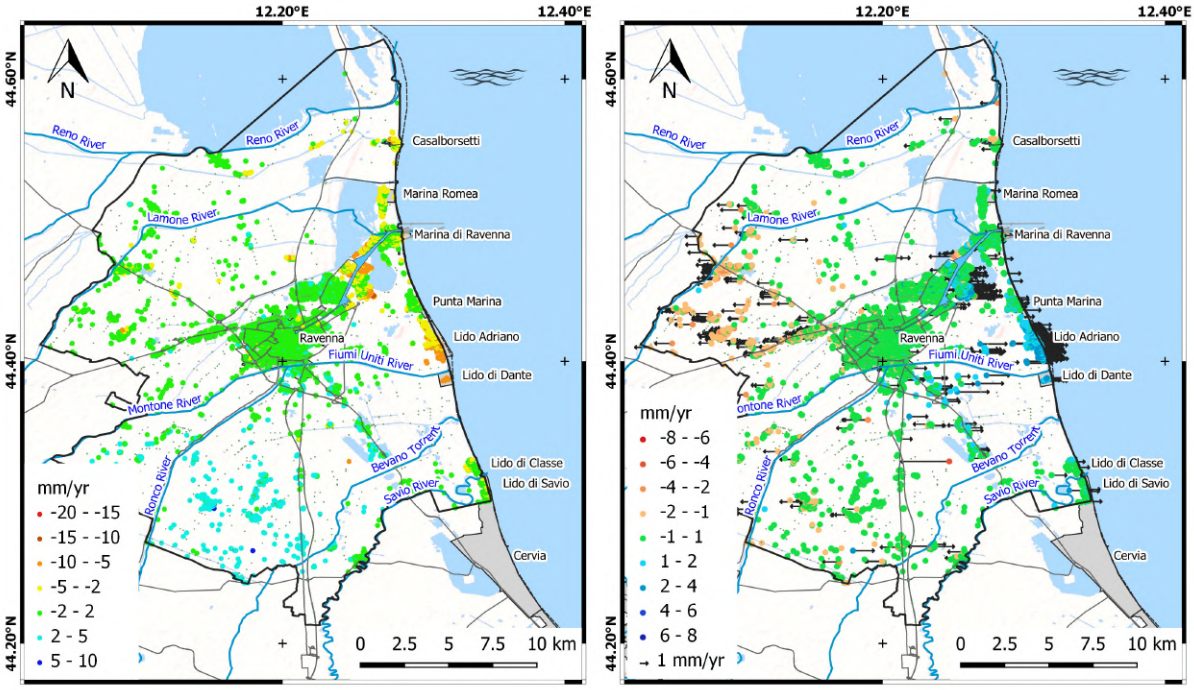

Figure 3.6: Vertical (left) and horizontal (right) residual velocity maps (mm/yr).

To quantify the effect due to consolidation processes, the mean rate of natural subsidence detected along the LOS directions (i.e. the constant value of the fitting in the plot of Figure 3.4) was subtracted from the rates detected at any time of construction. Such procedure enabled the computation of the anthropogenic contribution to the overall subsidence due to consolidation processes. For a better understanding of ground deformation due to the mentioned process, the obtained ascending and descending velocities due to anthropogenic processes were decomposed into the corresponding vertical and horizontal components (Figure 3.7). In agreement with the hypothesis of consolidation processes, Figure 3.7 shows a major contribution along the vertical direction, whereas the horizontal component of displacements is very close to zero throughout the area.

For a clearer interpretation of the contribution of consolidation processes to subsidence, Figure 3.8 shows detailed maps of LOS-oriented displacements over the coastal villages of Casalborsetti and Lido di Classe marked in Figure 3.7 as area 1 and area 2, respectively. These areas have been selected to better represent the effect of the consolidation processes over recently built sites. Their limited areal extension allows to represent at detailed scale the LOS-oriented displacements that appear more and more pronounced when constructions are more recent. The effect of anthropogenic processes due to consolidation is very well detected once the natural processes have been subtracted. Conversely, the consolidation processes could be masked by natural phenomena when a cumulative effect is observed by the InSAR analysis.

Discussions The presented results obtained from the spatial analysis of multi-temporal DInSAR data support a better understating of subsidence phenomena due to natural and anthropogenic causes. The separation of such components allows to quantify and filter out the possible contribution of consolidation processes under building loads occurring over recently settled urban and industrial areas. Potentially, any investigation about ground deformation phenomena based on multi-temporal DInSAR could be strongly biased by such

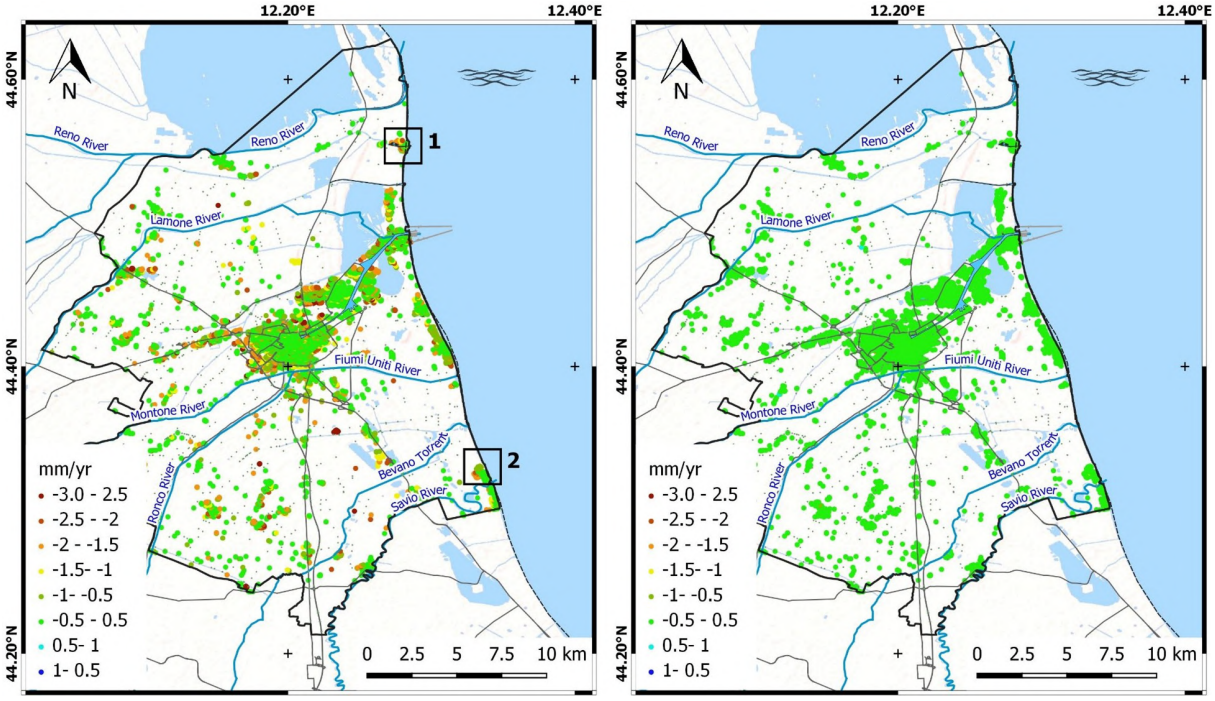

Figure 3.7: Vertical (left) and horizontal (right) velocity maps related to anthropogenic processes (mm/yr)

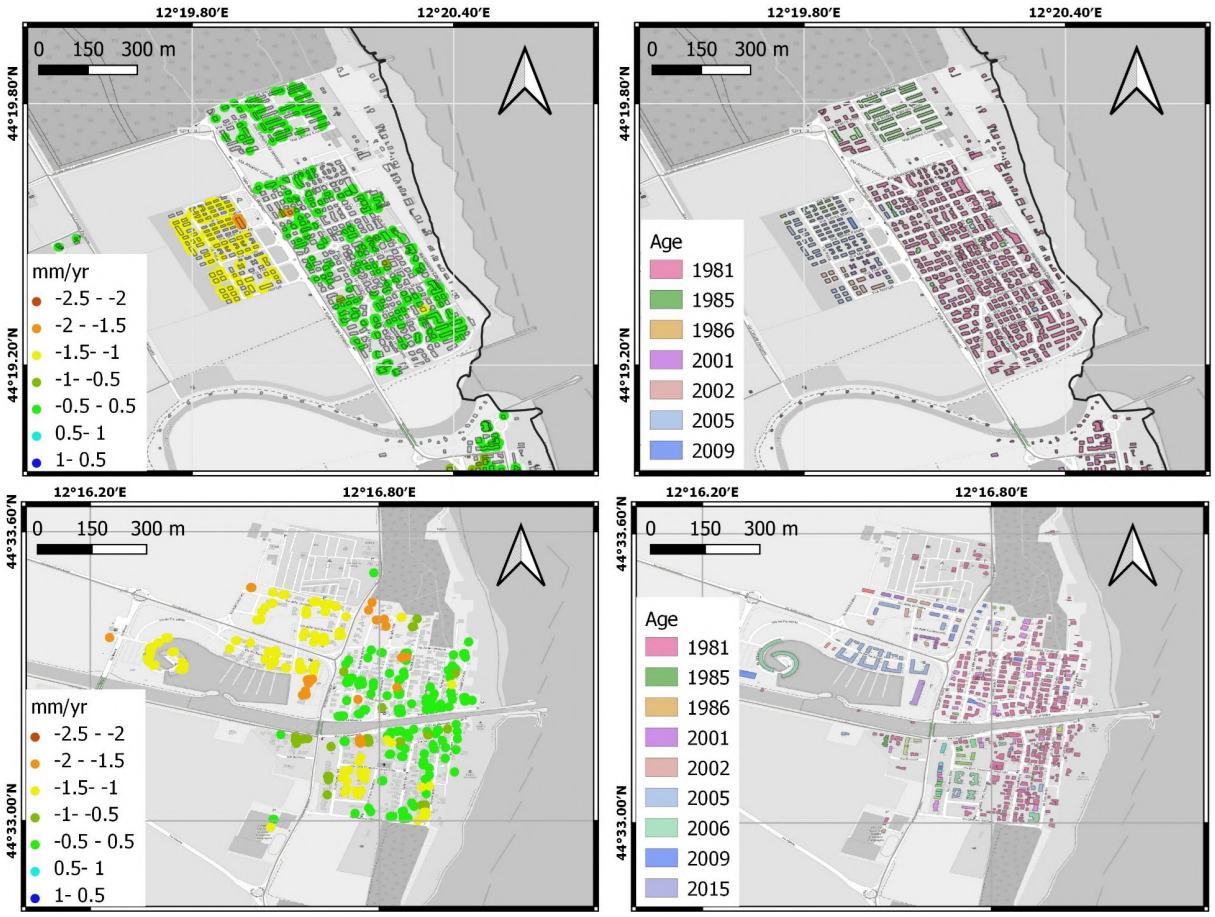

Figure 3.8: Comparison between the anthropogenic ascending slant velocity maps (left) and the buildings age (right) for the coastal villages of Lido di Classe (top) and Casalborsetti (bottom).

processes. Generally, the consolidation processes are not accounted for and contributions to subsidence of other driving factors could be overestimated. It is the case of DInSAR-based investigations focused to developing areas where consolidation processes could be dominant and related to construction and geotechnical factors (building loads, characteristics of the foundation layer, superficial terrain stratigraphy, geotechnical approaches to structural designing). The relationship between consolidation processes and the age of buildings found in this research application could further inform on deformation processes occurring at the ground improving the ability to detect displacements due to factors acting at local scale. Moreover, in the investigated area, the consolidations processes seems to be active for more than two decades (Grassi et al. 2022), a period covering the majority of investigations on subsidence phenomena based on DInSAR methods. It is worth noting that the obtained results are related to the stratigraphic setting of the study area, however, the proposed methodology could be applied in other study areas characterized by different settings and the results will highlight consolidation phenomena of different entities.

In this framework, the integration between DInSAR measurements and GIS data, representing buildings with the age of construction, provided a valuable tool in distinguishing consolidation processes after construction from other factors. For instance, residual vertical velocities due to such consolidation processes up to 3 mm/yr have been retrieved in the study area, well beyond the mm-level sensitivity of the DInSAR method in the detection of annual rate of displacements.

To further improve the reliability of the proposed analysis, the relationship between subsidence rates and age of construction should be established over areas characterized by an homogeneous stratigraphy. It requires additional information as a vector layer representing the superficial stratigraphic layers. In the presented application, the study area is characterized by a repeated alternations of coastal and alluvial deposits due to marine transgressive-regressive cyclicity and the coastal villages suffering from major subsidence phenomena were settled over well-drained floodplain (Campo et al. 2017). Such stratigraphic patterns could be considered as representative of the whole coastal areas where major subsidence rates have been detected. However, the presence of different superficial sedimentary bodies (for instance deposits of fluvial channels) may alter the susceptibility to consolidation processes after construction. Future works on the effects of consolidations processes would greatly benefit from improvements in the GIS dataset with regards to the collection, standardization and introduction of parameters from the geotechnic and structural engineering domains. In fact, soil consolidation is potentially affected by several factors such as the building dimensions and weight and the type of foundation. However, foundation design criteria typically limit the maximum soil pressure and/or settlement that can be caused by the building construction. This implies that different buildings realized during the same period have been conceived to cause the same soil pressure and/or settlement. On the contrary, buildings realized at different ages can produce significantly different soil pressure and settlement depending on the limit imposed by the current foundation design criteria and standards. However, such detailed information regarding the buildings is not extensively available in GIS repositories and more simple descriptions must be adopted in their place to predict or assess the consolidation settlements.

The relationship of Figure 3.4 should be considered as a representative of a general behavior for the dominant stratigraphic setting. However, across the decades the foundation design criteria and the constructive technique of the building (and the typical floor weight with it) evolved and, consequently, the consolidation processes could reflect the designing approach

at the age of construction. For instance, lightweight floors with no concrete slab were typically realized in the 1960s and 1970s, while later in the 1990s concrete slabs became very common. Similarly, wooden roofs have become widespread from the 2000s. All of this means that the age of construction is a synthetic parameter that can represent the several effects affecting the soil consolidation. As a general remark, we may observe that the consolidation processes could represent the totality of the deformation processes due to post-construction settlement within areas of recent urbanization where scatterers are mostly represented by roofs. An approach useful in the quantitative assessment of such a contribution should be adopted.

Figure 3.8 shows LOS-oriented displacements of $2 - 3$ mm/yr over some areas likely due to consolidation settlements of buildings constructed after the year 2000. Approximately, it represents the 20% of the cumulative displacements reported in Figure 3.3 in the same areas. Such contribution should be removed from the ground deformation processes to better represent subsidence phenomena and the related driving factors. On the other hand, the subtraction of the long-term rate due to natural subsidence and consolidation processes allows to depict the influence of residual phenomena reported on map of Figure 3.6 by decomposing velocities into vertical and East–West directions. The analysis of decomposed velocities shows an interesting velocity field in the coastal villages of Lido di Dante and Lido Adriano where subsidence rates up to 10 mm/yr and a dominant eastward displacement up to 3 mm/yr are well depicted. In this area, an offshore exploitation activity of natural gas takes place by a platform installed less than 2 km far from the coastline (see Figure 3.1 to locate the offshore site ANGA); the rates of ground deformation phenomena in the area have been recently reported by Polcari et al. (2022).

However, the consolidation processes outlined in this Chapter in such an area (up to $3 - 4$ mm/yr) cause an overestimation of the actual subsidence rates due to driving factors other than the consolidation processes themselves. Conversely, the horizontal displacements are not biased by the settlements occurred. The correlation of the horizontal displacement pattern and the offshore gas exploitation activity seems to be evident even though a similar pattern is visible in the industrial area located few km far in the north-western direction where the influence of gas withdrawal should be negligible. However, the industrial area is also subjected to vertical displacements up to -15 mm/yr over very well delimited sectors occupied by single industrial plants. Unfortunately, the available GIS data do not report the specific industrial activity in the attribute table and such kind of relationship cannot be established. A more detailed description of the industrial activities carried out in any single lot is therefore advised.

In the attempt to filter out the consolidation settlement from the subsidence rates, the use of GNSS as reference must also be addressed. Indeed, when GNSS stations are used to bring DInSAR velocities into a global reference frame, installation of GNSS monuments on recently settled area should be avoided. Otherwise, the contribution of consolidation processes triggered by the building load will be transferred to the totality of PSs selected by the multi-temporal interferometric processing. Ancillary subsidence data from topographic leveling could be a valid support in the interpretation of ground deformation. Leveling benchmarks are placed on roads and come from consolidated topographic network; for this reason, vertical displacements derived from leveling measurements are less sensitive to anthropogenic processes of consolidation even though their availability is very limited in most cases.

In the study area, an alternative source of subsidence could be related to groundwater pumping, since 1950s, for irrigation purposes from the multi-layered surficial aquifer (An-

tonellini et al. 2019). Data provided by ARPAe show a diffuse decrease of the groundwater table from 1990 to 2012 in the area of Ravenna (Antoncecchi et al. 2021). However, in the period of the present investigation, a substantial stability of the groundwater table is reported (A.R.P.A.E. 2020; Polcari et al. 2022).

3.3 Final remarks

The approach proposed in this Chapter allows to investigate and separate several contributions to subsidence phenomena over the municipality of Ravenna (Emilia Romagna, Italy). In particular, consolidation processes after construction were assessed by the use of GIS dataset of the built environment. In the present study, only few descriptive attributes related to the age of construction and intended uses were adopted in the classification of scatterers but many others are available and the relationship between rates and sources of subsidence could be further investigated.
In the presented results, it is shown that the subsidence phenomena could be strongly biased by consolidation processes or ascribed to a different causal factor with an overestimation of its contribution to ground deformation. In the study area, the consolidation processes seem to be active over areas settled in the last $20 - 30$ years with a component contributing to vertical rates up to 3 mm/yr, representing the 20% of the cumulative displacement reported for coastal villages where different sources of subsidence increase the vulnerability to coastal erosion. Therefore, such effects should be taken into consideration. For a better interpretation of the phenomena, more data about stratigraphy, construction modes and geotechnical factors should be incorporated in the GIS dataset. However, very often such information are not available at very local scale or partially available in a GIS format. Moreover, to increase the reliability of the proposed analysis, satellite data at higher spatial resolution could be employed in addition to the correction of the PS coordinates after residual topographic error estimation; it would improve the spatial linkage between scatterers and GIS information layers with a more reliable analysis of relationship between subsidence phenomena and causal factors.

Chapter 4

Multi-temporal interferometry for structural investigations

In this Chapter, the potentialities and performances of the multi-temporal satellite interferometric technique for structural investigations of single buildings are evaluated. In particular, an analytical procedure for the reconstruction of the 3D rigid motion of isolated buildings based on SAR measurements is proposed; to this aim, a dual-orbit SAR dataset is required. The proposed method is tested with numerical simulations and it is complemented by the estimation of the uncertainties related to the estimated motion parameters. Finally, the method is tested on a high-resolution COSMO-SkyMed dataset over the metropolitan area of city of Rome (Italy).

4.1 Introduction

The application of multi-temporal interferometric techniques at building or infrastructure scale is enabled by the advanced capabilities in terms of revisit time and high spatial resolution of the more recent generation of X-band SAR constellations (e.g., COSMO-SkyMed, TerraSAR-X/TanDEM-X). Indeed, the ability of the mentioned satellites and constellations to provide data with meter or even sub-meter spatial resolution allows measuring displacements of several points over a single structure with a millimetre accuracy and paved the way to successive analyses oriented to the structural monitoring based on satellite interferometric techniques.
In the last years, applications of satellite radar interferometry to the assessment of building structural damage induced by ground deformations and slope failure have been reported (Bianchini et al. 2015; Bru et al. 2013; Mazzanti and Cipriani 2011; Del Soldato et al. 2019; Noviello et al. 2020). Among the others, Cavalagli et al. (2019) presented an investigation on static monitoring of historical monuments complemented by in-situ measurements and Gernhardt and Bamler (2012) introduced the potentialities of meter-resolution SAR data in the deformation monitoring of single buildings. More recently Talledo et al. (2022) explored the potentialities and limitations of satellite data for structural assessment and monitoring and Di Carlo et al. (2021) investigated the use of multi-temporal DInSAR products and historical surveys data for buildings structural monitoring. In addition, some applications oriented to the monitoring of infrastructures have been also proposed in Zhu et al. (2018); Milillo et al. (2019); Jung et al. (2019).
However, several aspects related to the use of DInSAR techniques to monitor single

structures remain challenging. In particular, the reliability of structural monitoring based on radar satellite data needs to be carefully assessed due to the very small displacements characterizing potentially damaged structures. Moreover, the displacements of the targets obtained from multi-temporal interferometric techniques need to be combined to reconstruct the effective structural motion and the unavoidable displacement measurement and targets positioning uncertainties have to be taken into account. To fully exploit the redundancy of measurements at building scale, spatial and temporal resampling of the available PSs may be required (Talledo et al. 2022); however, standard interpolation procedures do not consider the uncertainties that may affect the PS positions and the displacement measurements.
The reconstruction of the global building displacement becomes more straightforward when the building can be considered as a rigid body; this is the case, for instance, of buildings suffering from foundation settlements that cause a rigid motion of the structure. However, also if the rigid motion hypothesis can be considered valid, a careful uncertainty analysis accounting for measurement and positioning errors is necessary to reliably reconstruct the 3D rigid motion of a building. As far as the author knows, a comprehensive analysis about the uncertainties affecting the multi-temporal DInSAR displacements and their propagation to the derived rigid motion of buildings is not available in the recent literature. To cover this gap, in this Chapter, a method for the evaluation of isolated buildings displacements from satellite SAR measurements along with an uncertainty analysis is proposed. The obtained results could inform about the minimal accuracy required to the DInSAR data (in terms of measures, positions and number of PSs) used in the structural analysis to detect a particular deformation phenomenon. Moreover, the proposed method aims at assessing displacements related to the rigid motion of buildings, generally caused by foundation settlements that can be due to structural weaknesses, underground water or gas extraction/injection activities and close presence of construction sites.
The developed model reconstructs the rigid motion components of a building starting from displacements detected by PSI technique along the LOS direction from a dual-orbit set of high resolution SAR data. Due to the limited sensitivity of the SAR measurements to displacements in North-South direction, the reconstruction of the original motion vector is limited to the three rotations and displacement components in East-West and vertical directions (Hanssen 2001; Gernhardt and Bamler 2012; Cavalagli et al. 2019). The uncertainties affecting the estimated motion parameters are evaluated from an analytical procedure based on the propagation of the uncertainties law applied to the developed model. The obtained analytical expression could be useful to evaluate the accuracy of the estimated rigid motion components on the basis of the number of potentially identified PSs, the building geometry and the satellite orbit inclinations, without knowing the exact positions of the PSs.

4.2 Assessment of the 3D rigid motion of buildings from multi-temporal interferometry

In this Section, the developed procedure for the estimation of the 3D rigid motion components is presented. It relies on the least square solution of the model built from the ascending and descending satellite measurement. Then, numerical simulations are performed to validate the model and assess the uncertainties affecting the motion components. Moreover, an analytical procedure for the estimation of the above mentioned uncertainties is proposed.

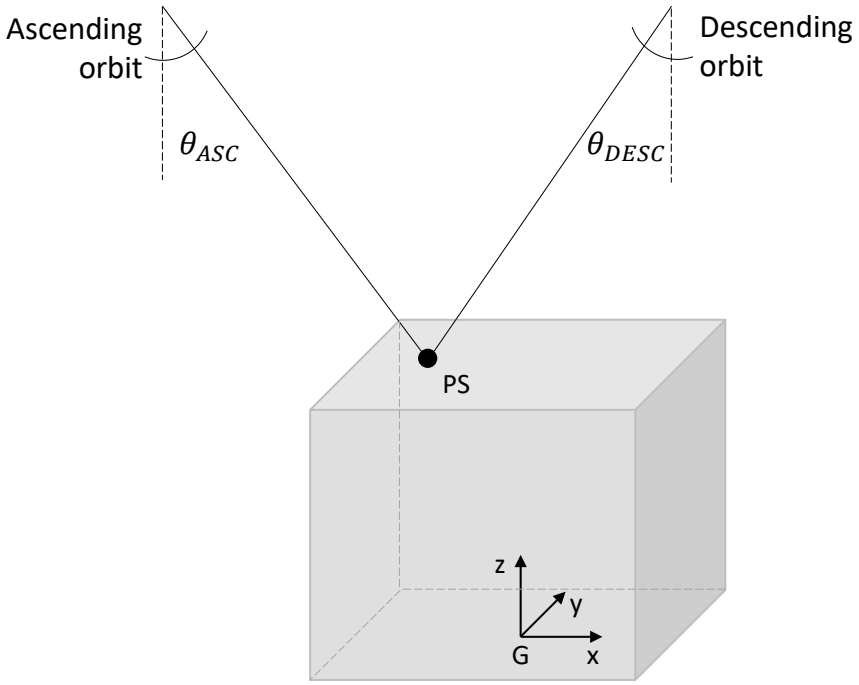

Figure 4.1: The considered reference system for the computation of the rigid motion parameters.

4.2.1 Evaluation of the 3D rigid motion

The developed procedure for the evaluation of the 3D rigid motion parameters of isolated buildings relies on the combination of ascending and descending satellite SAR measurements. The SAR data acquired from the two satellite acquisition geometries are temporally and spatially uncorrelated, meaning that displacements of PSs are measured at different acquisition times and in different positions. Thanks to the hypothesis of rigid motion, PS displacements measured from the ascending and descending orbit can be analysed together with no need for geometrical interpolation, i.e. it is not necessary that the PS measured from the two orbits are co-located. Also the temporal correlation is not required as the structural monitoring relies on mean annual displacement values. On the contrary, data measured from the two satellite geometries need to be properly realigned when investigating the building behaviour at a specific time.
Let us consider the reference system shown in Figure 4.1, where x, y and z represent, respectively, the East-West, North-South and vertical direction.

Assuming clockwise rotations as positive, the displacement of a generic point P relative to G, namely the point at the ground corresponding to the centre of gravity, can be expressed as

$$\begin{cases} v_{x,\mathrm{P}} = v_{x,\mathrm{G}} + \Phi_{y,\mathrm{G}}\, D_{z,\mathrm{P}} - \Phi_{z,\mathrm{G}}\, D_{y,\mathrm{P}} \\ v_{y,\mathrm{P}} = v_{y,\mathrm{G}} - \Phi_{x,\mathrm{G}}\, D_{z,\mathrm{P}} + \Phi_{z,\mathrm{G}}\, D_{x,\mathrm{P}} \\ v_{z,\mathrm{P}} = v_{z,\mathrm{G}} + \Phi_{x,\mathrm{G}}\, D_{y,\mathrm{P}} - \Phi_{y,\mathrm{G}}\, D_{x,\mathrm{P}} \end{cases} \tag{4.1}$$

in which $v_{x,\mathrm{G}}$, $v_{y,\mathrm{G}}$ and $v_{z,\mathrm{G}}$ are the displacements in the three directions, $\Phi_{x,\mathrm{G}}$, $\Phi_{y,\mathrm{G}}$ and $\Phi_{z,\mathrm{G}}$ are the rotation around the three axes and $D_{x,\mathrm{P}}$, $D_{y,\mathrm{P}}$ and $D_{z,\mathrm{P}}$ are the distances between P and G in x, y and z direction, respectively.
The displacement measured on the generic point P of the building along the LOS direction of the ascending and descending satellite orbit, i.e. $d_{a,P}$ and $d_{d,P}$, can be written as a function of the displacement components of the same point

$$\begin{cases} d_{a,P} = (-v_{x,\mathrm{P}} \cos\alpha_a + v_{y,\mathrm{P}} \sin\alpha_a) \sin\theta_a + v_{z,\mathrm{P}} \cos\theta_a \\ d_{d,P} = (-v_{x,\mathrm{P}} \cos\alpha_d + v_{y,\mathrm{P}} \sin\alpha_d) \sin\theta_d + v_{z,\mathrm{P}} \cos\theta_d \end{cases} \tag{4.2}$$

in which α_a and α_d are the heading angles of the satellite orbits and θ_a and θ_d are the incidence angles of the ascending and descending geometry, respectively (Figure 4.1). Typical values of the heading angles are such that $\sin\alpha$ and $\cos\alpha$ can be approximated to 0 and ± 1, respectively (in particular $\alpha_a = 350°$ and $\alpha_d = 190°$ for COSMO-SkyMed). In this case, Equation (4.2) becomes

$$\begin{cases} d_{a,P} = -v_{x,\mathrm{P}} \sin\theta_a + v_{z,\mathrm{P}} \cos\theta_a \\ d_{d,P} = v_{x,\mathrm{P}} \sin\theta_d + v_{z,\mathrm{P}} \cos\theta_d \end{cases} \tag{4.3}$$

It can be noted that the limited sensitivity of the SAR to displacements along the North-South direction (i.e., the y direction) allows for a reliable estimation of the rigid motion components related to the displacement along the vertical and East-West direction and the rotation around the axes (namely, $v_{x,\mathrm{G}}$, $v_{z,\mathrm{G}}$, $\Phi_{x,\mathrm{G}}$, $\Phi_{y,\mathrm{G}}$ and $\Phi_{z,\mathrm{G}}$).
Substituting the expression of $v_{x,\mathrm{P}}$ and $v_{z,\mathrm{P}}$ of Equation (4.1) into Equation (4.3), the following matrix expression holds

$$\begin{bmatrix} d_{a,\mathrm{P}} \\ d_{d,\mathrm{P}} \end{bmatrix} = \begin{bmatrix} -\sin\theta_a & \cos\theta_a & D_{y,\mathrm{P}} \cos\theta_a & (-D_{z,\mathrm{P}} \sin\theta_a - D_{x,\mathrm{P}} \cos\theta_a) & D_{y,\mathrm{P}} \sin\theta_a \\ \sin\theta_d & \cos\theta_d & D_{y,\mathrm{P}} \cos\theta_d & (D_{z,\mathrm{P}} \sin\theta_d - D_{x,\mathrm{P}} \cos\theta_d) & -D_{y,\mathrm{P}} \sin\theta_a \end{bmatrix} \begin{bmatrix} v_{x,\mathrm{G}} \\ v_{z,\mathrm{G}} \\ \Phi_{x,\mathrm{G}} \\ \Phi_{y,\mathrm{G}} \\ \Phi_{z,\mathrm{G}} \end{bmatrix} \tag{4.4}$$

The rigid motion components $v_{x,\mathrm{G}}$, $v_{z,\mathrm{G}}$, $\Phi_{x,\mathrm{G}}$, $\Phi_{y,\mathrm{G}}$ and $\Phi_{z,\mathrm{G}}$ can be determined only if enough displacement measurements are available. Considering N_S measurements, n for the ascending orbit and m for the descending orbit, Equation (4.4) becomes:

$$\begin{bmatrix} d_{a,1} \\ \vdots \\ d_{a,n} \\ d_{d,1} \\ \vdots \\ d_{d,m} \end{bmatrix} = \begin{bmatrix} -\sin\theta_a & \cos\theta_a & D_{ya,1} \cos\theta_a & (-D_{za,1} \sin\theta_a - D_{xa,1} \cos\theta_a) & D_{ya,1} \sin\theta_a \\ \vdots & \vdots & \vdots & \vdots & \vdots \\ -\sin\theta_a & \cos\theta_a & D_{ya,n} \cos\theta_a & (-D_{za,n} \sin\theta_a - D_{xa,n} \cos\theta_a) & D_{ya,n} \sin\theta_a \\ \sin\theta_d & \cos\theta_d & D_{yd,1} \cos\theta_d & (D_{zd,1} \sin\theta_d - D_{xd,1} \cos\theta_d) & -D_{yd,1} \sin\theta_a \\ \vdots & \vdots & \vdots & \vdots & \vdots \\ \sin\theta_d & \cos\theta_d & D_{yd,m} \cos\theta_d & (D_{zd,m} \sin\theta_d - D_{xd,m} \cos\theta_d) & -D_{yd,m} \sin\theta_a \end{bmatrix} \begin{bmatrix} v_{x,\mathrm{G}} \\ v_{z,\mathrm{G}} \\ \Phi_{x,\mathrm{G}} \\ \Phi_{y,\mathrm{G}} \\ \Phi_{z,\mathrm{G}} \end{bmatrix} \tag{4.5}$$

with $N_S = n + m$. $D_{xa,i}$, with $i = 1, ..n$, denotes the distance along the x direction between the i-th PS identified from the ascending orbit and G, while $D_{xd,j}$, with $j = 1, ..m$, is the distance between the j-th PS of the descending orbit and G. The same goes for the distances in y and z direction. It is important to note that the rigid motion hypothesis makes not necessary that targets from ascending and descending dataset are the same.
Equation (4.5) can be synthetically presented as

$$\mathbf{M} = \mathbf{S}\,\boldsymbol{\Theta} \tag{4.6}$$

in which

$$\mathbf{M} = \begin{bmatrix} d_{a,1} \\ \vdots \\ d_{a,n} \\ d_{d,1} \\ \vdots \\ d_{d,m} \end{bmatrix}; \quad \mathbf{\Theta} = \begin{bmatrix} v_{x,\mathrm{G}} \\ v_{z,\mathrm{G}} \\ \Phi_{x,\mathrm{G}} \\ \Phi_{y,\mathrm{G}} \\ \Phi_{z,\mathrm{G}} \end{bmatrix} \tag{4.7}$$

and

$$\mathbf{S} = \begin{bmatrix} -\sin\theta_a & \cos\theta_a & D_{y,1}\cos\theta_a & (-D_{z,1}\sin\theta_a - D_{x,1}\cos\theta_a) & D_{y,1}\sin\theta_a \\ \vdots & \vdots & \vdots & \vdots & \vdots \\ -\sin\theta_a & \cos\theta_a & D_{y,n}\cos\theta_a & (-D_{z,n}\sin\theta_a - D_{x,n}\cos\theta_a) & D_{y,n}\sin\theta_a \\ \sin\theta_d & \cos\theta_d & D_{y,1}\cos\theta_d & (D_{z,1}\sin\theta_d - D_{x,1}\cos\theta_d) & -D_{y,1}\sin\theta_a \\ \vdots & \vdots & \vdots & \vdots & \vdots \\ \sin\theta_d & \cos\theta_d & D_{y,m}\cos\theta_d & (D_{z,m}\sin\theta_d - D_{x,m}\cos\theta_d) & -D_{y,m}\sin\theta_a \end{bmatrix} \tag{4.8}$$

In Equations (4.7) and (4.8), $\mathbf{M}$ is the N_S-by-1 vector collecting the measured displacements, $\mathbf{\Theta}$ is the vector that contains the five motion parameters and $\mathbf{S}$ a N_S-by-5 matrix whose terms depend on the positions of the PS and the incidence angles of the two satellite acquisition geometries.
In order to compute the rigid motion parameters values that best approximate the available measurements, the number of observations N_S must be significantly higher than the unknown parameters, contained in the vector $\mathbf{\Theta}$. Optimal values of the motion parameters are estimated through the least square method by minimizing the difference between measured and modelled displacements as

$$\hat{\mathbf{\Theta}} = (\mathbf{S}^{\mathrm{T}}\mathbf{S})^{-1}\mathbf{S}^{\mathrm{T}}\mathbf{M} \tag{4.9}$$

To evaluate the relative displacement of the building with respect to the ground, the same procedure has to be applied with reference to the PS targets at the ground. The relative rigid motion of the building is then estimated as the difference between the rigid motion obtained from the PSs on the building and those at the ground, thus allowing to distinguish the displacement of the ground from that of the building. PSs on the building are distinguished from those of the ground thanks to their height that can be estimated according to Reale et al. (2011); Rebmeister et al. (2021); Crosetto et al. (2010).
The hypothesis of rigid motion needs to be verified; to this aim, different subsets of the N_S PSs belonging to the building are selected and the rigid motion components are evaluated for each subset according to Equation (4.9). A low variability of the rigid motion components identified from the different subsets proves the reliability of the assumption.

4.2.2 Numerical simulations

In this Section, the numerical analyses designed to evaluate the performances of the procedure outlined in Section 4.2.1 are presented; these analyses are based on

1. the imposition of the rigid motion to simulated building,

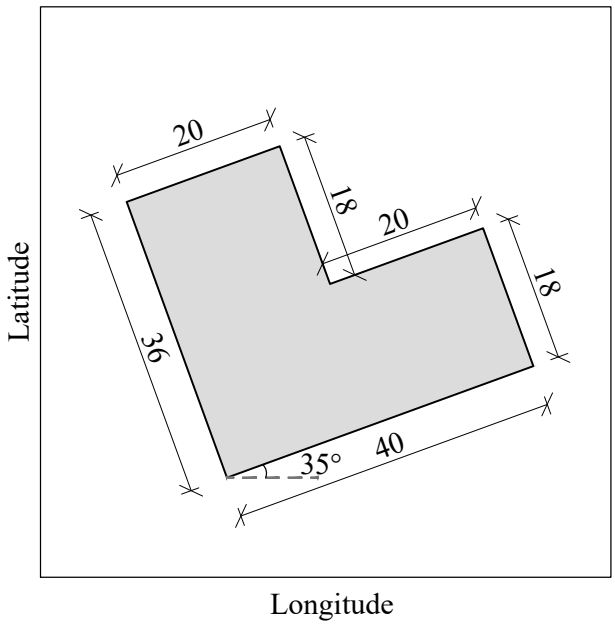

Figure 4.2: Plan view of the L-shaped building for the numerical simulations. Dimensions are in meters.

2. the simulation of the satellite measurements including measurement[1] and positioning uncertainties,

3. the evaluation of the rigid motion according to Section 4.2.1,

4. the comparison between imposed and estimated displacements,

5. the assessment of the variability of results.

The plan and dimensions of the building used for the numerical simulations is shown in Figure 4.2; it is a building with a L-shaped plan and a flat roof, inclined by 20° relative to East-West and 15 m high. The incidence angles of the two satellite orbits are assumed equal to 30° and 25° for the ascending and descending orbit, respectively.

The presented numerical analyses include also the simulation of the satellite measurements; therefore, the uncertainties affecting the SAR data have to be introduced. These uncertainties are related to inaccuracies in the PS displacement measurements and positioning. The latter are related to the position in plan of the PSs as it is assumed that the height of the building is known from a geometrical survey, and thus the PS vertical positions. For each simulation, the difference between the imposed motion parameters and the estimated ones allows to quantify the effect of the measurement and/or positioning uncertainties. Assuming to deal with COSMO-SkyMed data, which are particularly suitable for applications at infrastructure or building scale, the typical displacement rate accuracy $\overline{\sigma}_M$ is considered to be about 1 or 2 mm/yr (Casu et al. 2006; Crosetto et al. 2016). However, analyses with accuracy up to 5 mm/yr have been also performed in order to investigate its effect on the results.

As far as uncertainties in the PS positioning are concerned, these are related to the spatial resolution of the SAR images which does not allow for the knowledge of the exact position

[1]Note that the PS displacement along the LOS is not actually a measurement but it is obtained through PSI from SAR measurements. Nevertheless, throughout the paper, for the sake of simplicity, we use the term measurement uncertainties to indicate uncertainties related to the PS displacement along the LOS.

Table 4.1: Simulation parameters. n and m are the number of Persistent Scatterers for ascending and descending orbit, respectively; $\overline{\sigma}_M$ and $\overline{\sigma}_P$ are the measurement and positioning uncertainty, respectively.

Building shape	n	m	$\overline{\sigma}_M$ [mm/yr]	$\overline{\sigma}_P$ [m]	Grid cell [m]	Simulations number
L-shaped	60	40	1	0.9	3 × 3	3000

Table 4.2: Imposed simulation motion components and statistics of the estimated motion components. θ_{imp} are the values of the imposed motion components, $\mu(\theta_r)$ and $\sigma(\theta_r)$ are the mean value and standard deviation of the estimated motion components.

	Imposed parameters	**Simulation results**	
	θ_r	$\mu(\theta_r)$	$\sigma(\theta_r)$
$v_{x,G}$ [mm]	10.0	10.2	0.7
$v_{z,G}$ [mm]	50.0	50.0	0.3
$\Phi_{x,G}$ [mrad]	0.00	0.02	0.04
$\Phi_{y,G}$ [mrad]	2.00	1.99	0.02
$\Phi_{z,G}$ [mrad]	1.00	0.99	0.07

of the PS. CSK Stripmap HIMAGE data have a spatial resolution of 3 m both in range and azimuth. The investigated area could be therefore ideally divided into a grid of 3 m × 3 m and at most one PS can be identified in each grid cell. Indeed, there is no guarantee that a PS is measured in each grid cell. The main scatterer of a grid cell is located in a random position inside the grid cell. However, the exact location of the PS into the grid cell is not known in real applications and the measured displacement is assigned to the cell centre (i.e., the processed position in the following), thus introducing unavoidable uncertainties. The high number of performed numerical analyses allowed to statistically characterize the distance between the exact and the processed position of PS targets; this distance presents a distribution resembling a Gaussian distribution $\mathcal{N}(\mu = 0, \sigma^2 = 0.81)$. Therefore, the positioning uncertainty ($\overline{\sigma}_P$) is the square root of the variance (i.e., $\overline{\sigma}_P = 0.9$ m). Monte Carlo simulations are performed considering the contribution of both measurement and positioning uncertainties (i.e., $\overline{\sigma}_M$ and $\overline{\sigma}_P$, respectively).

Numerical simulations results The parameters of the numerical simulations and the imposed and obtained motion components are presented in Tables 4.1 and 4.2, respectively. Note that θ_r generally indicates the r-th motion parameter gathered in $\boldsymbol{\Theta}$.

Further simulations have been performed to evaluate the impact of the number of PSs and the measurement and positioning accuracy on the uncertainty of results. To this purpose, Figure 4.3a shows the trend of $\sigma(v_{z,G})$ for N_S between 14 and 200 (with $n = m = N_S/2$) and for different values of $\overline{\sigma}_M$, namely 0, 1, 2 and 5 mm/yr. In general, the estimated parameter uncertainty decreases when the number of PSs increases and when $\overline{\sigma}_M$ decreases (namely the displacement accuracy increases). Figure 4.3b presents the trends of $\sigma(v_{z,G})$ with increasing n and for different values of m, obtained with $\overline{\sigma}_M = 2$ mm/yr and accounting for both measurement and positioning uncertainties. Also in this case it is observed how an increase in the number of PSs implies a reduction of the estimated parameter uncertainty. Figure 4.3c represents the trends of $\sigma(v_{z,G})$ with respect to the number of detected PSs for increasing values of spatial resolution. It can be noted that the value of the uncertainty strongly decreases when the grid cell size decreases.

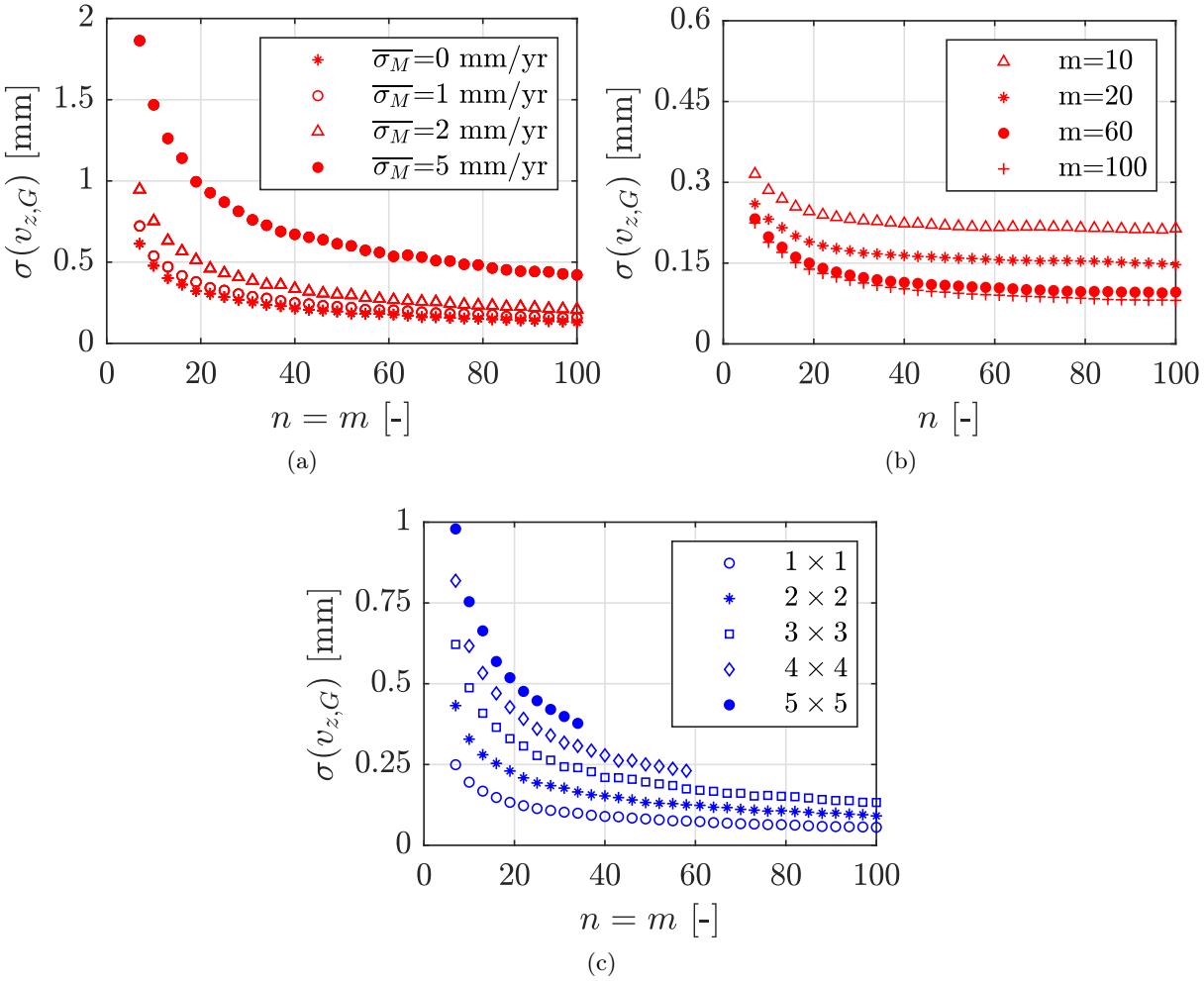

Figure 4.3: (a) Trends of $\sigma(v_{z,G})$ with increasing n for different values of $\overline{\sigma}_M$ obtained considering measurement and positioning uncertainties. The total number of PSs is $N_S = n + m$ with $n = m$. (b) Trends of $\sigma(v_{z,G})$ with increasing n for different values of m. (c) Trends of $\sigma(v_{z,G})$ with increasing n for different grid cell size.

Results presented in this section are mainly referred to the vertical displacements $v_{z,G}$. However, similar results were obtained considering also the other motion parameters, which allow drawing the same considerations.

4.2.3 Analytic motion parameters uncertainties

This Section presents an analytical procedure for the assessment of the uncertainties related to the motion components evaluated as described in Section 4.2.1. The proposed procedure has a general validity, thus, it can be applied for every building geometry as long as the rigid motion hypothesis is valid. Moreover, the analytical expressions presented in the following apply for PSs with the same height, e.g. in the case of PSs placed on a flat roof. The procedure can be further generalized to account for different PS heights at the expense of the expression simpleness.
The proposed approach could be adopted in real applications to evaluate the accuracy by which the motion components can be estimated depending on the number of potentially identified PSs on the analysed structure without the need of the a-priori knowledge of the effective positions of the targets. In fact, some conditions detailed in the following

allow removing the dependence of the estimated motion parameter uncertainties on the PS coordinates. Hence, a general expression of the estimated parameter uncertainty depending only on the number of PSs, the building geometry and the inclination with respect to the satellite orbits can be formulated. The influence of the simplifying conditions on the achieved results will be later discussed in this Section.

Starting from the least square solution for the vector $\boldsymbol{\Theta}$, Equation (4.9) can be rewritten as

$$\hat{\boldsymbol{\Theta}} = \mathbf{BM} \tag{4.10}$$

where

$$\mathbf{B} = (\mathbf{S}^T\mathbf{S})^{-1}\mathbf{S}^T \tag{4.11}$$

Therefore, assuming that measurement and positioning uncertainties are independent, the covariance of $\boldsymbol{\Theta}$ can be written exploiting the propagation uncertainty law as

$$\boldsymbol{\Sigma}(\boldsymbol{\Theta}) = \left(\frac{\partial \mathbf{B}}{\partial \mathbf{D}}\mathbf{M}\right)\boldsymbol{\Sigma}(\mathbf{D})\left(\frac{\partial \mathbf{B}}{\partial \mathbf{D}}\mathbf{M}\right)^T + \mathbf{B}\boldsymbol{\Sigma}(\mathbf{M})\mathbf{B}^T \tag{4.12}$$

where $\mathbf{D}$ is the vector collecting the position of each PS with respect to the centre of gravity and $\mathbf{M}$ is the vector of the measurements. Equation (4.12) can be rewritten in a compact form as the sum of two terms, the first ($\boldsymbol{\Sigma}_{\boldsymbol{P}}(\boldsymbol{\Theta})$) depending only on the positioning uncertainties and the second ($\boldsymbol{\Sigma}_{\boldsymbol{M}}(\boldsymbol{\Theta})$) only on the measurement uncertainties, as

$$\boldsymbol{\Sigma}(\boldsymbol{\Theta}) = \boldsymbol{\Sigma}_{\boldsymbol{P}}(\boldsymbol{\Theta}) + \boldsymbol{\Sigma}_{\boldsymbol{M}}(\boldsymbol{\Theta}) \tag{4.13}$$

noting that first term in the right hand side of Equation (4.12) is independent on the uncertainties affecting the measurements, whereas the second is independent on the positioning uncertainties.
Therefore, the total uncertainty of the r-th motion component can be evaluated from the main diagonal of $\boldsymbol{\Sigma}(\boldsymbol{\Theta})$ and is expressed by

$$\sigma_T(\theta_r) = \sqrt{\sigma_P^2(\theta_r) + \sigma_M^2(\theta_r)} \tag{4.14}$$

4.3 The application of the developed methodology

In this Section, the application of the procedure proposed in the previous Section to a case study in the metropolitan area of Rome (Italy) is presented.

4.3.1 Study area and dataset

The study area is located in the metropolitan area of the city of Rome (Figure 4.4); in particular, the focus is set to the Tevere valley characterized by recent (Pleistocene-Holocene) alluvial deposits composed of silty clays and lenses of sands with a nearly constant thickness of $20 - 25$ m (Funiciello and Amanti 1995; Milli 1997; Cavarretta et al. 2005; Funiciello and Giordano 2005; Raspa et al. 2008). The area and the relations between the geologic, geotechnical and hydrological characteristics and observed ground

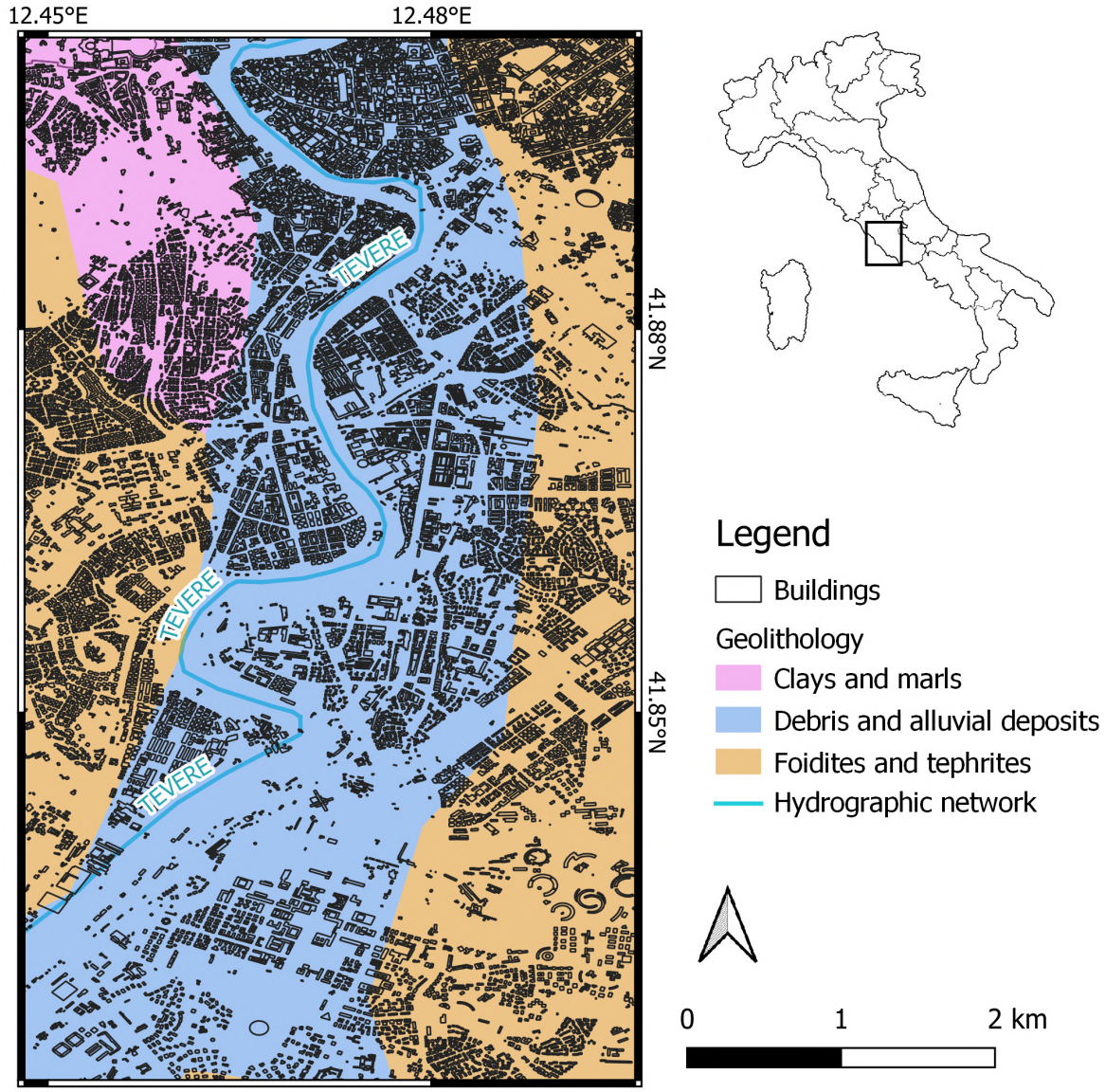

Figure 4.4: Map of the study area with the buildings dataset, the geolithology and the hydrographic network of the municipality of Rome (Italy).

displacement have already been investigated by Scifoni et al. (2016). In particular a dataset composed of ERS and ENVISAT data and spanning the period 1992 – 2010 has been processed with a SBAS approach. The resulting displacement maps show a predominance of stability in the metropolitan area (i.e., rates in the range $[-2, 2]$ mm/yr) and a long-term subsidence phenomenon in the areas nearer to the path of the river. The comparison with the geological setting enlightened a correlation between the presence of the alluvial deposit and the deformation pattern.
For the application presented in this Chapter, high resolution CSK Stripmap HIMAGE data[2] were processed according to the strategy reported in Section 1.3 of Chapter 1. For the removal of the topographic phase, the SRTM DEM with a resolution of 30 m has been employed. The details regarding the processed CSK dual-orbit set of data are reported in Table 4.3.

[2]This work was carried out using COSMO-SkyMed Products by the Italian Space Agency (ASI), delivered under a license to use by ASI in the framework of the ReLUIS-DPC 2019 – 2021 Project (Line WP6).

Table 4.3: The COSMO-SkyMed dataset over the city of Rome.

Orbit	Number of images	Master date	Start date	End date	θ
Ascending	135	22/03/2013	21/03/2011	30/03/2019	36.7°
Descending	70	17/12/2016	19/02/2011	29/12/2016	30.3°

Note: θ is the mean incidence angle in the study area.

For the application that is here discussed, the residual topographic error was estimated and the correction of the PS targets coordinated were corrected accordingly as described in Section 1.3.3. Moreover, as far as the GNSS calibration station is concerned, the velocities of the M0SE station (Latitude: 41.893°; Longitude: 12.493°) located in the city centre of Rome were used. In particular,

$$
\begin{aligned}
v_{\text{up}}^{\text{M0SE}} &= (-0.8 \pm 0.2)\,\text{mm/yr} \\
v_{\text{east}}^{\text{M0SE}} &= (-0.9 \pm 0.2)\,\text{mm/yr} \\
v_{\text{north}}^{\text{M0SE}} &= (1.7 \pm 0.5)\,\text{mm/yr}
\end{aligned}
$$

The GNSS velocities projected along the ascending and descending LOS directions with uncertainties (according to Equations (1.14) and (2.1)) are

$$
\begin{aligned}
v_{\text{LOS,asc}}^{\text{M0SE}} &= -0.3\,\text{mm/yr} \\
v_{\text{LOS,desc}}^{\text{M0SE}} &= -1.3\,\text{mm/yr}
\end{aligned}
$$

4.3.2 Results and discussions

The results of the elaboration are presented in Figure 4.5, in which the ascending descending LOS-oriented calibrated velocity maps are presented for the selected study area.

Within the study area, two building were selected as the case study to exemplify the developed procedure for the estimation of the 3D rigid motion parameters and the associated uncertainties. The selected buildings are those of Figure 4.6 (namely, building 1 and building 2) along with the PSs from both the ascending and descending set related to the buildings. PS belonging to the target buildings are selected with the aid of a database of the building location and shape. In order to guarantee that almost all of the PS of the buildings are included, a small buffer area outside the original building area is added (Zhu et al. 2018). The geometric characteristics of the selected buildings and the number of PSs belonging to them are listed in Table 4.4. It is worth noting that, due to the fact that the height of the buildings are known (and thus the heigh of the related PSs), the vertical positioning uncertainties can be neglected.

The two analysed buildings show a vertical displacement during the investigated period of almost 3 mm and horizontal displacements of about 0.6 mm and 1.3 mm for Building 2 and 1, respectively. Small rotations are observed with an order of 10^{-2} mrad (Table 4.5).

Furthermore, the hypothesis of rigid motion is verified as an example for Building 1. To this aim, 30 different subsets composed of 80 randomly selected PSs (40 from the ascending orbit and 40 from the descending orbit) are identified. For each subset, values of the rigid motion components and corresponding uncertainties are estimated. Mean values and standard deviations of the results obtained from the 30 analyses are reported

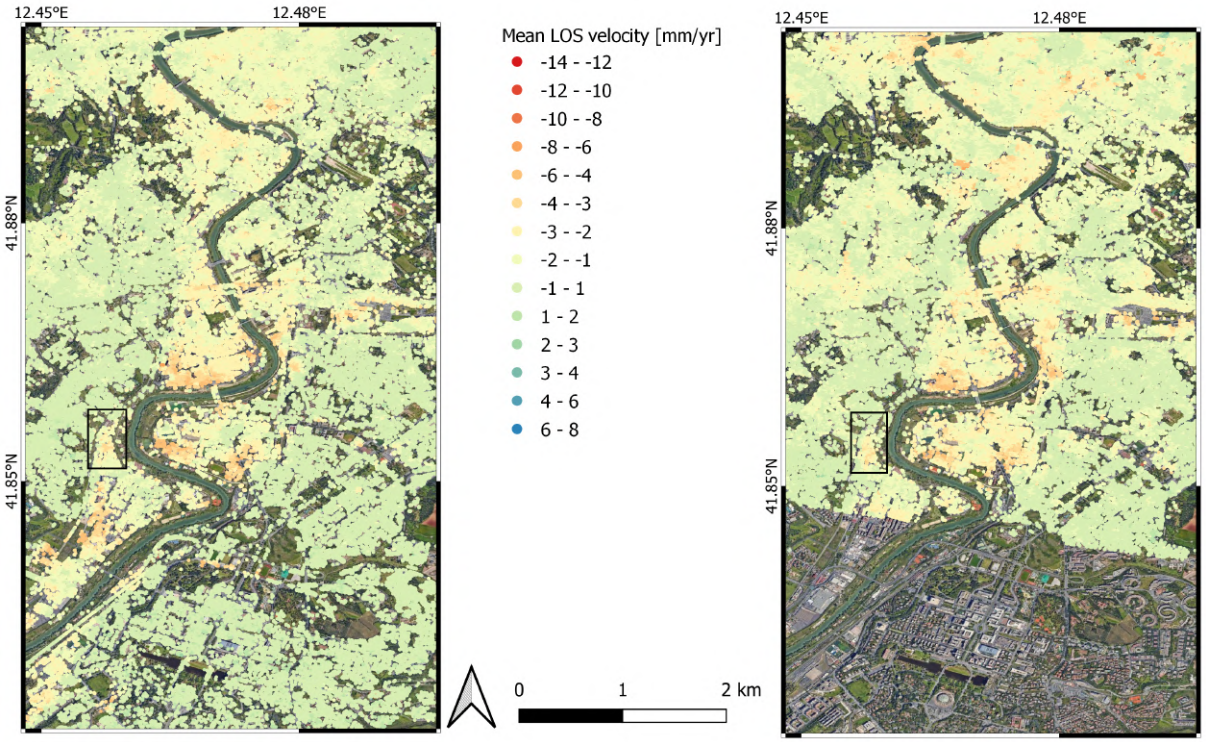

Figure 4.5: Ascending (left) and descending (right) slant oriented calibrated velocity maps (mm/yr) over the city of Rome (Italy). The area enclosed by the black rectangle identifies the area in which the buildings selected as the case studies are located.

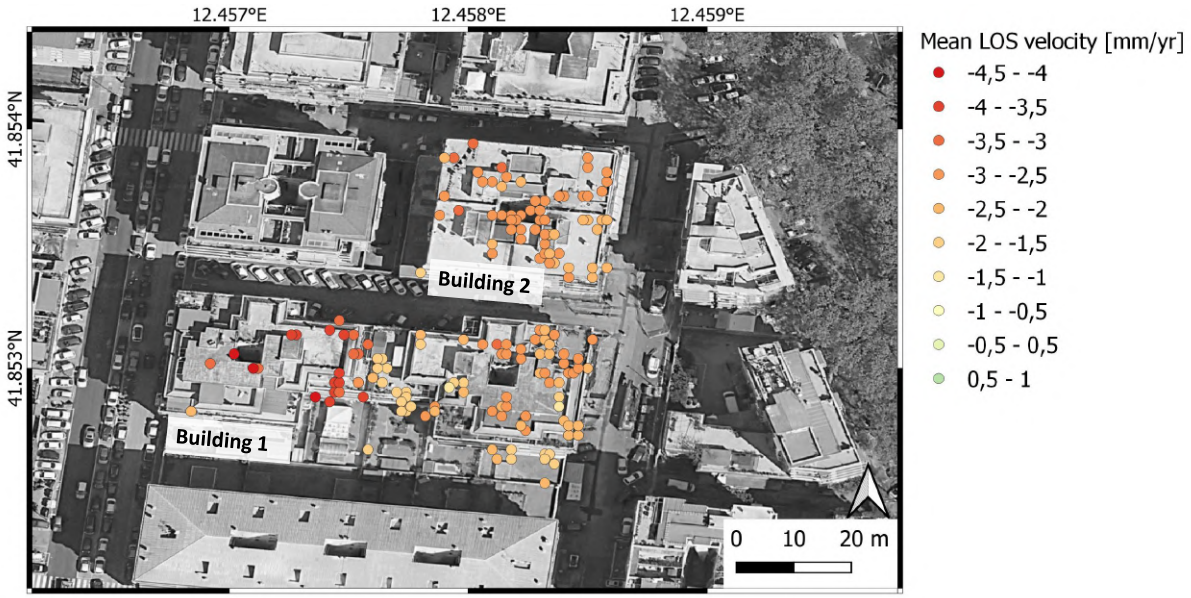

Figure 4.6: Ascending and descending slant oriented velocity maps for the selected buildings.

Table 4.4: Characteristics of the analysed buildings: number of PSs identified form the ascending (n) and descending (m) orbit, building dimensions (L and B) and building height (D_z).

		Building 1	**Building 2**
n		59	29
m		92	65
L	[m]	72.3	34.3
B	[m]	28.3	28.0
D_z	[m]	26.7	24.3

Table 4.5: The estimated motion components and the associated uncertainties accounting for both measurement and positioning uncertainties.

	Building 1		**Building 2**	
	$\theta_{r,\text{est}}$	$\sigma_T(\theta_r)$	$\theta_{r,\text{est}}$	$\sigma_T(\theta_r)$
$v_{x,G}$ [mm]	-1.3	0.2	-0.6	0.4
$v_{z,G}$ [mm]	-2.8	0.1	-2.8	1.1
$\Phi_{x,G}$ [mrad]	-0.02	0.01	-0.01	0.02
$\Phi_{y,G}$ [mrad]	-0.04	0.00	0.01	0.03
$\Phi_{z,G}$ [mrad]	-0.06	0.02	0.01	0.03

Table 4.6: Mean values and standard deviations of the estimated motion components and the uncertainties obtained accounting for both measurement and positioning uncertainties through 30 simulations performed for building 1.

	Building 1			
	$\theta_{r,\text{est}}$		$\sigma_T(\theta_r)$	
	μ	σ	μ	σ
$v_{x,G}$ [mm]	-1.2	0.1	0.3	0.0
$v_{z,G}$ [mm]	-2.8	0.1	0.2	0.0
$\Phi_{x,G}$ [mrad]	-0.02	0.00	0.02	0.00
$\Phi_{y,G}$ [mrad]	-0.05	0.00	0.01	0.00
$\Phi_{z,G}$ [mrad]	-0.06	0.01	0.03	0.00

in Table 4.6. Mean values of the estimated motion parameters resemble those obtained considering the full set of PSs and standard deviations are at least a order of magnitude smaller confirming the hypothesis of rigid motion.

The hypothesis of rigid motion is further validated by defining other subsets of PSs as follows rather than randomly. Each subset is composed of the PSs belonging to a specific portion of the building, namely $L_1 \times B$ where B is the smaller building dimension (namely 28.3 m) and L_1 varies from 6 m to 56 m with step size 3 m. Figure 4.7 shows the trends of the estimated motion parameters for increasing L_1. It can be observed that the estimated motion parameters show great uncertainty when L_1 is lower than 20 m, i.e. when a very few PSs are considered. On the contrary, they become quite stable for greater values of L_1 and, thus, for a greater number of targets

Discussions The results presented in this Section provide an insight on the capabilities and potentialities of multi-temporal interferometric techniques for structural investigation applications. It is important to highlight that the satellite interferometric techniques can

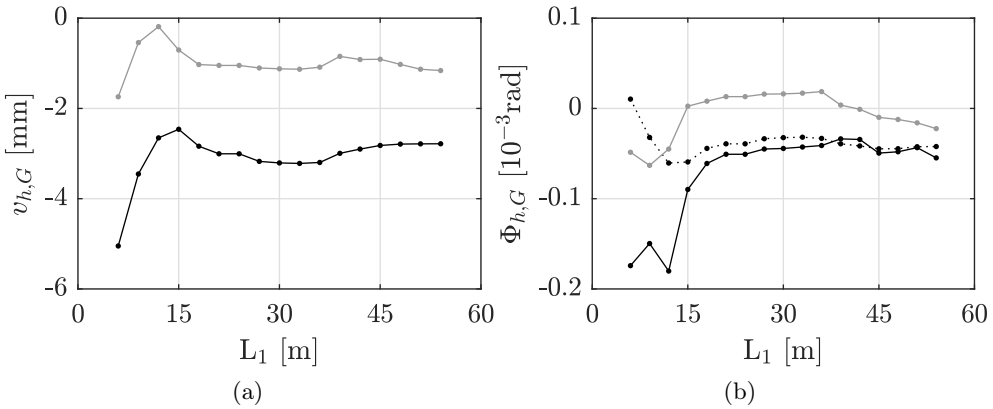

Figure 4.7: Trend of (a) $v_{z,G}$ (black), $v_{x,G}$ (grey), (b) $\Phi_{z,G}$ (black), $\Phi_{y,G}$ (dotted) and $\Phi_{x,G}$ (grey) for subsets of Persistent Scatterers identified on different portions of the building roof, namely L$_1$×B.

provide insights into the structural behaviour with reference to the past decade (i.e., from the launch of the first X-band SAR constellation); this means that the identification of displacements or rotations below the critical thresholds for buildings (e.g., 1 mrad for rotations) does not imply the absence of structural issues, as the contribution of previous displacements or rotations can not be evaluated. On the contrary, abnormal structural displacements over the recent years can be detected from SAR measurements, allowing for the design and installation of a specific in-situ monitoring system to investigate the damage evolution.

The developed model relies on a high number of PSI velocities from dual orbit SAR observation for the estimation of five rigid motion components of an isolated building. The use of all the available independent ascending and descending measures (i.e., the use of a number of observations significantly higher with respect of the number of the unknown parameters) improves the estimation of the motion components; moreover, the least square solution of the model ensures the computation of the parameters estimates that best fit the observations.

The performed numerical simulations were designed to take into account the uncertainties affecting both the measurements and the positioning of the targets evaluating these contributions from literature values and from a statistical analysis, respectively. The results of the simulations (i.e., the mean and the standard deviation of the parameters as computed from the simulations of Table 4.2) were compared to the imposed parameters and a general agreement between the values can be noted.

Some interesting considerations that could have a general validity regarding the impact of the simulation parameters on the results can be pointed out. In particular, from Figure 4.3, it can be noted that:

1. for increasing value of the measurement uncertainty and for decreasing number of targets, the uncertainty related to the estimated motion component increases (Figure 4.3a). In particular, the value of the uncertainty related to the vertical motion component drops under the threshold of 1 mm when at least 40 PSs over the structure are detected independently from the value of the measurement uncertainty;

2. the uncertainty related to the estimated motion component increases when the number of PSs decreases for a given value of the measurement uncertainty. Moreover, the uncertainty related to the vertical motion component value seems to reach a

stability when at least 40 PSs in one of the orbits are detected for the simulated building (Figure 4.3b);

3. the spatial resolution of the SAR data has a role in the estimation accuracy of the motion components. In particular, for higher resolution data the stability of the uncertainty value is reached even if few tenths of targets are detected over the structure. Moreover, for resolutions lower than 3 m $\times$ 3 m, the value of the uncertainty related to the vertical motion component is always lower than 0.5 mm and, when a very high number of PSs are detected, there is no advantage in using very high resolution data because the value of uncertainty always stands below 0.2 mm. It can be also noted the unsuitability of the medium resolution data (e.g., 5 m $\times$ 5 m) for structural investigations because of the low number of PSs identifiable over the structure and, thus, the poor achievable accuracy of the estimated motion components (Figure 4.3c).

The analytical expression for the parameter motion components uncertainties could be used in real applications to a priori evaluate the achievable accuracy without the need to exactly know the positions of the targets. This can be done when the number of PSs measured from the two acquisition geometries is sufficiently high and under the validity of the hypothesis of uniformly distributed PSs over the building roof. Moreover, the a posteriori uncertainties related to the motion component can be evaluated from the number of identified PSs, the acquisition geometries from both orbits and the analysed building geometry. The computed uncertainties values could inform on the accuracy by which the rigid motion components of a given building can be identified.
The procedure for the computation of the 3D rigid motion components of an isolated building with the uncertainties estimation has been tested with a real high resolution (3 m $\times$ 3 m) COSMO-SkyMed dataset. For both the analysed case studies, the estimated uncertainties are, in most cases, one order of magnitude smaller than the parameters to which they are related to.
Interesting considerations arise from the analyses performed to validate the rigid motion hypothesis. In particular, when a number of simulations is performed over subsets of PSs, the mean and variance of both the estimated parameters and the related uncertainties have been computed enlightening a substantial agreement between the analysis performed with the entire set of PSs and that performed with the selected subsets; thus, the stability of the achieved solution is demonstrated. Moreover, the analysis performed with an increasing number of PSs (Figure 4.7) shows that the stability of the parameters values (considering both displacement components and rotations) is reached when at least few tens of PSs are considered (corresponding to 20 m of length of Building 1 of Figure 4.7).
The achieved results can suggest that the proposed model is able to estimate displacement components of building along the vertical and East-West direction and rotations in the order of millimetres and tenths of milliradians with associated uncertainties in most cases smaller of one order of magnitude. Moreover, the analysis produce more reliable results when at least some tens of PS are considered (i.e., for building of some hundreds of squared meters for the resolution of the processed SAR data) and the accuracy increases with the number of PSs detected and analysed and when accurate measurements are considered. The use of higher resolution data is also advised to increase the accuracy of the analysis; to this aim, new constellations providing data at meter or sub-meter resolutions could be of interest for structural investigation applications.

4.4 Final remarks

In this Chapter, a procedure for the evaluation of the rigid motion components of isolated buildings from satellite SAR measurements has been proposed. In particular, the rigid motion components are reconstructed starting from LOS displacements from dual orbit set of high resolution data obtained by the developed PSI processing strategy. Moreover, numerical simulations have been carried out to validate the procedure and outline its performances. The proposed method is complemented by an analytical procedure relying on the error propagation law for the quantification of the uncertainties affecting the estimated motion parameters with the aim to evaluate the reliability of the identified structural motion. The main benefit of the proposed analytical expressions is that they can be adopted in real applications to a priori evaluate the accuracy by which the motion parameters can be identified depending only on the number of potentially identified PSs, the building geometry and the satellite orbit inclinations, with no need to know the exact positions of the PSs (Bassoli et al. 2023).
The method has been applied to two buildings case study in the metropolitan area of Rome (Italy) for which a dual orbit set of COSMO-SkyMed data has been processed. The presented results for the selected buildings show that structural displacements and rotations of the order of some tenths of mm/yr and mrad/yr respectively can be recognized. The accuracies of the identified displacements and rotations depend on their entity and increase with the PS numerosity and, in general, they are one order of magnitude smaller with respect to the parameters to which they are related to.
The proposed procedure can be generalized to automatically investigate the behaviour of wide urbanized areas, neighbourhoods or districts aiming at monitoring the built heritage on a large scale. Furthermore, in the proposed method, it is assumed that the building height is known from a simple geometrical survey and thus the targets heights. In the case of an automatic application on a large scale, a geometrical survey is not feasible and a valid alternative could be the use of a GIS dataset; however, only a limited number of municipalities in Italy makes available rich dataset regarding the built heritage. When the geometry of the buildings can not retrieved, the scatterer heights should be evaluated through PSI techniques. If so, a further uncertainty contribution related to the uncertainty in the PS height should be added to the positioning uncertainty that has been already discussed.

Discussions and conclusion

In this thesis, methods and approaches for the analyses of PSI-based data have been proposed with the aim to investigate the potentialities of interferometric products to provide valuable information in the interpretation of the phenomena occurring at the Earth surface. The focus has been set to the assessment of the accuracies related to the performed analyses to provide results with the associated uncertainties.
The main contributions of this dissertation are summarised in the following along with some discussions. First, a free and open source PSI processing strategy based on the use of the software SNAP, StaMPS and TRAIN has been proposed. Moreover, the processing of dual-orbit set of SAR data has been complemented by: a) a procedure for the calibration of PSI-products performed with velocities from GNSS observations, b) the correction of the Persistent Scatterers coordinates after the computation of the phase contribution due to the residual topography and c) the decomposition of the LOS velocities to retrieve the vertical and East-West oriented velocity field. The processing strategy and the procedures outlined above where tailored and tested to medium and high resolution SAR data from the Sentinel-1 and COSMO-SkyMed satellites, respectively. Then, a procedure based on the error propagation law for the estimation of the uncertainties associated to the vertical and East-West components of the mean PS velocities has been proposed; in particular, the expression of the variance-covariance matrix associated to the decomposed velocities has been derived and the validation of the SAR decomposed results, performed at relevant sites, has been carried out with velocities from GNSS observations. The PSI open-source processing of ascending and descending SAR data applied to a dual-orbit set of Sentinel-1 data over the eastern sector of the Po Plain has proven its ability to provide PS time series that can depict linear trends and periodical signatures along the slant direction with a points dispersion of few mm, with no further filtering procedures. The processing has been complemented by the calibration, decomposition, uncertainty estimation and validation performed with the use of contemporary GNSS observations. The mentioned procedures allowed to investigate and delineate the ground deformation phenomena occurring in the area and to provide differences between decomposed SAR and GNSS annual rates of 2 mm/yr in worst cases with uncertainties at mm/yr.
Following the rationale of this dissertation, i.e., the need to generate valuable information from the SAR data for the interpretation of phenomena, PSI-based and GIS dataset were combined and analysed to investigate and separate ground deformation contributions. In particular, the relationship between displacements occurring over built environment and consolidation processes has been investigated from a dual-orbit Sentinel-1 SAR dataset and descriptive attributes, related to the age of construction and intended use, over the municipality of Ravenna (Emilia Romagna, Italy). This has allowed to demonstrate that

investigations on subsidence phenomena by multi-temporal DInSAR could be strongly biased by consolidation processes or other processes ascribed to different causal factors causing an overestimation of its contribution to ground deformation. Moreover, the results have shown that the consolidation processes could last $20-30$ years after the construction, with a component contributing to vertical rates up to 3 mm/yr, representing the 20% of the cumulative displacement reported for the coastal villages of the study area. The main limitations affecting the described approach are related to: a) the poor GIS dataset in terms of descriptive attributes related to the building intended use, construction modes and geotechnical factors and the lack of information regarding the stratigraphy, b) the unsuitability of the Sentinel-1 IW data to perform an analysis at building scale.
As far as the former issue is concerned, a richer dataset and more data about stratigraphy, geology and hydrogeology should be incorporated for a better interpretation of the phenomena; however, such information are not usually available in a GIS format at very local scale. The interpretation of the effects of consolidations processes over different study areas characterized by different stratigraphic or geological setting would greatly benefit from improvements in the GIS dataset related to parameters from the geotechnic and structural engineering domains, such as the building dimensions and weight and the type of foundation. Concerning the latter, the reliability of the performed GIS analysis regarding the relationship between subsidence phenomena and causal factors would be improved by the exploitation of higher spatial resolution SAR data and a more accurate positioning of the targets; in fact, these solutions would enhance the spatial linkage between scatterers and GIS information layers.
The COSMO-SkyMed data, with a spatial resolution of 3 m $\times$ 3 m, were indeed employed to investigate the potentialities of multi-temporal interferometry for structural applications performed at the scale of a single building. To this aim, a model relying on a high number of PSI velocities from dual orbit SAR observation has been proposed to estimate the rigid motion components of an isolated building. The proposed method has been complemented by the assessment of the accuracies associated to the estimated motion components performed both through numerical simulations and analytic expressions taking into account the uncertainties affecting the displacement and the positioning of the targets. From the performed numerical simulations and the application of the proposed method to COSMO-SkyMed data over the metropolitan area of Rome (Italy), some interesting considerations regarding the relations between achieved accuracies and the dataset parameters can be pointed out. In particular, the uncertainty related to the estimated motion components increases for increasing value of the measurement uncertainty and decreasing number of detected Persistent Scatterers. Moreover, the accuracies values benefit from higher spatial resolution of the SAR data and the unsuitability of the medium resolution data for structural investigations is demonstrated due to the poor achievable accuracy of the estimated motion components. The developed analytical expression could be used to: a) a posteriori assign, as previously mentioned, the accuracy level related to the motion component from the number of identified PSs, the acquisition geometries from both orbits and the analysed building geometry and b) a priori evaluate the achievable accuracy without the need to exactly know the positions of the targets when certain specific conditions apply.
The achieved results suggest that displacement components of building along the vertical and East-West direction and rotations in the order of millimetres and tenths of milliradians, respectively, with associated uncertainties in most cases smaller of one order of magnitude can be estimated by the developed model. Moreover, the estimation of the motion components is improved by the use of a number of observations significantly higher

with respect to the number of the unknown parameters.
The procedure could be useful to automatically investigate the behaviour of wide urbanized areas with the aim to monitor the built heritage on a large scale; to this aim, the use of a GIS dataset with geometric and geotechnical information regarding the buildings is advised. However, as previously recalled, to find a rich dataset regarding the built heritage is not a trivial task. When the GIS dataset can not be found, the geometric information, and in particular the heights of the scatterers, have to be retrieved from the processing of SAR data; in this case, to increase the reliability of the analysis and to maximize the number of targets associated to the investigated building, data from new X-band satellites with a meter or sub-meter spatial resolution are advised along with the assessment of the uncertainty related to the vertical positioning of the targets.

Future developments of the research activity The integration between PSI-based and GIS dataset, related to both the structures and the environment, is a relevant aspect in the interpretation of the phenomena and the way they influence the built heritage. For this reason, further studies will be devoted to the use of richer GIS dataset and spatial analyses for a better delineation of the relationship between causal phenomena and their effects.
A second development of my research activity concerns the application of the devised method for an automatic and large scale investigation of structural and infrastructural criticalities. To this aim, high resolution SAR data with an accurate 3D positioning of the targets need to be used. This will allow to perform a preliminary identification of potential criticalities affecting structures and infrastructures with the aim to set up an integrated monitoring system, based on PSI results and data from traditional sensors and techniques, where issues are detected.

Bibliography

Abidin H, Andreas H, Gumilar I, Fukuda Y, Pohan Y, Deguchi T. 2011. Land subsidence of Jakarta (Indonesia) and its relation with urban development. Nat Hazards. 59:1753–1771.

Altamimi Z, Rebischung P, Métivier L, Collilieux X. 2016. ITRF2014: A new release of the International Terrestrial Reference Frame modeling nonlinear station motions. J Geophys Res-Earth. 121(8):6109–6131.

Antoncecchi I, Ciccone F, Rossi G, Agate G, Colucci F, Moia F, Petracchini L. 2021. Soil deformation analysis through fluid-dynamic modelling and DInSAR measurements: A focus on groundwater withdrawal in the Ravenna area (Italy. Bollettino di Geofisica Teorica ed Applicata. 62(2).

Antonellini M, Giambastiani B, Greggio N, Bonzi L, Calabrese L, Luciani P, Perini L, Severi P. 2019. Processes governing natural land subsidence in the shallow coastal aquifer of the Ravenna coast, Italy. Catena. 172:76–86.

ARPAE. 2018. Rilievo della subsidenza nella pianura emiliano-romagnola, seconda fase, relazione finale.

ARPAE. 2020. Valutazione dello stato delle acque sotterranee 2014-2019.

ASI. 2019. Cosmo-skymed mission and products description. Italian Space Agency; 3rd ed.

ASI. 2021. Cosmo-skymed seconda generazione: System and products description. Italian Space Agency.

Baldi P, Casula G, Cenni N, Loddo F, Pesci A. 2009. GPS-based monitoring of land subsidence in the Po Plain (northern Italy. Earth Planet Sci Lett. 288,1–2:204–212.

Baldi P, Casula G, Cenni N, Loddo F, Pesci A, Bacchetti M. 2011. Vertical and horizontal crustal movements in central and northern Italy. Boll Soc Geol It. 52(4):667–685.

Barra A, Reyes-Carmona C, Herrera G, Galve JP, Solari L, Mateos RM, Azañón JM, Béjar-Pizarro M, López-Vinielles J, Palamà R, et al. 2022. From satellite interferometry displacements to potential damage maps: A tool for risk reduction and urban planning. Remote Sensing of Environment. 282:113294.

Basilic R, Kastelic V, Demircioglu M, Garcia Moreno D, Nemser E, Petricca P, Sboras S, Besana-Ostman G, Cabral J, Camelbeeck T, et al. 2013. The european database of seismogenic faults (edsf) compiled in the framework of the project share.

Bassoli E, Grassi F, Varzaneh GE, Ponsi F, Mancini F, Vincenzi L. 2023. A simplified procedure to assess uncertainties in the estimation of the rigid motion of isolated buildings based on insar monitoring. Procedia Structural Integrity. 44:1554–1561.

Bekaert D, Hooper A, Wright T. 2015a. A spatially variable power law tropospheric correction technique for InSAR data. J Geophys Res-Earth. 120(2):1345–1356.

Bekaert D, Walters R, Wright T, Hooper A, Parker D. 2015b. Statistical comparison of InSAR tropospheric correction techniques. Remote Sens Environ. 170:40–47.

Berardino P, Fornaro G, Lanari R, Sansosti E. 2002. A new algorithm for surface deformation monitoring based on small baseline differential SAR interferograms. IEEE Transactions on Geoscience and Remote Sensing. 40(11):2375–2383.

Bert MK. 2006. Radar interferometry: persistent scatterers technique. The Netherlands: Springer.

Bertoni W, Brighenti G, Gambolati G, Ricceri G, Vuillermin F. 1995. Land subsidence due to gas production in the on-and offshore natural gas fields of the Ravenna area, Italy. In: IAHS Publications-Series of Proceedings and Reports-Intern Assoc Hydrological Sciences; vol. 234. p. 13–20.

Bianchini S, Pratesi F, Nolesini T, Casagli N. 2015. Building deformation assessment by means of persistent scatterer interferometry analysis on a landslide-affected area: The Volterra (Italy) case study. Remote Sensing. 7(4):4678–4701. Available from: https://www.mdpi.com/2072-4292/7/4/4678.

Bitelli G, Bonsignore F, Del Conte S, Franci F, Lambertini A, Novali F, Severi P, Vittuari L. 2020. Updating the subsidence map of Emilia-Romagna region (Italy. In: By Integration of SAR Interferometry and GNSS Time Series: The 2011–2016 Period. Proc. IAHS; vol. 382. p. 39–44.

Bitelli G, Bonsignore F, Pellegrino I, Vittuari L. 2015. Evolution of the techniques for subsidence monitoring at regional scale: the case of Emilia-Romagna region (Italy. In: Proc. IAHS; vol. 372. p. 315.

Boehm J, Niell A, Tregoning P, Schuh H. 2006. Global mapping function (GMF): A new empirical mapping function based on numerical weather model data. Geophys Res Lett. 33:07304.

Bonetti J, Del Bianco F, Schippa L, Polonia A, Stanghellini G, Cenni N, Draghetti S, F M, Gasperini L. 2022. Anatomy of Anthropically Controlled Natural Lagoons through Geophysical, Geological, and Remote Sensing Observations: The Valli Di Comacchio (NE Italy) Case Study. Remote Sensing. 14(4):987.

Bru G, Herrera G, Tomás R, Duro J, la Vega RD, Mulas J. 2013. Control of deformation of buildings affected by subsidence using persistent scatterer interferometry. Structure and Infrastructure Engineering. 9(2):188–200. Available from: https://doi.org/10.1080/15732479.2010.519710.

Bui LK, Le PV, Dao PD, Long NQ, Pham HV, Tran HH, Xie L. 2021. Recent land deformation detected by sentinel-1a insar data (2016–2020) over hanoi, vietnam, and the relationship with groundwater level change. GIScience & Remote Sensing. 58(2):161–179.

Bürgmann R, Rosen P, Fielding E. 2000. Synthetic aperture radar interferometry to measure Earth's surface topography and its deformation. Annu Rev Earth Pl Sc. 28(1):169–209.

Campo B, Amorosi A, Vaiani S. 2017. Sequence stratigraphy and late Quaternary paleoenvironmental evolution of the Northern Adriatic coastal plain (Italy. Palaeogeography, Palaeoclimatology, Palaeoecology. 466:265–278.

Carannante S, Argnani A, Massa M, D'Alema E, Lovati S, Moretti M, Cattaneo M, Augliera P. 2015. Earthquakes: New seismotectonic implications from subsurface geology and high-quality hypocenter location. Tectonophysics. 655:107–123.

Carminati E, Doglioni C, Scrocca D. 2003a. Apennines subduction-related subsidence of Venice (Italy. Geophys Res Lett. 30:50–51.

Carminati E, Martinelli G. 2002. Subsidence rates in the po plain, northern Italy: The relative impact of natural and anthropogenic causation. Eng Geol. 66(3-4):241–255.

Carminati E, Martinelli G, Severi P. 2003b. Influence of glacial cycles and tectonics on natural subsidence in the Po (Northern Italy): Insights from 14C age. Geochem Geophys Geosyst. 4(10).

Casu F, Manzo M, Lanari R. 2006. A quantitative assessment of the sbas algorithm performance for surface deformation retrieval from dinsar data. Remote Sensing of Environment. 102(3-4):195–210.

Cavalagli N, Kita A, Falco S, Trillo F, Costantini M, Ubertini F. 2019. Satellite radar interferometry and in-situ measurements for static monitoring of historical monuments: The case of Gubbio, Italy. Remote Sensing of Environment. 235:111453. Available from: `https://www.sciencedirect.com/science/article/pii/S0034425719304729`.

Cavarretta G, Cavinato G, Mancini M, Moscatelli M, Patera A, Stigliano F, Vallone R, Milli S, Garbin F, Storoni S. 2005. Geological and geotechnical modelling of the city of rome. In: Proceedings of GEOITALIA 2005—V Forum Italiano di Scienze della Terra. p. 23–24.

Cenni N, Mantovani E, Baldi P, Viti M. 2012. Present kinematics of central and northern Italy from continuous GPS measurements. J Geodyn. 58:62–72.

Cenni N, Viti M, Baldi P, Mantovani E, Bacchetti M, Vannucchi A. 2013. Present vertical movements in central and northern Italy from GPS data: Possible role of natural and anthropogenic causes. J Geodyn. 71:74–85.

Cerenzia I, Putero D, Bonsignore F, Galassi G, Olivieri M, Spada G. 2016. Historical and recent sea level rise and land subsidence in Marina di Ravenna, northern Italy. Ann Geophys. 59(5):0546.

Chen B, Gong H, Li X, Lei K, Ke Y, Duan G, Zhou C. 2015. Spatial correlation between land subsidence and urbanization in Beijing, China. Nat Hazards. 75:2637–2652.

Chen CW, Zebker HA. 2000. Network approaches to two-dimensional phase unwrapping: Intractability and two new algorithms. JOSA A. 17(3):401–414.

Chen CW, Zebker HA. 2001. Two-dimensional phase unwrapping with use of statistical models for cost functions in nonlinear optimization. JOSA A. 18(2):338–351.

Chen CW, Zebker HA. 2002. Phase unwrapping for large SAR interferograms: Statistical segmentation and generalized network models. IEEE Transactions on Geoscience and Remote Sensing. 40(8):1709–1719.

Chen WF, Liew JR. 2002. The civil engineering handbook. Crc Press.

Cian F, Blasco J, Carrera L. 2019. Sentinel-1 for monitoring land subsidence of coastal cities in Africa using PSInSAR: A methodology based on the integration of SNAP and StaMPS. Geosci J. 9:124.

Costantini M, Falco S, Malvarosa F, Minati F. 2008. A new method for identification and analysis of persistent scatterers in series of sar images. In: IGARSS 2008-2008 IEEE International Geoscience and Remote Sensing Symposium; vol. 2. IEEE. p. II–449.

Crosetto M, Biescas E, Duro J, Closa J, Arnaud A. 2008. Generation of advanced ers and envisat interferometric sar products using the stable point network technique. Photogrammetric Engineering & Remote Sensing. 74(4):443–450.

Crosetto M, Monserrat O, Cuevas-González M, Devanthéry N, Crippa B. 2016. Persistent scatterer interferometry: A review. ISPRS Journal of Photogrammetry and Remote Sensing. 115:78–89.

Crosetto M, Monserrat O, Iglésias R, Crippa B. 2010. Persistent scatterer interferometry: Potential, limits and initial C- and X-band comparison. Photogrammetric Engineering and Remote Sensing. 76:1061–1069.

Curlander JC, McDonough RN. 1991. Synthetic aperture radar. vol. 396. John Wiley & Sons New York, NY, USA.

Dang V, Doubre C, Weber C, Gourmelen N, Masson F. 2014. Recent land subsidence caused by the rapid urban development in the Hanoi region (Vietnam) using ALOS InSAR data. Nat Hazards Earth Syst Sci. 14:657–674.

De Zan F, Monti Guarnieri A. 2006. TOPSAR: Terrain Observation by Progressive Scans. IEEE Transactions on Geoscience and Remote Sensing. 44(9):2352–2360.

Del Soldato M, Farolfi G, Rosi A, Raspini F, Casagli N. 2018. Subsidence evolution of the Firenze–Prato–Pistoia plain (central Italy) combining PSI and GNSS data. Remote Sens-Basel. 10(7):1146.

Del Soldato M, Solari L, Poggi F, Raspini F, Tomás R, Fanti R, Casagli N. 2019. Landslide-induced damage probability estimation coupling InSAR and field survey data by fragility curves. Remote Sensing. 11(12). Available from: `https://www.mdpi.com/2072-4292/11/12/1486`.

Delgado Blasco JM, Foumelis M, Stewart C, Hooper A. 2019. Measuring Urban Subsidence in the Rome Metropolitan Area (Italy) with Sentinel-1 SNAP-StaMPS Persistent Scatterer Interferometry. Remote Sensing. 11(2):129.

Devanthéry N, Crosetto M, Monserrat O, Cuevas-González M, Crippa B. 2018. Deformation monitoring using Sentinel-1 SAR data. In: Multidisciplinary Digital Publishing Institute Proceedings; vol. 2. p. 344.

Di Carlo F, Miano A, Giannetti I, Mele A, Bonano M, Lanari R, Meda A, Prota A. 2021. On the integration of multi-temporal synthetic aperture radar interferometry products and historical surveys data for buildings structural monitoring. Journal of Civil Structural Health Monitoring. 11:1429–1447.

Farolfi G, Bianchini S, Casagli N. 2019a. Integration of gnss and satellite insar data: Derivation of fine-scale vertical surface motion maps of po plain, northern apennines, and southern alps, italy. IEEE Trans Geosci Remote Sens. 57(1):319–328.

Farolfi G, Piombino A, Catani F. 2019b. Fusion of GNSS and satellite radar interferometry: determination of 3D fine-scale map of present-day surface displacements in Italy as expressions of geodynamic processes. Remote Sens-Basel. 11(4):394.

Ferretti A, Fumagalli A, Novali F, Prati C, Rocca F, Rucci A. 2011. A new algorithm for processing interferometric data-stacks: SqueeSAR. IEEE T Geosci Remote. 49(9):3460–3470.

Ferretti A, Prati C, Rocca F. 2000. Nonlinear subsidence rate estimation using permanent scatterers in differential SAR interferometry. IEEE T Geosci Remote. 38(5):2202–2212.

Ferretti A, Prati C, Rocca F. 2001. Permanent scatterers in SAR interferometry. IEEE Transactions on geoscience and remote sensing. 39(1):8–20.

Fiaschi S, Tessitore S, Bonì R, Martire D, Achilli V, Borgstrom S, Ibrahim A, Floris M, Meisina C, Ramondini M, et al. 2017. From ERS-1/2 to Sentinel-1: Two decades of subsidence monitored through A-DInSAR techniques in the Ravenna area (Italy. GIScience & Remote Sensing. 54(3):305–328,.

Foumelis M, Delgado Blasco JM, Desnos YL, Engdahl M, Fernandez D, Veci L, Lu J, Wong C. 2018. Esa Snap - Stamps Integrated Processing for Sentinel-1 Persistent Scatterer Interferometry. In: IGARSS 2018 - 2018 IEEE International Geoscience and Remote Sensing Symposium; Jul. p. 1364–1367.

Funiciello R, Amanti M. 1995. La geologia di roma: il centro storico. vol. 50. Ist. Poligrafico dello Stato.

Funiciello R, Giordano G. 2005. Carta geologica del comune di roma, vol. 1. CDROM Università di Roma TRE-Comune di Roma-DDS Apat.

Gabriel AK, Goldstein RM, Zebker HA. 1989. Mapping small elevation changes over large areas: Differential radar interferometry. Journal of Geophysical Research: Solid Earth. 94(B7):9183–9191. Available from: https://agupubs.onlinelibrary.wiley.com/doi/abs/10.1029/JB094iB07p09183.

Gambolati G, Teatini P. 1998. Numerical analysis of land subsidence due to natural compaction of the Upper Adriatic Sea basin. In: CENAS. Dordrecht: Springer; p. 103–131.

Gernhardt S, Bamler R. 2012. Deformation monitoring of single buildings using meter-resolution sar data in psi. ISPRS Journal of Photogrammetry and Remote Sensing. 73:68–79. Innovative Applications of SAR Interferometry from modern Satellite Sensors; Available from: https://www.sciencedirect.com/science/article/pii/S0924271612001232.

Geudtner D, Torres R, Snoeij P, Davidson M, Rommen B. 2014. Sentinel-1 system capabilities and applications. In: Geoscience and Remote Sensing Symposium (IGARSS), 2014 IEEE International. IEEE. p. 1457–1460.

Grassi F, Mancini F, Bassoli E, Vincenzi L. 2022. Contribution of anthropogenic consolidation processes to subsidence phenomena from multi-temporal dinsar: a gis-based approach. GIScience & Remote Sensing. 59(1):1901–1917.

Hanssen RF. 2001. Radar Interferometry: Data Interpretation and Error Analysis. (Remote Sensing and Digital Image Processing; vol. 2). Springer Dordrecht.

Herring T, King R, Floyd M, McClusky S. 2018. GAMIT Reference Manual, GPS Analysis at MIT. Release. 10(7).

Hooper A, Segall P, Zebker H. 2007. Persistent scatterer InSAR for crustal deformation analysis, with application to Volcán Alcedo, Galápagos. J Geophys Res-Earth. 112(B07407):19.

Hooper A, Zebker H, Segall P, Kampes B. 2004. A new method for measuring deformation on volcanoes and other natural terrains using InSAR persistent scatterers. Geophys Res Lett. 31(23).

Hooper A, Zebker HA. 2007. Phase unwrapping in three dimensions with application to insar time series. JOSA A. 24(9):2737–2747.

Hooper AJ. 2006. Persistent scatter radar interferometry for crustal deformation studies and modeling of volcanic deformation. Stanford University.

Jung J, Kim Dj, Palanisamy Vadivel SK, Yun SH. 2019. Long-term deflection monitoring for bridges using x and c-band time-series sar interferometry. Remote Sensing. 11(11):1258.

Ketelaar G, Bähr H, Liu S, Piening H, Veen W, Hanssen R, Samiei-Esfahany S. 2020. Integrated monitoring of subsidence due to hydrocarbon production: Consolidating the foundation. In: Proceedings of the International Association of Hydrological Sciences; vol. 382. p. 117–123.

Khorrami M, Alizadeh B, Ghasemi Tousi E, Shakerian M, Maghsoudi Y, Rahgozar P. 2019. How groundwater level fluctuations and geotechnical properties lead to asymmetric subsidence: A PSInSAR analysis of land deformation over a transit corridor in the Los Angeles metropolitan area. Remote Sens-Basel. 11(4):377.

Lanari R, Berardino P, Borgström S, Del Gaudio C, De Martino P, Fornaro G, Guarino S, Ricciardi G, Sansosti E, Lundgren P. 2004a. The use of IFSAR and classical geodetic techniques for caldera unrest episodes: Application to the Campi Flegrei uplift event of 2000. Journal of Volcanology and Geothermal Research. 133(1-4):247–260.

Lanari R, Mora O, Manunta M, Mallorquí J, Berardino P, Sansosti E. 2004b. A small-baseline approach for investigating deformations on full-resolution differential SAR interferograms. IEEE T Geosci Remote. 42(7):1377–1386.

Li F, Liu G, Gong H, Chen B, Zhou C. 2022. Assessing land subsidence-inducing factors in the shandong province, china, by using ps-insar measurements. Remote Sensing. 14(12):2875.

Lomb N. 1976. Least-squares frequency analysis of unevenly spaced data. Astrophys Space Sci. 39:447–462.

Lyard F, Lefevre F, Letellier T, Francis O. 2006. Modelling the global ocean tides: Modern insights from FES2004. Ocean Dynam. 56(5):394–415.

Lyu M, Ke Y, Guo L, Li X, Zhu L, Gong H, Constantinos C. 2020. Change in regional land subsidence in beijing after south-to-north water diversion project observed using satellite radar interferometry. GIScience & Remote Sensing. 57(1):140–156.

Macchiarulo V, Milillo P, Blenkinsopp C, Giardina G. 2022. Monitoring deformations of infrastructure networks: A fully automated gis integration and analysis of insar time-series. Structural Health Monitoring. 21(4):1849–1878.

Mancini F, Grassi F, Cenni N. 2021. A Workflow Based on SNAP–StaMPS Open-Source Tools and GNSS Data for PSI-Based Ground Deformation Using Dual-Orbit Sentinel-1 Data: Accuracy Assessment with Error Propagation Analysis. Remote Sens. 13:753.

Mantovani E, Viti M, Babbucci D, Tamburelli C, Cenni N. 2020. Geodynamics of the central-western Mediterranean region: Plausible and non-plausible driving forces. Mar Petrol Geol:113.

Manunta M, De Luca C, Zinno I, Casu F, Manzo M, Bonano M, Fusco A, Pepe A, Onorato G, Berardino P, et al. 2019. The parallel SBAS approach for Sentinel-1 interferometric wide swath deformation time-series generation: Algorithm description and products quality assessment. IEEE T Geosci Remote. 57(9):6259–6281.

Martinelli G, Minissale A, Verrucchi C. 1998. Geochemistry of heavily exploited aquifers in the Emilia-Romagna region (po valley, northern Italy. Environ Geol. 36(3-4):195–206.

Massonnet D, Briole P, Arnaud A. 1995. Deflation of Mount Etna monitored by spaceborne radar interferometry. Nature. 375(6532):567–570.

Massonnet D, Feigl K. 1998. Radar interferometry and its application to changes in the Earth's surface. Rev Geophys. 36(4):441–500.

Massonnet D, Rossi M, Carmona C, Adragna F, Peltzer G, Feigl K, Rabaute T. 1993. The displacement field of the landers earthquake mapped by radar interferometry. Nature. 364:138–142.

Mazzanti P, Cipriani I. 2011. Terrestrial SAR interferometry monitoring of a civil building in the city of Rome. In: FRINGE 2011 Work. p. 19–23.

Milillo P, Giardina G, Perissin D, Milillo G, Coletta A, Terranova C. 2019. Pre-collapse space geodetic observations of critical infrastructure: The Morandi Bridge, Genoa, Italy. Remote Sensing. 11(12). Available from: https://www.mdpi.com/2072-4292/11/12/1403.

Milli S. 1997. Depositional setting and high-frequency sequence stratigraphy of the middle-upper pleistocene to holocene deposits of the roman basin. Geologica romana. 33(99):e136.

Modoni G, Darini G, Spacagna R, Saroli M, Russo G, Croce P. 2013. Spatial analysis of land subsidence induced by groundwater withdrawal. Eng Geol. 167:59–71.

Moreira A, Prats-Iraola P, Younis M, Krieger G, Hajnsek I, Papathanassiou K. 2013. A tutorial on synthetic aperture radar. IEEE Geosci Remote S Magazine. 1(1):6–43.

Noviello C, Verde S, Zamparelli V, Fornaro G, Pauciullo A, Reale D, Nicodemo G, Ferlisi S, Gulla G, Peduto D. 2020. Monitoring buildings at landslide risk with SAR: A methodology based on the use of multipass interferometric data. IEEE Geoscience and Remote Sensing Magazine. 8(1):91–119.

Ogundare JO. 2015. Precision surveying: the principles and geomatics practice. John Wiley & Sons.

Perissin D, Rocca F. 2006. High-accuracy urban dem using permanent scatterers. IEEE Transactions on geoscience and remote sensing. 44(11):3338–3347.

Perissin D, Wang T. 2011. Repeat-pass sar interferometry with partially coherent targets. IEEE Transactions on Geoscience and Remote Sensing. 50(1):271–280.

Polcari M, Secreti V, Anderlini L, Albano M, Palano M, Serpelloni E, Pezzo G. 2022. Multi-technique geodetic detection of onshore and offshore subsidence along the Upper Adriatic Sea coasts. International Journal of Applied Earth Observation and Geoinformation. 108:102756.

Qin Y, Perissin D. 2015. Monitoring ground subsidence in Hong Kong via Spaceborne Radar: Experiments and validation. Remote Sens. 7:10715–10736.

Qiu Z, Monserrat O, Crosetto M, Krishnakumar V, Zhou L. 2021. An innovative extraction methodology of active deformation areas based on sentinel-1 sar dataset: the catalonia case study. International Journal of Remote Sensing. 42(16):6228–6244.

Radman A, Akhoondzadeh M, Hosseiny B. 2021. Integrating insar and deep-learning for modeling and predicting subsidence over the adjacent area of lake urmia, iran. GIScience & Remote Sensing. 58(8):1413–1433.

Raspa G, Moscatelli M, Stigliano F, Patera A, Marconi F, Folle D, Vallone R, Mancini M, Cavinato GP, Milli S, et al. 2008. Geotechnical characterization of the upper pleistocene–holocene alluvial deposits of roma (italy) by means of multivariate geostatistics: Cross-validation results. Engineering Geology. 101(3-4):251–268.

Reale D, Fornaro G, Pauciullo A, Zhu X, Bamler R. 2011. Tomographic imaging and monitoring of buildings with very high resolution SAR data. IEEE Geoscience and Remote Sensing Letters. 8(4):661–665.

Rebmeister M, Schenk A, Bradley P, Dörr N, Hinz S. 2021. OCLeaS – A tomographic PSI algorithm using orthogonal matching pursuit and complex least squares. Procedia Computer Science. 181:220–230.

Roccheggiani M, Piacentini D, Tirincanti E, Perissin D, Menichetti M. 2019. Detection and monitoring of tunneling induced ground movements using Sentinel-1 SAR interferometry. vol. 11. Remote Sens-Basel.

Rosen PA, Hensley S, Joughin IR, Li FK, Madsen SN, Rodriguez E, Goldstein RM. 2000. Synthetic aperture radar interferometry. Proceedings of the IEEE. 88(3):333–382.

Rosen PA, Hensley S, Zebker HA, Webb FH, Fielding EJ. 1996. Surface deformation and coherence measurements of kilauea volcano, hawaii, from sir-c radar interferometry. Journal of Geophysical Research: Planets. 101(E10):23109–23125.

Rucci A, Ferretti A, Guarnieri AM, Rocca F. 2012. Sentinel 1 SAR interferometry applications: The outlook for sub millimeter measurements. Remote Sensing of Environment. 120:156–163.

Samieie-Esfahany S, Hanssen R, Thienen-Visser K, Muntendam-Bos A. 2009. On the effect of horizontal deformation on InSAR subsidence estimates. In: Proceedings of the Fringe 2009 Workshop; Nov; Frascati, Italy.

Samsonov S, d'Oreye N, Smets B. 2013. Ground deformation associated with post-mining activity at the french–german border revealed by novel insar time series method. International Journal of Applied Earth Observation and Geoinformation. 23:142–154.

Scargle J. 1982. Studies in astronomical time series analysis II. Statistical aspects of spectral analysis of unevenly sampled data. Astrophys J. 263:835–853.

Scheiber R, Moreira A. 2000. Coregistration of interferometric SAR images using spectral diversity. IEEE Transactions on Geoscience and Remote Sensing. 38(5):2179–2191.

Schmidt DA, Bürgmann R. 2003. Time-dependent land uplift and subsidence in the santa clara valley, california, from a large interferometric synthetic aperture radar data set. Journal of Geophysical Research: Solid Earth. 108(B9).

Scifoni S, Bonano M, Marsella M, Sonnessa A, Tagliafierro V, Manunta M, Lanari R, Ojha C, Sciotti M. 2016. On the joint exploitation of long-term dinsar time series and geological information for the investigation of ground settlements in the town of roma (italy). Remote Sensing of Environment. 182:113–127.

Scivetti N, Marcos P, Prieto ME, Pavón Pivetta C, Benedini L, Stremel AJ, Bahía ME, Bilmes A, Richiano S. 2021. Geomorphological and anthropic impacts over land surface displacements: application of dinsar technique to the case of bahía blanca city, argentina. Geocarto International:1–20.

Simeoni U, Tessari U, Corbau C, Tosatto O, Polo P, Teatini P. 2017. Impact of land subsidence due to residual gas production on surficial infrastructures: The Dosso degli Angeli field study (Ravenna, Northern Italy. Engineering Geology. 229:1–12.

Solari L, Ciampalini A, Raspini F, Bianchini S, Moretti S. 2016. PSInSAR analysis in the Pisa urban area (Italy): A case study of subsidence related to stratigraphical factors and urbanization. Remote Sensing. 8(2):120.

Stramondo S, Bozzano F, Marra F, Wegmuller U, Cinti F, Moro M, Saroli M. 2008. Subsidence induced by urbanisation in the city of Rome detected by advanced InSAR technique and geotechnical investigations. Remote Sens Environ. 112:3160–3172.

Stramondo S, Saroli M, Tolomei C, Moro M, Doumaz F, Pesci A, Loddo F, P B, Boschi E. 2007. Surface movements in Bologna (Po Plain - Italy) detected by multitemporal DInSAR. Remote Sens Environ. 110(3):304–316.

Sytnik O, Stecchi F. 2014. Disappearing coastal dunes: Tourism development and future challenges, a case study from Ravenna, Italy. J Coast Conserv. 19(5):715–727.

Talledo DA, Miano A, Bonano M, Di Carlo F, Lanari R, Manunta M, Meda A, Mele A, Prota A, Saetta A, et al. 2022. Satellite radar interferometry: Potential and limitations for structural assessment and monitoring. Journal of Building Engineering. 46:103756. Available from: https://www.sciencedirect.com/science/article/pii/S2352710221016144.

Tang Y, Cui Z, Wang J, Lu C, Yan X. 2008. Model test study of land subsidence caused by high-rise building group in Shanghai. Bull Eng Geol Environ. 67:173–179.

Teatini P, Ferronato M, Gambolati G, Bertoni W, Gonella M. 2005. A century of land subsidence in Ravenna, Italy. Environmental Geology. 47(6):831–846.

Teatini P, Ferronato M, Gambolati G, Gonella M. 2006. Groundwater pumping and land subsidence in the Emilia-Romagna coastland, Italy: Modeling the past occurrence and the future trend. Water Resources Research. 42(1).

Teatini P, Tosi L, Strozzi T. 2011. Quantitative evidence that compaction of Holocene sediments drives the present land subsidence of the Po Delta, Italy. J Geophys Res Solid Earth. 116.

Tomás, Pagán, Navarro, Cano, Pastor, Riquelme, Cuevas-González, Crosetto, Barra, Monserrat, et al. 2019. Semi-Automatic Identification and Pre-Screening of Geological–Geotechnical Deformational Processes Using Persistent Scatterer Interferometry Datasets. Remote Sensing. 11(14):1675.

Torres R, Snoeij P, Geudtner D, Bibby D, Davidson M, Attema E, Potin P, Rommen B, Floury N, Brown M, et al. 2012. GMES Sentinel-1 mission. Remote Sensing of Environment. 120:9–24.

Tosi L, Teatini P, Strozzi T. 2013. Natural versus anthropogenic subsidence of Venice. Sci Rep. 3:2710.

Van Leijen FJ, Van der Marel H, Hanssen RF. 2021. Towards the integrated processing of geodetic data. In: 2021 IEEE International Geoscience and Remote Sensing Symposium IGARSS. IEEE. p. 3995–3998.

Wang S, Zhang G, Chen Z, Cui H, Zheng Y, Xu Z, Li Q. 2022. Surface deformation extraction from small baseline subset synthetic aperture radar interferometry (sbas-insar) using coherence-optimized baseline combinations. GIScience & Remote Sensing. 59(1):295–309.

Werner C, Wegmuller U, Strozzi T, Wiesmann A. 2003. Interferometric point target analysis for deformation mapping. In: IGARSS 2003. 2003 IEEE International Geoscience and Remote Sensing Symposium. Proceedings (IEEE Cat. No. 03CH37477); vol. 7. IEEE. p. 4362–4364.

Xu Y, Ma L, Du Y, Shen S. 2012. Analysis of urbanisation-induced land subsidence in Shanghai. Nat Hazards. 63:1255–1267.

Yagüe-Martínez N, Prats-Iraola P, Rodríguez González F, Brcic R, Shau R, Geudtner D, Eineder M, Bamler R. 2016. Interferometric Processing of Sentinel-1 TOPS Data. IEEE Transactions on Geoscience and Remote Sensing. 54(4):2220–2234.

Zebker H, Villasenor J. 1992. Decorrelation in interferometric radar echoes. IEEE T Geosci Remote. 30(5):950–959.

Zhu M, Wan X, Fei B, Qiao Z, Ge C, Minati F, Vecchioli F, Li J, Costantini M. 2018. Detection of building and infrastructure instabilities by automatic spatiotemporal analysis of satellite SAR interferometry measurements. Remote Sensing. 10(11). Available from: https://www.mdpi.com/2072-4292/10/11/1816.